PHOTOMETRIC CALIBRATIONS OF METALLICITY AND TEMPERATURE FOR M DWARFS

NEDA HEJAZI

A THESIS SUBMITTED TO THE FACULTY OF GRADUATE STUDIES IN PARTIAL FULFILMENT OF THE REQUIREMENTS FOR THE DEGREE OF MASTER OF SCIENCE

GRADUATE PROGRAM IN ASTRONOMY,

YORK UNIVERSITY,

TORONTO, ONTARIO

OCTOBER 2014

Abstract

Based on a carefully collected sample of dwarf stars, a new empirical photometric calibration to estimate the metallicity of late-type K and early-to-mid-type M dwarfs is presented. The calibration sample has two parts; the first part includes 21 M dwarfs in common proper motion pairs with an FGK star or early-type M dwarf of known metallicity and the second part contains 50 dwarfs with metallicities obtained through moderate-resolution spectra. Using the most recent BT-Settl model atmospheres and the estimated effective temperatures of stars in the calibration sample, the synthetic colour-colour diagram most sensitive to M-dwarf temperatures is identified.

By applying these methods to a large sample of around 1,300,000 M dwarfs from the Sloan Digital Sky Survey (SDSS) and the Two-Micron All Sky Survey (2MASS), the metallicity and temperature distributions of these small stars are determined. Using a photometric parallax, the Galactic heights of stars in the large sample are calculated. Our results show a shift in metallicity distribution toward lower metallicities as a function of Galactic height. The relation between metallicity and absolute magnitude is also investigated.

A scarcity of metal-poor dwarf stars in the metallicity distribution relative to the Simple Closed Box Model indicates the existence of the "M dwarf problem," similar to the previously known G and K dwarf problems. It is shown that the Galactic chemical evolution models proposed to solve the G and K dwarf problems could also be a solution of the M dwarf problem as well.

Acknowledgments

I would like to express the deepest appreciation to my supervisor, Professor Michael De Robertis, whose timely guidance, constructive comments and full support helped me shape the thesis into its final form. His dedication and encouragement were invaluable and enabled me to accomplish the research. Without his assistance, suggestions and prompt inspirations this work would never have been completed.

I would also to extend my sincere gratitude to Professor Peter Dawson from Trent University for his thoughtful advice and worthy contribution to all stages of this study. I really thank him for all valuable points he taught me graciously. In addition, I am very indebted to my mentor and the committee chair, Professor Patrick Hall, for his careful reading and helpful suggestions which improved my thesis. I would especially like to acknowledge him for helping me with my coursework and teaching assistance during the graduate years as well. I am also grateful for assistance provided by the former graduate student, Dr. Xiaoyi Dong, while the work was being undertaken.

Last, but not least, I wish to thank my beloved husband for the kindness, encouragement and support he has shown while I was carrying out this research.

Table of Contents

List of Tables

List of Figures

Chapter 1

Properties and Significances of M dwarfs

1.1 *Introduction*

M stars (M dwarfs or red dwarfs) are among the smallest (with masses $0.075 < M < 0.6\ M_{\odot}$ and radii $0.08 < R < 0.62\ R_{\odot}$), coolest (with temperatures $2300 < T_{eff} < 3800$ K) and faintest (with luminosities $0.00015 < L < 0.072\ L_{\odot}$) stars in our Galaxy which fall on the lower right of the main sequence in the HR diagram[1], Figure 1.1. These small stars are the dominant stellar component of the Milky Way, making up ~70% of all stars by number and nearly half the stellar mass of the Galaxy (Reid & Gizis 1997). Their main-sequence lifetimes are much longer than the current age of the Universe (Laughlin et al. 1997) and many of them have completed many Galactic orbits (Reid & Hawley 2000). They can, therefore, be used as excellent tracers of

[1]The HR diagram, named after Ejnar Hertzsprung and Henry Norris Russell, is a scatter graph, presenting the correlation between the absolute magnitude (luminosity) and temperature (spectral type or colour) of stars. Most of stars are found in a curve, extending from the upper left to the lower right of the graph which is called the main sequence. Stars on this curve are burning hydrogen in their cores, with masses ranging from around a tenth of the solar mass up to 200 times as massive (taken from:
http://en.wikipedia.org/wiki/Hertzsprung%E2%80%93Russell_diagram (unless otherwise noted, all URLs quoted throughout refer to 5 October 2014)
http://www.space.com/22437-main-sequence-stars.html).

Galactic structure and population as well as Galactic chemical, kinematical and dynamical evolution. Although M dwarfs are the most ubiquitous stars in the Galaxy, due to their intrinsic faintness, only very small samples were available for study. Prior to using CCDs[2] with telescopes in the early 1980's, photometric measurements were made only by photographic plates whose quantum efficiency[3] (QE) is ~ 1% and their typical photometric accuracy is 0.1-0.2 mags (Karttunen et al. 2007). Thus their limited photometric accuracy made it difficult to compare observations with models, especially for faint objects such as M dwarfs. As photographic plates were replaced by more efficient CCDs, highly accurate observations even for very faint stars became possible. Nowadays, photometry as accurate as ~ 0.01 mags[4] for objects as faint as m ~ 27 mags[5] can be made by advanced telescopes over most parts of the sky. Since the advent of deep surveys such as the Sloan Digital Sky Survey (SDSS, York et al. 2000) and the Two-Micron All Sky Survey (2MASS, Skrutskie et al. 2006) M dwarfs have been investigated in photometric samples of unprecedented sizes (tens of millions of M dwarfs) which has revolutionized this area of astronomy. In addition to photometry, spectra of M dwarfs have also been acquired in large numbers. In particular, SDSS has provided the largest spectroscopic database to date, which has resulted in a catalog which includes important information about spectral types, radial velocity, and chromospheric activity estimates (as traced by Hα emission in Balmer series) or more than 70,000 M stars.

M dwarfs have been employed for different stellar and Galactic studies using SDSS databases. Some efforts have been made to determine the mean and standard deviation of several colours[6] at each spectral type between M0 and M9[7] (Hawley et al. 2002, West et al. 2005, Bochanski et al.

[2]Charge-coupled devices, is a device for transferring electrical charges, from the device to a place where the charges can be converted into a digital value. For more details see:
http://en.wikipedia.org/wiki/Charge-coupled_device

[3]The number of electrons released by a photocell per photon of incident radiation of a given energy; for more details see: http://en.wikipedia.org/wiki/Quantum_efficiency

[4] For example, this is the typical photometric accuracy via the MegaPrime/MegaCam imager at Canada-France-Hawaii Telescope (CFHT).

[5] Faintest objects observable in visible light with 8m ground-based telescopes.; for more details see:
http://en.wikipedia.org/wiki/Apparent_magnitude

[6] The colour index, or briefly colour is the difference between the magnitudes in two different filters, such as U and B, where U is sensitive to ultraviolet rays and B is sensitive to blue light. The difference between U and B is called the U-B colour index. The smaller the colour index, the bluer (or hotter) the object is. For more details see:
(http://en.wikipedia.org/wiki/Color_index).

[7] Each spectral type such as M type is divided to 10 sub-spectral types from 0 to 9; M0, M1,…, M9.

2007a, and West et al. 2011). Useful colour-absolute magnitude[8] relations (CMRs) have been obtained (Hawley et al. 2002, Bochanski 2008, Bochanski et al. 2010, Bochanski et al. 2011) which can be applied to estimate the distance of a star (photometric parallax[9]) when its astrometric parallax[10] is not available. Magnetic activity of M dwarfs has been traced by Hα emission through the SDSS spectra (West et al. 2004, West et al. 2008) and some constraints have been made on the age-activity relation[11] (West et al. 2008).

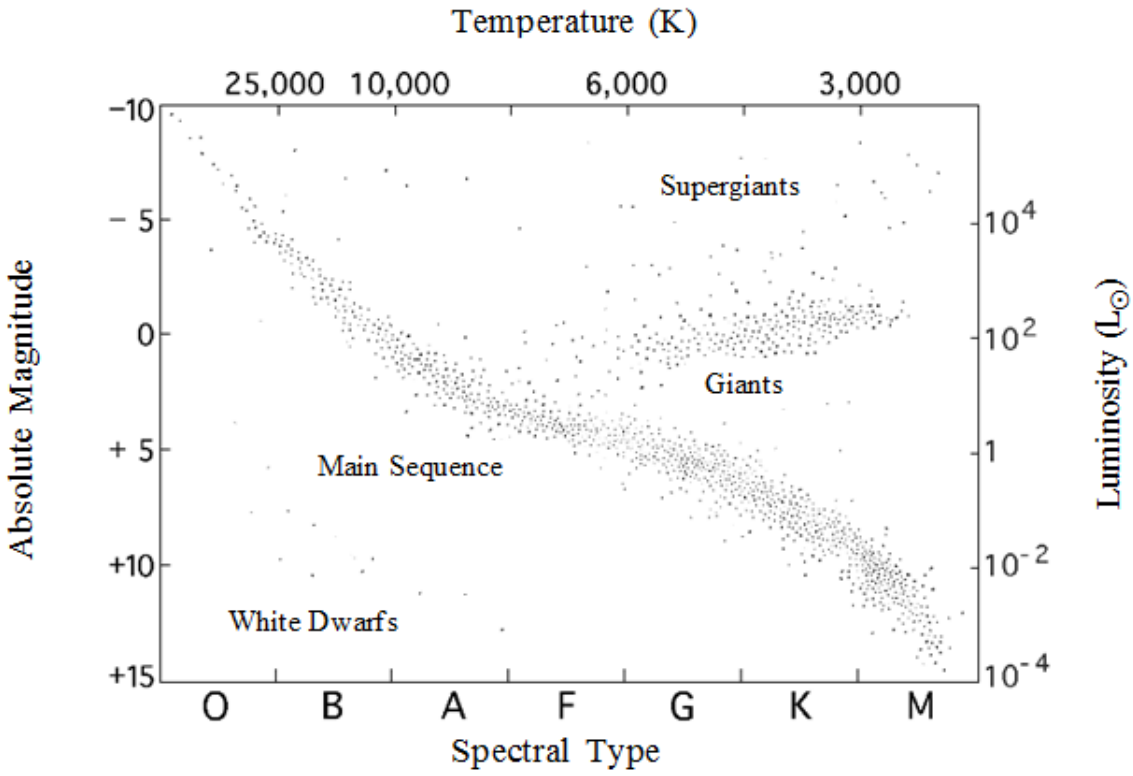

Figure 1.1 A version of the HR diagram, in form of absolute magnitude and luminosity versus spectral type and temperature. M dwarfs are located in the lower right of the diagram. (Taken from "Live from RXTE!Team".)

The fundamental parameters such as mass, radius and temperature of two M dwarfs in a double-lined eclipsing binary system has carefully been determined (Blake et al. 2008). This can allow

[8] This is the measure of intrinsic brightness of an astronomical object.
[9] This is a method that uses the known colours and absolute magnitudes of stars to infer their distances.
[10] It is the displacement of the apparent position of a star viewed along two different lines of sights and measured by the inclination angle between the two lines.
[11] It has been found that there is a relation between magnetic activity (as traced by Hα emission) and age of low-mass stars in such that younger stars show more activity than older ones.

identifying such double systems in future surveys (e.g., Pan-STARRS[12]) which will produce valuable information about low-mass eclipsing binaries. The fundamental properties of stellar systems such as the luminosity and mass functions of low-mass stars have been measured in large samples (Covey et al. 2008 and Bochanski et al. 2010, with samples of more than 25,000 and 15 million M dwarfs respectively).

Galactic structure has also been studied using M stars; for instance Bochanski et al. 2010 used SDSS photometry of more than 15 million stars to measure the scale heights and scale lengths of two Galactic structural components, i.e., the thin and thick disks[13]. Moreover, careful studies have attempted to characterise the kinematic distributions of the two disks (Bochanski et al. 2007b). More interestingly, proper comparisons have been made between the kinematics of different M dwarf populations (e.g., early-type and late-type populations, active and inactive stars, or a combination of these) (Bochanski et al. 2011). In addition to Galactic structure and kinematics, Galactic chemical evolution has recently been investigated by determining the metallicity[14] of more than 4000 M dwarfs through their SDSS spectra (Woolf & West 2012).

In addition to stellar and Galactic studies, M dwarfs have been under scrutiny as planet host candidates. Widely used methods in detecting exoplanets such as the radial velocity (Doppler) and transit techniques are more sensitive to those orbiting stars of lower mass. At a given orbital period, the reflex radial velocity[15] amplitude scales with the stellar mass $M^{-2/3}$ and transit depth scales as $M^{-2.1}$ (Seager & Mallén-Ornelas 2003, Moorhead 2008). It is therefore easiest to detect planets around M dwarfs, all other factors being equal. Moreover, measurements of both radius (by the transit technique) and mass (by the Doppler technique) of Earth-size planets can be made most efficiently if they orbit M dwarfs (Rojas-Ayala et al. 2013).

Since M dwarfs are much less luminous than FGK stars, the circumstellar habitable zone, the volume in which the surface temperature of a planet permits liquid water to exist, is closer to an M dwarf. Planets in smaller orbits are more easily detectable, because these planets induce larger

[12]The Panoramic Survey Telescope and Rapid Response System

[13] Many spiral galaxies have been shown to have two different disks that are composed of two kinematically and chemically distinct populations, the thin disk (the narrower one) and the thick disk (the broader one).

[14] Metallicity of a star is commonly defined as: $[\frac{Fe}{H}] = \log_{10}(\frac{N_{Fe}}{N_H})_{Star} - \log_{10}(\frac{N_{Fe}}{N_H})_{Sun}$ where N_{Fe} and N_H are the number of iron and hydrogen atoms per unit of volume, respectively.

[15] The radial velocity of star due to the planet's gravity

reflex motions on the host stars. Besides, the orbital periods of planets in smaller orbits are shorter, so that observations of a few weeks or months are usually enough to detect the periodic variations. As a result, planets within the habitable zone are more likely to be detected around small stars. Nevertheless, the habitability of M dwarfs has been debated; some studies have shown that small habitable zones, the probability of tidally locked planets, magnetic activity and high stellar variations can impede the survival of life on such planets. However, a recent study (Grenfell et al. 2013) has demonstrated that uncertainties in the UV emissions of cool M dwarfs may have a potentially large impact upon atmospheric biosignatures in simulations of Earth-like exoplanets. This emphasizes the need for future missions to better characterize the UV emission of M dwarfs in order to understand potential biosignature signals.

Considering the widespread significance of M dwarfs mentioned above, the determination of fundamental parameters, such as temperature and metallicity, of these dwarfs has relevant implications for stellar, Galactic and planetary astronomy. For example, under the general assumption that the photospheric chemical composition of stars represents the local Galactic chemical composition, and since M dwarfs are the dominant stellar component of the Galaxy, the metallicity of these small stars can be employed to test the current models of Galactic chemical evolution[16] (for example, Woolf & West 2012). Metallicity is also of great importance in modern theories of planet formation. To first approximation, the metallicity of a star is equal to its protoplanetary disk's initial metallicity (Rojas-Ayala et al. 2013). It is well established that the presence and number of gas giants ($M > M_{\mathrm{Jupiter}}$) around FGK stars is strongly correlated with stellar metallicity and mass. It has been demonstrated that more metal rich and/or more massive FGK stars are more likely to host giant planets than their metal poorer and/or less massive counterparts (Gonzalez 1997). This relationship is referred to as the planet-metallicity correlation (PMC). The validity of the PMC for M dwarfs has been under some investigation (for example; Mann et al. 2013b, Neves et al. 2013) which indicates the correlation between the presence of giant planets and metallicity does hold for M dwarfs as well. Nonetheless, these studies are controversial, mainly due to complications in the current metallicity calibrations of low-mass stars (see Chapter 2).

[16]More precisely, M dwarfs are largely convective, meaning their true abundances are reflected by the metallicity measured through their spectra or photometry.

In section 1.2, the historical trend through which stars of spectral type M were recognized and classified is reviewed. In section 1.3, some important physical properties of M dwarfs which make them distinctive among other main sequence stars are addressed.

1.2 *Spectral Type : Historical Notes*

Spectral type is a fundamental property of a star, which relates to its surface temperature. The type 'M 'was designated for the first time at Harvard by Mrs. W.P. Fleming for spectral classification outlined in the *Draper Memorial Catalogue* in 1890. Early spectral type classifications were based on visual or photographic data, and then limited only to bright stars. Almost all stars assigned to M type in the early catalogs were giants rather than dwarfs[17]. Although the Harvard system provided a ready means to compare general properties of many stars (approximately), it suffered from its dependence on internal classification criteria, which limited its applicability. In order to assign a spectral type to a star, the relative strengths of lines and bands in the spectrum of the star were compared to a reference list of line ratios, rather than by matching against a set of standard stars. Moreover, it had practical problems in the designation of a spectral type to stars with specific physical properties. In other words, each spectral type spanned a wide range of properties. A well-designed system of spectral-type ranking is expected to classify corresponding physical properties as well.

Those problems were resolved in the MK spectral classification system[18] in 1943. The success of this system was mainly due to its empirical definition of spectral type with respect to a set of particular standard stars. In the MK system, the spectral type M was characterised by the presence of strong absorption bands largely due to the diatomic molecule titanium oxide, TiO. The TiO bands dominate the optical spectra of M dwarfs and are the primary indicators for this spectral type. At that time, only a few M dwarfs were sufficiently bright for spectroscopic studies. Furthermore, most photographic observations were restricted to the blue-green region (≈ 4400-5400 Å) of the spectrum which is far from the peak of the spectral energy distribution, making it difficult to obtain high signal-to-noise ratio spectra for these cool stars (Reid & Hawley, 2000). As a result, while M giants were classified to the spectral type M6, in the

[17]As shown in the Figure 1.1, the white dwarfs (see footnote 29), giants and supergiants are different classes of stars which can be distinguished from main sequence stars.
[18]Those problems were resolved in the MK spectral classification system (Morgan & Keenan 1943).

original MK system the classification of the main sequence M stars extended only to the M2 type.

With the improvement of larger, better equipped telescopes with more efficient spectrographs, later type M dwarfs were detected and the need for extending the spectral classification to stars with types later than M2 was felt. Without any accepted rules, several incompatible systems for classifying M dwarfs came into general use. The two most widely used systems were the Yerkes system (Morgan 1938, Kuiper 1942) and Joy's Mount Wilson system (Joy, 1947). The spectral-type tracer in the former was based on the strength of TiO bands between 5800 and 6500 Å, while the latter took the strength of TiO bands around 4400 Å as the main indicator for spectral classification. Since these two systems operated according to different criteria in different wavelength regions, the net result was different spectral types for the same star. Therefore, devising a unified system was clearly necessary.

M dwarfs are low-luminosity, cool stars and the best way to classify these stars is to use redder wavelengths, maximizing the signal-to-noise ratio in spectroscopic observations. It should be noted the spectral regions used in a classification system have to contain suitable atomic and molecular features as well. The first attempts for such an extension were made by Keenan & MacNeil (1976) and Boeshaar (1976), but both studies were limited to wavelengths shortward of 6800 Å, reflecting the detector technology at that time, and neither provided classification of stars later than M6. The solidification of the M dwarf classification system came with the availability of detectors with wider sensitivity toward red wavelengths. One system, defined by Bessell (1991) was related to Wing's giant-star system (Wing 1973), based on TiO bands for earlier-type M dwarfs and VO bands for later types where the TiO bands saturate.

At the same time, Kirkpatrick, Henry & McCarthy (1991) devised a system (KHM system) based on a least-squares comparison of low-resolution (18Å) spectra against a grid of standards (i.e., spectra of some actual stars) made at the same resolution. In their original paper, they showed the spectra of 39 K and M dwarf spectroscopic standards (primary standards), as well as 38 secondary standards from 6300 to 9000 Å. In addition to those dwarfs, the spectra of 14 giants were presented from 6300 to 9000 Å along with two miscellaneous spectra. They also provided an extensive list of atomic and molecular features (which are dominated by TiO, VO and CaH

bands) in the spectra of late K and M stars of all luminosity classes. In this system, spectral classification is accomplished by using a spectrophotometric least-squares technique in which both the features and the slope of the spectrum are used. Moreover, from the spectral slopes and the strengths of the red and near-infrared (NIR) spectral features, it is possible to distinguish dwarfs from giants and a luminosity classification can also be carried out. This spectroscopic method (based on both spectral features and spectral slopes) can be compared with the method based only on spectral features. The former requires the flux calibrations for the data to be relatively accurate so that any errors in the slope of the spectra remain small, while the latter can be done without flux calibration but a fit to the continuum of the spectrum is needed. Because "true" continuum points are more difficult to identify, rather than opacity minima between certain bandheads of TiO[19], this second method is more likely prone to error than the first one.

Reid et al. (1995) developed a spectral classification system which mimicked the Kirkpatrick et al. (1991) sequence. They applied "The Third Catalogue of Nearby Stars" including over 1850 stars which covered less than one-third of the spectral range used by Kirkpatrick et al. (1991) and hence the feature-by-feature minimization approach was not useful anymore. They therefore chose a specific feature (TiO bandstrength) as a spectral type indicator, connecting their observations to the KHM system by employing its spectral-type standard stars and defined a new system. By using this system, the spectral types of 1685 stars, as late as K or M type, were obtained which was one of the largest spectroscopic studies of low-mass dwarfs at that time.

With the advent of 2MASS and SDSS, large spectroscopic catalogs of low–mass stars became available. Covey et al. (2007) provided an IDL-based code package, dubbed "the Hammer[20]", which automatically assigns spectral types to input spectra by measuring a suite of spectral indices and performing a least squares minimization of the residuals between the indices of the target and those measured from spectral type standards. This is based only on the relative strength of spectral features (not the spectral slopes), which computes 26 atomic (H, CaI, CaII, NaI, MgI, FeI, Rb and Cs) and molecular (G band, CaH. TiO, VO, and CrH) features which are prominent in late-type stars, as well as two colours, named BlueColour and Colour-1 (Table 6 in

[19]Even in high resolution spectra, the TiO lines blend with all other lines and create a pseudo continuum, which makes the estimation of the true continuum level very difficult.
[20]http://www.astro.washington.edu/users/slh/hammer/

Covey et al. 2007), which sample the broadband shape of the spectral energy distribution (SED). These indices sample spectral features which are strong enough to be visible in moderate-resolution spectra and that have previously been shown to be sensitive to surface temperature (for example Gizis & Reid 1999, Kirkpatrick et al. 1999). Each index, however, is most useful within a given spectral type range, and can decrease the accuracy of the spectral typing process outside that range if it contributes an excessive amount of weight to the goodness of fit parameter. For this reason, the Hammer excludes indices which are unlikely to be useful in constraining the spectral type of a given star. The values of the remaining indices are then compared to those of the template grid of known standards to obtain the best-fit spectral type and in in this way a spectral type is assigned to the star. Covey et al. (2007) tested the accuracy of the Hammer by measuring the spectral type of dwarf templates whose spectral types were already determined by other means. These tests indicated that the Hammer's automated spectral types are accurate to within ± 2 subclasses for K and M type stars.

The Hammer spectral typing algorithm was originally developed for late-type SDSS spectra, but has subsequently been modified for spectral classification of stars observed in different surveys, spanning the MK spectral sequence. It has been widely used to classify stellar spectra. West et al. (2008) determined the spectral types of 44,084 dwarfs (M0-L0) drawn from SDSS Data Release 5 (DR5, Adelman-McCarthy 2007) by the Hammer. They examined a subset of the spectra by eye and confirmed that the spectral types assigned by Hammer were accurate to within ± 1 subtype. Lee et al. (2008) developed the SEGUE (Sloan Extension for Galactic Exploration and Understanding) Stellar Parameter Pipeline(SSPP) which derives, using multiple techniques, the radial velocities and fundamental stellar atmospheric parameters of stars in a large sample (140,000 stars). For the coolest stars (T_{eff}< 4500 K), they employed the Hammer spectral typing software to estimate the MK spectral type of each star. It was also discussed that the Hammer code assigns spectral types accurate to within ± 2 subtypes for K and M dwarfs.

Great effort has been made by West et al. (2011) to reduce systematic discrepancies in the spectral types from West et al. (2008) sample that were determined automatically by the Hammer algorithm. A bias was detected as a systematic offset for late-type stars whose classification was often one subtype earlier than determined through visual inspection. For this reason, they visually inspected 116,161 M dwarf candidates and manually assigned spectral

types and removed non-M dwarf interlopers[21].It was found out that for early-type M dwarfs the Hammer and the spectral typers agree most of the time. However, for about 38% of the late-type M dwarfs the Hammer assign spectral types one subtype earlier than the average human spectral typer. This showed that while the Hammer produces automatic spectral types within ± 1 subtype accuracy, there is a systematic offset of subtype for the late-type stars. At last, this work led to the assembling of the largest spectroscopic catalog of M dwarfs to date, including 70,841 visually inspected stars. Finally, the recent study of Yi et al. (2014) presented a spectroscopic catalog of 67,082 M dwarfs from "The Large Sky Area Multi-Object Fiber Spectroscopic Telescope (LAMOST)" Pilot Survey. Each spectrum was processed using the Hammer spectral typing software to determine the star's spectral type. They adopted the low-mass (M0-L0) template spectra derived by Bochanski et al. 2007 (from over 4000 SDSS spectra) and tested the Hammer code with M dwarfs of known spectral type. They investigated each mismatched case and realized that the original Hammer indices are not adequate to discriminate all of the subtypes. By running an ensemble learning method, Random Forest (Breiman, 2001), they were able to modify the Hammer indices through adding some new indices. The amended Hammer results in an average offset of 0.6 subtype as compared to the visually inspected ones.

1.3 *Physical Properties*

1.3.1 *Interior*

The central physical conditions for low mass stars are among the most distinctive ones that main sequence stars can experience during their lives. For comparison, the central temperature of solar type stars is $T_c \sim 10^7$ K while for an M dwarf with mass $\sim 0.1\ M_\odot$ this temperature is of order of 4×10^6 K. The central density increases with decreasing mass, from $\rho_c \sim 100$ g cm^{-3} for the Sun to ~ 500 g cm^{-3} for a star with M $\sim 0.1\ M_\odot$. Under these conditions, the average ion electrostatic energy is several times the average kinetic energy, characterizing a strongly coupled ion plasma (Chabrier et al. 2005). Furthermore, the circumstances in low mass stars are appropriate for an electron gas to be in a partially degenerate state[22].When the density is quite

[21] The sample was divided among 17 individuals who used the manual "eyecheck" mode of the hammer to investigate the spectra. The order of the co-authors was based on the number of spectra examined.

[22]The Pauli Exclusion Principle does not allow two half-integer spin particles (fermions) to simultaneously occupy the same quantum state (http://en.wikipedia.org/wiki/Pauli_exclusion_principle). This restricts the number of

large, pressure dissociation[23] and ionization[24] become important; a situation which is well achieved in M dwarfs. All these processes have to be taken into account in evaluating the "Equation of State"[25] (EOS) for the interiors of M stars (Chabrier et al. 2005, Cassisi 2011).

In the interior of solar-like stars, heat is basically transferred by radiative processes, except for a rather small region in the outermost envelope where convective processes dominate. As mass decreases, the inner radiative region shrinks and below a specific mass it ultimately disappears and star becomes fully convective. In particular, for an M0-type dwarf ($M \sim 0.55M_{\odot}$), around 90% of the total mass is located in the inner radiative region, but this fraction declines to 70% for an M2/M3-type star ($M \sim 0.4M_{\odot}$). At spectral type M3.5-M4 ($M \sim 0.35M_{\odot}$) stars become entirely convective (Chabrier & Baraffe 1997, Reid and Hawley 2000).

Studies have demonstrated that M dwarfs are relatively magnetically active. Despite observations of stellar activity for decades, its exact mechanism is not well understood. In the Sun and (solar type stars), the generation of magnetic fields is related to the Sun's rotation. It has been found that there is a rotational boundary between the inner rotating radiative zone and the outer rotating convective zone. This boundary, called the tachocline, generates rotational sheer permitting magnetic fields to be produced and to reach the surface of the Sun, where they appear as observable magnetic loops (Parker 1993, Thompson & Christensen-Dalsgaard 2003, West et al. 2008). These loops heat the upper tenuous atmosphere layers emerging as the solar chromosphere, transition region and corona. These cause measurable emission lines in the

---

electrons that can have low energy. When electrons are packed together the number of available low energy states is not enough and many electrons are forced to occupy high energy states. When this happens the electrons are said to be degenerate. This results in an emergent pressure against compression of matter into smaller volumes.

[23]Vardya (1960) proposed the idea of pressure dissociation, in analogy with the effect of pressure ionization (see below). For a given temperature, as the pressure is increased, the molecules and atoms are brought closer, so that H_2 - H_2 and H_2 – H interactions become increasingly important. The effect of this is to obliterate the higher energy levels, implying a decrease in the effective dissociation potential. This affects the abundances of molecular hydrogen and could be important in models of late-type main sequence stars and white dwarfs (Chabrier et al. 2005, Cassisi 2011).

[24]A condition found in degenerate matter such as the internal conditions in white dwarfs and low mass stars, in which the atoms are packed so tightly that the electron orbits overlap to the point where an electron can no longer be regarded as belonging to any particular nucleus and must be considered free(Chabrier et al. 2005, Cassisi 2011).

[25] An equation of state is a thermodynamic equation describing the state of matter under a given set of physical conditions (http://en.wikipedia.org/wiki/Equation_of_state).

optical, UV and X-ray spectral regions. The faster a star rotates, the stronger the magnetic fields that are created and the stronger the magnetic heating that takes place.

It has been shown that coronal and chromospheric emissions, which trace magnetic heating of the atmosphere, can also be linked to the rotation of M dwarfs (e.g., Noyes et al. 1984, Delfosse et al. 1998, Pizzolato et al. 2003). Browning et al. (2010) analyzed the rotation and chromospheric activity of 121 nearby M dwarfs using their high resolution spectra. They found out that rotation correlates with magnetic activity; all rotating stars were active but not all active stars are detectably rotating. Browning et al. pointed out it is possible that all the active, non-rotating stars occur at low inclination angles[26] with respect to our line of sight. It should be noted that at a spectral type of M3.5-M4, stars become fully convective and the tachocline probably vanishes. However, in spite of this change, magnetic activity persists in late-type M dwarfs. West et al. (2008) investigated the variation of activity in M dwarfs (traced by Hα emission) as a function of spectral type. They found that the fraction of active stars for early-type M dwarfs is very small ($\lesssim 0.05$), peaks at the spectral type M7-M8 ($\cong 0.75$) and drops into the L dwarf regime.

1.3.2 *Atmosphere*

Due to the cool surface temperatures of M dwarfs ($T_{eff} \lesssim 4000$ K), numerous molecules form in their atmospheres. M-dwarf spectra are mainly characterized by the presence of strong molecular absorption lines such as metal oxides (e.g., TiO and VO) and metal hydrides (e.g., CaH, FeH and MgH) which are the main opacity sources at optical wavelengths, and also CO and H_2O which are the most efficient absorbers in the infrared (IR) part of the spectra. The situation for stars with $T_{eff} \lesssim 2500$ K is even more complex where the condensation of grains becomes increasingly relevant. At these low temperatures, there is evidence for the condensation of metals and silicates into grains, e.g. TiO into $CaTiO_3$, or Mg and Si into $MgSiO_3$, and Ca into $CaSiO_3$ and Ca_2SiO_4 (Chabrier et al. 2005).

There are clear correlations between the strength of individual lines and spectral type. In Figures, 1.2 and 1.3 several M-dwarf spectra are represented. As can be seen, TiO is very weak at spectral

[26] The angle between the rotation axis and the line of sight

type K7 but becomes stronger until type M6 where it saturates. At approximately the same temperature as the redder TiO bands saturate, VO becomes noticeable at 7330-7530 Å. FeH bandheads also emerge in the latest spectral types. The strongest atomic lines at the optical range are CaI at 4227 Å, the Na I doublets at 5890/5896 Å and 8183/8195 Å, and K I doublets at 7665/7699 Å. The most prominent features in the IR are the broad absorption bands at 1.4, 1.8 and 2.6 μm due to water. Other weaker molecular bands, especially CO at 2.15 μm and FeH in the 1.1-1.2 μm region, are also present (Reid and Hawley 2000).

It is important to note that in low mass dwarfs, due to high surface gravity[27] (log (g) ≅ 5) and surface pressure, the photosphere is thin, extending only 100-200 km into the star. This thin layer is able to transfer the energy from the core, generated by nuclear reactions, to space and adjust the surface temperature and luminosity effectively (Reid and Hawley 2002).

[27] The surface gravity of a star is defined by $g=\frac{GM}{R^2}$ (usually expressed in cgs units) where G is the gravitational constant, M is mass and R is the radius of the star.

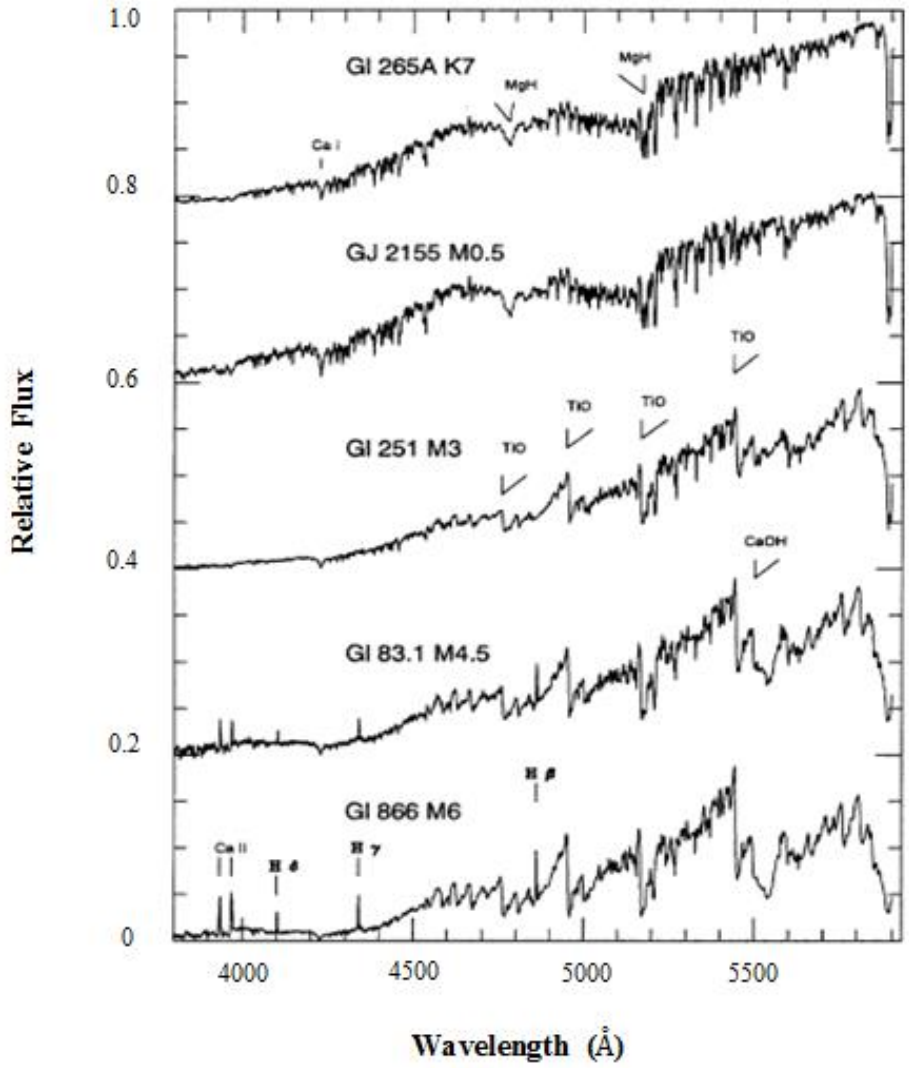

Figure 1.2 Blue-green spectra of five K/M dwarfs with different types. The prominent bands and atomic features are identified. (Taken from Reid & Hawley, 2000)

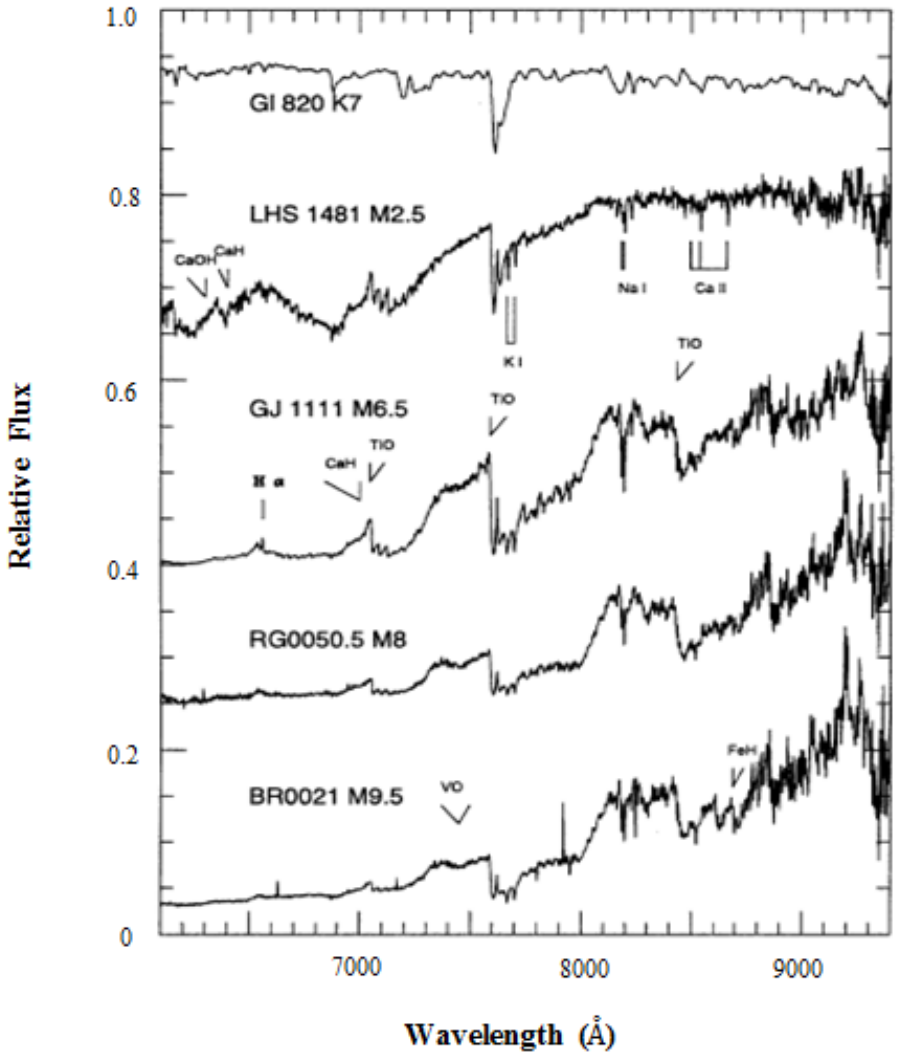

Figure 1.3 Red spectra of five K/M dwarfs with different types. The prominent bands and atomic features are identified. (Taken from Reid & Hawley, 2000)

Chapter 2

Model Atmospheres and Synthetic Colours

2.1 *Introduction*

Electromagnetic radiation is the only type of information we receive from stars. Accordingly, the modeling of stellar atmospheres, which is a powerful tool for understanding these objects, is based upon the knowledge obtained from their spectra as well as fundamental physical principles. Modeling can be accomplished using computer programs, and great progress has been made in this area over the past generation. Noticeably, the modeling of the atmospheres of low mass stars has significantly been improved to the point where there is now a good agreement with observations.

Among the most advanced, yet general-purpose computer codes for the modeling of stellar atmospheres is PHOENIX. It can calculate atmospheres and spectra of all main sequence stars, including cool stars as well as brown dwarfs[28], giants and white dwarfs[29]. This model atmosphere

[28] A brown dwarf is a substellar object whose mass is not sufficient to sustain hydrogen fusion in its cores, in contrast with main sequence stars (taken from: http://en.wikipedia.org/wiki/Brown_dwarf).

[29] A white dwarf is a stellar remnant composed mostly of electron-degenerate matter. For more details see: http://en.wikipedia.org/wiki/White_dwarf

code was first established by Peter Hauschildt in 1990's (e.g. Hauschildt et al, 1997) and is regularly updated and made available online[30].

Although there may remain some serious limitations in the PHOENIX code, it is able to provide a reasonably complete description of the spectra of stellar atmospheres. It is most often desirable to build a grid of models for a particular study and there are thousands of models in a typical grid. However, the line lists are far too large for the memory of a single computer or even multi-CPU workstations. Fortunately, current supercomputers allow very efficient parallel computing[31] to run PHOENIX in reasonable times (typically two hours per model), and in this way large grids of model atmospheres and synthetic spectra can be generated.

A detailed description of the PHOENIX code for low-mass stars is presented in section 2.2. The most commonly used model atmosphere grids obtained from PHOENIX are briefly described in Section 2.3. Finally, in section 2.4, the method for the calculation of synthetic magnitudes is explained and the loci of constant temperature and constant metallicity in colour – colour diagrams are shown and compared for different values of surface gravity.

2.2 *Model Atmosphere PHOENIX for Low-Mass Stars*

PHOENIX is a state-of-the-art stellar and planetary atmosphere code. It is able to solve one-dimensional or three-dimensional radiative transfer equations[32] in both plane-parallel and spherical symmetric atmospheres[33]. It also allows deviations from the local thermodynamic equilibrium (LTE) for several elements but mostly assumes LTE.

In PHOENIX, grids of models for cool stars and brown dwarfs basically have a wide range of parameters as below:

[30] See: http://www.hs.uni-hamburg.de/EN/For/ThA/phoenix/index.html

[31] This is a form of computation in which many calculations are carried out simultaneously.

[32] Radiative transfer is the propagation of energy in the form of electromagnetic radiation. The radiation traveling through a medium is affected by absorption, emission, and scattering processes. The radiative transfer equations describe these interactions mathematically (taken from: http://en.wikipedia.org/wiki/Radiative_transfer).

[33] There is a simplifying assumption in which the atmosphere is plane parallel, managing that physical variables depend only on one space coordinate, that is, the vertical depth. However, in stars where the photosphere is relatively thick compared to the stellar diameter, this is not a good approximation and an assumption of a spherical atmosphere is more appropriate.

- surface temperature: $500 \leq T_{eff} \leq 4{,}000$ K,
- metallicity: $-4.0 \leq [M/H] \leq 0.5$ dex,
- surface gravity: $\log(g) > 3.5$.

In general, the atmospheres of M stars are dominated by several molecular compounds such as H_2O, TiO, H_2, CO and VO. Most of the hydrogen is locked in molecular H_2 and most of the carbon is found in the form of CO. Their energy distribution is governed by millions of absorption lines of TiO, VO, CaH and FeH in the optical to near-IR, and H_2O and CO in the IR spectral region, which leave no window of true continuum.

The equation of state in PHOENIX contains 105 molecules, and up to 27 ionization stages of 39 elements. The models include over 300 molecular bands of TiO, VO, CaH and FeH, and about 2 million spectral lines out of 42 million atomic and 700 million molecular (H_2, CH, NH, OH, H_2O, MgH, SiH, C_2, CN, CO, SiO) lines. The modeling is carried out by assuming LTE, plane-parallel atmosphere[34], energy conversion and hydrostatic equilibrium[35].

H_2O, VO, and especially TiO opacities define a pseudo-continuum covering the entire flux distribution of these small stars. The optical pseudo-continuum of TiO is due to its vibrational bands. It has been shown that LTE is a poor approximation for Ti I line formation. Departures from LTE of the Ti I atom indirectly change the concentration of TiO. In PHOENIX, a fully self-consistent non-LTE (NLTE) treatment for a Ti I model atom with 395 levels and 5279 primary bound-bound transitions is included, and the effects of departures from LTE in this atom on the strengths of Ti I lines and TiO molecular bands are taken into account (Hauschildt et al. 1996, 1997).

At low temperatures ($T_{eff} < 3000$ K) dust formation occurs. Depending of the chemical composition of the atmosphere, the formation of over 600 gas-phase species and 1,000 liquids and crystals are considered, and the opacities of 30 different types of grains (e.g. Al_2O_3, $MgAl_2O_4$, iron, $MgSiO_3$, Mg_2SiO_4, amorphous carbon, SiC, and some calcium silicates) are included in PHOENIX.

[34] In the case of giant star models ($\log(g) < 3.5$) the assumption of a plane-parallel atmosphere is not appropriate anymore, so the spherical hydrostatic must be considered.
[35] See: http://www.hs.uni-hamburg.de/EN/For/ThA/phoenix/index.html

Dust formation can affect the atmosphere in two ways: by eliminating important opacity sources such as TiO and VO from the gas phase and the weakening of the corresponding spectral lines, and by adding new opacities produced by the grains themselves. The latter depend on the different behaviors of the macroscopic dust grains which can generally be classified as follows (Hauschildt & Baron 2005):

- If the dust particles remain as dust clouds in the layers where they originally formed, strong optical and IR opacities are produced by these clouds ("Dusty" models). These dust opacities are usually calculated from the base of the dust cloud up to the uppermost atmospheric layer.
- If all particles fall into deep atmosphere layers and settle below the line and continuum forming regions, they do not contribute to the opacity, resulting in no grain opacity detectable in the spectrum ("Cond" models).
- If a fraction of the grains settles out and form a depleted cloud, dust opacities will only be present in the cloud layers, but not necessarily in all the layers where the dust originally formed ("Settling" models).

There is some observational evidence showing that the Dusty models are more useful for T_{eff}> 1,800 K (late M dwarfs to early L dwarfs) whereas for giant planets and extreme T dwarfs the Cond models appear to be more appropriate. The updated model atmosphere grids including dust formation, which are applicable for M dwarfs, will be introduced in the next section.

2.3 *Model Atmosphere Grids for Low-Mass Stars*

Among all model atmosphere grids constructed by PHOENIX, the most successful ones are[36]

- NextGen (very low mass stars, no dust formation)
- AMES-Cond (brown dwarfs/extrasolar planets without irradiation, no dust opacity)
- AMES-Dusty (brown dwarfs/extrasolar planets without irradiation, with dust opacity)
- BT-Settl (stars/brown dwarfs/planets without irradiation, with a cloud model)

[36] http://perso.ens-lyon.fr/france.allard/

BT-Settl is a new model atmosphere grid, which is an update to AMES-Cond/Dusty models (Allard et al. 2012). This model has shown to be the most successful in reproducing the spectroscopic and photometric properties of M dwarfs. There are two versions of the BT-Settl model grid. The first one (BT-Settl/AGSS2009[37]) was computed using the PHOENIX code updated for:

- The Barber et al. (2006) water, the Homeier et al. (2003) methane, the Sharp & Burrows (2007) ammonia, and the Tashkun et al. (2004) CO_2 opacity line lists,
- The solar abundances revised by Asplund et al. (2009),
- A cloud model accounting for the mixing properties and resulting diffusion mechanism prescribed by the radiation hydrodynamics[38] (RHD) simulations of Freytag et al. (2010).

The grid covers the whole mass- range of stars to young planets with $400 \leq T_{eff} \leq 70{,}000$ K, $-0.5 \leq \log(g) \leq 5.5$, and $-4.0 \leq [M/H] \leq 0.5$ dex, and includes α-element[39] enhancement ([α/H]) between 0.0 and 0.6. This model agrees well with M dwarfs as late as M6. Later-type M dwarfs are affected by dust formation, and cloud modeling is therefore required to understand their properties. It has been demonstrated that the cloud model in this version is not efficient enough to reproduce dust formation in late type M stars.

The second, newer version of BT-Settl grid (BT-Settl/CIFIST2011[40]) can model M dwarfs adequately using up-to-date opacities and the revised solar abundances by Caffau et al. (2011). This version uses updates to the atomic and molecular line broadening and the TiO line list from Plez (1998). This list provides a more accurate description of the TiO bands in M dwarfs. This model grid gives an unprecedented fit quality for M dwarfs (Allard et al. 2013). In our study, we have used this new version of the BT-Settl grid and calculated the corresponding synthetic

[37] The model grid is available online: http://phoenix.ens-lyon.fr/Grids/BT-Settl/AGSS2009/

[38] A fluid interacting with electromagnetic radiation gains or loses energy and momentum through the emission, absorption and scattering of photons. Radiation hydrodynamics is a set of techniques used to model the resulting flows. The intensity of the radiation field and the optical depth of the fluid describe many important properties of the system, leading to a specific modeling approach (taken from: http://www.scholarpedia.org/article/Radiation_hydrodynamics).

[39] α- elements have atomic numbers $Z \leq 22$ and are C, N, O, Ne, Mg, Si, S, Ar, Ca, and Ti. These elements are synthesized by alpha-capture prior to the silicon fusing, a precursor to Type II supernovae. For more details see: http://en.wikipedia.org/wiki/Alpha_process

[40] The model grid is available online: http://phoenix.ens-lyon.fr/Grids/BT-Settl/CIFIST2011/

colours for the range 3000 $\lesssim T_{eff} \lesssim$ 4,200 K (corresponding to spectral types around between M4.5 and K6.5).

2.4 *Synthetic Colours*

Our grid is taken from BT-Settl/ CIFIST2011 consisting of 91 models with temperatures ranging from 3,000 to 4,200 K (in steps of 100 K), with metallicities between -2.5 and 0.5 (in steps of 0.5) and with surface gravity log (g) = 5.0 which is a relatively good approximation for M dwarfs.

We first calculated synthetic magnitudes and colours of SDSS and 2MASS filter bandpasses (*u*, *g*, *r*, *i*, and *z*. see Chapter 5 for more details). Since all fluxes in the synthetic spectra of BT-Settl grids are expressed in units of ergs/sec/cm^2/Å, for consistency we used the energy form (versus photon counting form) of formulation:

$$f_\lambda(S_x) = \frac{\int_0^\infty F_\lambda(\lambda) S_x(\lambda) d\lambda}{\int_0^\infty S_x(\lambda) d\lambda} \quad (2.1)$$

where λ is the wavelength, F_λ is the monochromatic energy distribution, f_λ is the flux and S_x is the dimensionless response function[41] of the photometric broadband filter x. By substituting $f_\lambda(S_x)$ into the equation below, the synthetic magnitude m_i can be calculated:

$$m_x = -2.5 \log [f_\lambda(S_x)] + k_x \quad (2.2)$$

where k_x is the photometric zeropoint. Through eight SDSS-2MASS broad-band filter magnitudes (*ugrizJHK)*, 21 different colours for our 91 models were calculated. Our synthetic colours are in very good agreement ($\sim$ 0.03 mag) with those calculated by Allard et al.[42] which can be considered as a successful test of our calculations. It is important to note that to compare our calculated synthetic colours fairly with data in current catalogues, the synthetic magnitudes

[41] The filter response functions of most important surveys can be found in the Filter Profile Service of Spanish Virtual Observatory (SVO).
[42] http://perso.ens-lyon.fr/france.allard/

of SDSS filters were calculated in the AB magnitude system[43] (the zeropoint is k = -48.6) while for 2MASS the magnitudes were computed in the Vega magnitude system[44]. We calculated the zeropoints of 2MASS broad-band filters (*JHK*) using the available energy distribution of Vega, and used these in computing synthetic magnitudes. The difference between these zeropoints (i.e., k_J-k_H, k_J-k_K, k_H-k_K) is in very good agreement with published values. The zeropoints corresponding to the eight filters (*ugrizJHK*) are arranged in Table 2.1. Some synthetic colours of SDSS-2MASS along with corresponding temperatures are arranged in Table 2.2, respectively. Each row corresponds to the metallicity range [-2.5,+0.5]. As an example, we represented the synthetic (*i*-*K*) - (*g*-*r*) colour-colour diagram in the SDSS-2MASS filter sets for temperatures from 3000 to 4000 K in Figure 2.1.

Although many M dwarf studies assume log (g) = 5.0, this may not be a good approximation for all M dwarfs. According to the empirical surface gravity – mass relation of M dwarfs in Bean et al. (2006, Equation 2 in their paper[45]), for the stellar mass spanning from 0.1 to 0.6 $M_\odot$ (corresponding to the spectral type ranging from M0 to M6), the values of surface gravity are between 4.63 and 5.22 dex. In fact, early type M stars (M0-M1) have surface gravities which differ from log (g) = 5.0 by up to 0.2 dex. Figures 2.2 compares the isometallicity and isotemperature curves for different values of surface gravity, log (g) = 4.5, 5.0 and 5.5, with temperatures between 3000 and 4000 K in the synthetic (*i*-*K*)-(*g*-*r*) colour-colour diagram of SDSS-2MASS. There is a clear shift in these curves from one value of log (g) to the other. Obviously, for a more accurate treatment, the variation of synthetic colours in terms of surface gravity must be taken into account.

Table 2.1 The zeropoints of each SDSS-2MASS filter bands

Filter	***u***	***g***	***r***	***i***	***z***	***J***	***H***	***K***
Zeropoint	-48.600	-48.600	-48.600	-48.600	-48.600	-49.510	-49.995	-50.463

[43]The AB magnitude system defines the colours of a source with a flat energy distribution to be zero. That is, an object with F_λ = constant has the same magnitude in all bandpasses.

[44] By definition, Vega's magnitudes are zero in all filters in the Vega magnitude system.

[45]This is a polynomial of third degree for log (g) as a function of stellar mass.

Table 2.2 Effective temperatures and BT-Settl synthetic colour ranges corresponding to metallicities between -2.5 and +0.5 and surface gravity log (g) = 5.0 for SDSS and 2MASS filters

T_{eff}	*g-r*	*g-i*	*r-i*	*r-K*	*g-J*	*i-J*
3000	1.144-2.192	3.026-3.414	1.222-1.887	3.615-5.541	5.582-5.856	2.168-2.830
3100	1.075-2.130	2.810-3.237	1.107-1.735	3.521-5.200	5.281-5.452	2.095-2.642
3200	1.047-2.060	2.680-3.066	1.006-1.633	3.403-4.954	4.951-5.179	2.023-2.499
3300	1.030-1.967	2.577-2.862	0.895-1.547	3.306-4.743	4.656-4.944	1.941-2.367
3400	1.016-1.859	2.436-2.655	0.796-1.430	3.199-4.508	4.372-4.684	1.854-2.238
3500	0.990-1.752	2.306-2.470	0.718-1.361	3.096-4.337	4.139-4.477	1.775-2.126
3600	1.003-1.642	2.183-2.298	0.656-1.241	2.999-4.111	3.933-4.258	1.699-2.014
3700	1.009-1.537	2.076-2.147	0.608-1.138	2.916-3.904	3.737-4.057	1.633-1.910
3800	1.048-1.434	1.967-2.063	0.564-1.015	2.836-3.669	3.547-3.863	1.571-1.800
3900	1.023-1.327	1.845-1.981	0.523-0.958	2.761-3.538	3.360-3.720	1.515-1.739
4000	1.071-1.251	1.724-1.886	0.489-0.815	2.682-3.281	3.196-3.523	1.470-1.637
4100	1.098-1.209	1.605-1.805	0.458-0.707	2.592-3.077	3.025-3.362	1.420-1.557
4200	1.074-1.176	1.500-1.735	0.426- 0.647	2.510-2.949	2.873-3.243	1.373-1.508

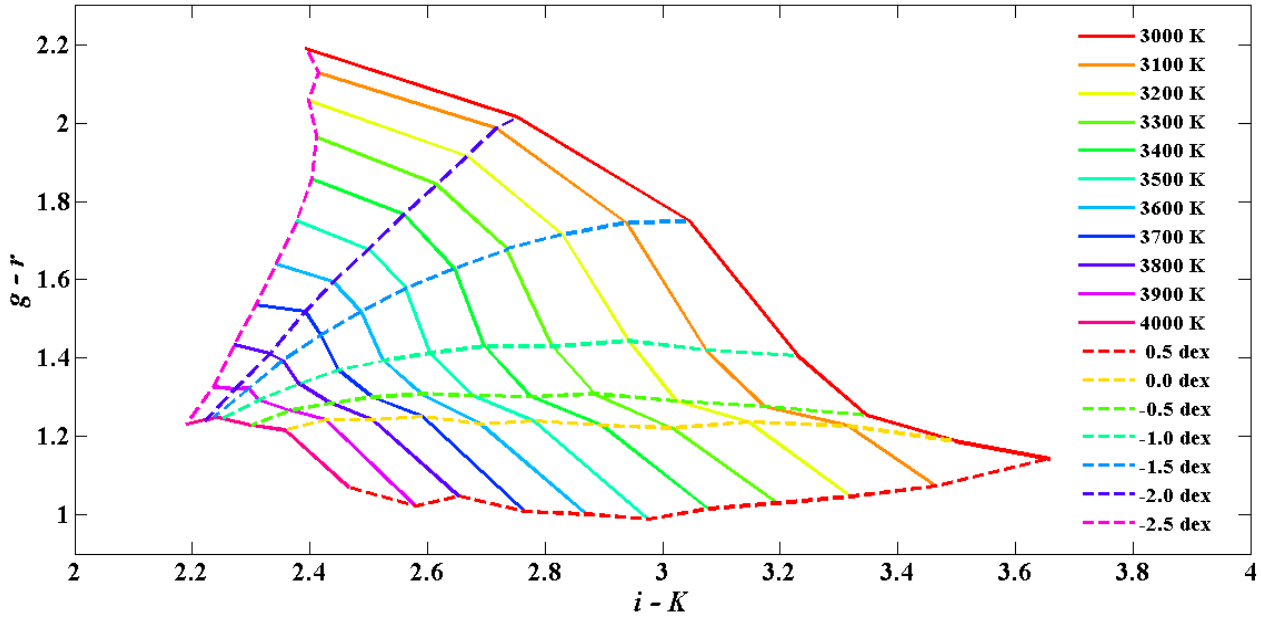

Figure 2.1 The synthetic (*i-K*) - (*g-r*) colour-colour diagram of SDSS-2MASS filter bandpasses. The loci of constant temperatures (solid lines) and the loci of constant metallicity (dashed lines) are colour-coded

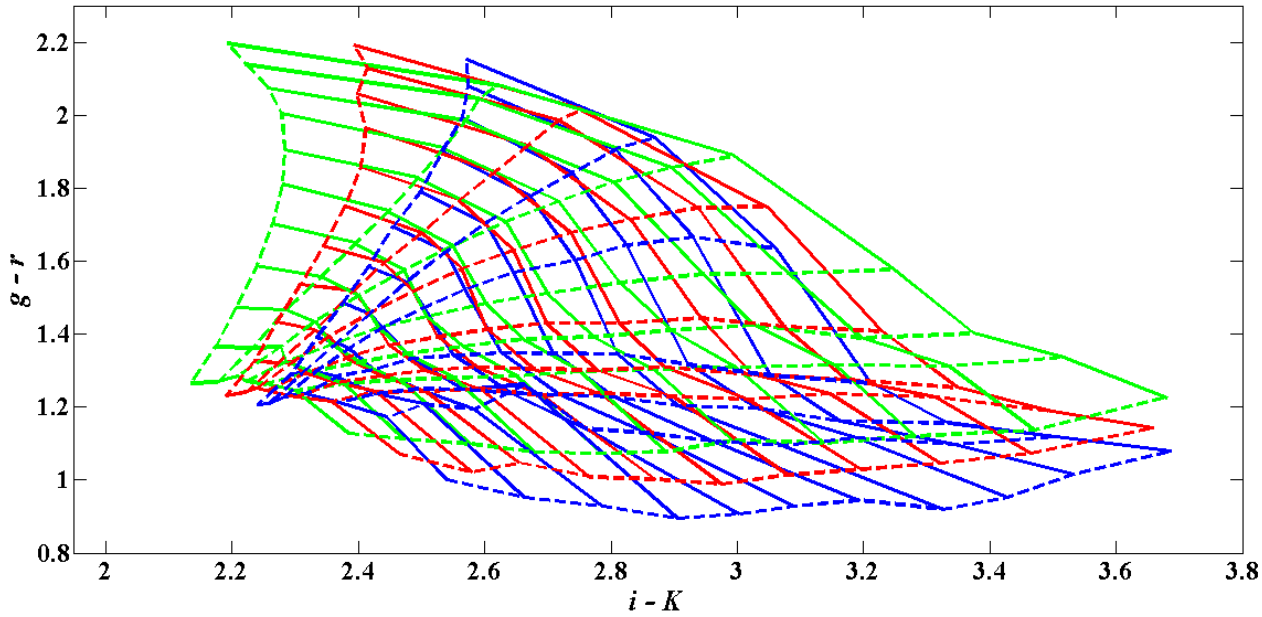

Figure 2.2 The synthetic (*i-K*) - (*g-r*) colour-colour diagram of SDSS-2MASS filter bandpasses for different values of log (g) = 4.5, 5.0 and 5.5, shown by blue, red, and green colours, respectively. The solid lines represent the loci of constant temperature and the dashed lines show the loci of constant metallicity.

Chapter 3

Techniques for Determination of M-Dwarf Metallicity

3.1 *Introduction*

In the last two decades different techniques have been established to estimate the metallicity and temperature of M dwarfs, giving consistent results in many cases. In general, the more widely used methods for metallicity and temperature determination can be divided into two main groups, spectroscopic and photometric, in which parameters are determined through analyses of spectra or photometry of stars. In most recent techniques for metallicity determination, M dwarfs in binary systems[46] with an F-, G-, or K-type star, which has a measured metallicity, are used. It is assumed that members of a binary (or a cluster) which formed from the same molecular cloud should have the same chemical composition. Diffusion and nuclear enrichment processes which can change atmospheric abundances should not have any measurable effect on these main sequence stars. Hence, M dwarfs in such double systems can be assigned their FGK-dwarf companions' metallicity. There are some well-established methods to determine the

[46] It should be noted that such binaries must have large angular separations so that each component can be observed separately.

metallicity of FGK stars which can be applied to the primary of such a binary. In this way, the metallicity of the secondary (which is an M dwarf) is taken to have the same metallicity as the primary. The metallicities obtained in this way are usually used for empirical calibrations of M-dwarf metallicity, both spectroscopic and photometric.

In this Chapter, the most commonly used spectroscopic and photometric techniques for determining the metallicity of M dwarfs are described in some detail (Sections 3.2and 3.3, respectively). These methods underlie our photometric metallicity calibration (Chapter 4).

3.2 *Spectroscopic Techniques*

Spectroscopic analysis is one of the most powerful tools to determine atmospheric parameters and chemical abundances of stars. There are several spectroscopic methods for deriving stellar parameters such as the metallicity of M dwarfs. We will address the most important methods of these kinds along with their applicability in the following subsections.

3.2.1 *Fitting Models with observed Spectra*

One way to interpret observed spectra in terms of physical parameters such as temperature, metallicity and surface gravity is to use model atmospheres. Gizis (1997) employed the Extended Model Grid computed by Allard & Hauschildt (1995) to estimate the temperature and metallicity of M dwarfs. The extended models had been computed for metallicities between [M/H] = 0.0 and [M/H] = -4.0 in steps of 0.5 dex. Gizis (1997) chose the models with temperatures in the M-dwarf regime i.e., between 2,500 K and 4,000 K in steps of 100 K. Since both theory and observations have indicated M dwarfs have log (g) ≈ 5.0, the analysis was restricted to models with log (g) = 5.0. In this method the spectral region between 6200 and 7300 Å were compared by minimizing the least squares difference (χ^2) between the observed spectrum and the models. The synthetic spectra were fitted to the TiO and CaH features visible in moderate-resolution spectra ($\lambda/\Delta\lambda \approx 2{,}000$) to measure the metallicity of stars. The sample of cool stars under study covered the range from solar metallicity stars to the most extreme subdwarfs. More precisely, Gizis (1997) classified stars as M dwarfs (dM), M subdwarfs (sdM), and M extreme subdwarfs (esdM) which correspond to metallicity [M/H] ≈ 0.0, -1.2 and -2.0 dex, respectively. This

metallicity scale was qualitatively in agreement with theoretical HR diagram and the Hubble Space Telescope (HST) globular cluster measurements. The agreement of these three methods indicated the metallicity scale was accurate within ~ 0.5 dex.

Several other researchers have also estimated the metallicity as well as the temperature of low-mass dwarfs by fitting synthetic spectra to some low- and moderate-resolution ($400 < \lambda/\Delta\lambda < 6000$), observed spectra including atomic and molecular spectral features (Jones et al. 1995, 1996; Viti et al. 1997; Leggett et al. 2002). In a recent work (Rajpurohit et al. 2013), the effective temperatures of 152 M stars have been estimated by matching their low- or moderate-resolution[47], optical spectra with the most recent BT-Settl synthetic spectra (see Chapter 2) via a χ^2 minimization technique.

The comparison of high resolution spectra with synthetic models of stellar atmospheres provides a reliable implement to study stellar properties. Valenti et al. (1998, hereafter V98) pioneered the use of spectral synthesis to determine M dwarf parameters to high precision. They fitted synthetic spectra of TiO and some atomic lines using the NextGen model atmospheres, to a high quality ($\lambda/\Delta\lambda \approx$ 120,000) observed spectrum of Star Gl 725 B (with spectral type M3.5) to determine its stellar parameters (T_{eff} = 3170 ± 71 K, log (g) = 4.77 ± 0.14, and [M/H] = -0.92 ± 0.07 dex).

Bean et al. (2006) tested and improved the V98 technique using high resolution, high signal-to-noise ratio (S/N) observations of five visual binaries, containing FGK-dwarf primaries and M-dwarf secondaries[48]. Their goal was to determine whether the V98 method could yield metallicities for M-dwarf secondaries consistent with those derived from FGK star primaries. For this purpose, they obtained the iron abundances of the primaries by fitting synthetic spectra to profiles of 30 selected Fe I lines in observed spectra. In this work, [Fe/H] was approximately taken equal to the overall metallicity [M/H]. Synthetic spectra were generated for each profile line region by means of the MOOG code[49] (Sneden 1973). The match between the synthetic

[47] 97 stars were observed with low resolution spectra and 55 stars with mid resolution spectra.
[48] The spectral types of the components span from F7 to K3 for the primaries and from M0.5 to M3.5 for the secondaries.
[49] http://www.as.utexas.edu/~chris/moog.html

spectra and observed spectra was evaluated by the fitting algorithm; new parameters (such as metallicity, effective temperature, and surface gravity) were selected and the algorithm continued to iterate until the parameters which minimized χ^2 were achieved.

To determine metallicities of M-dwarf secondaries, Bean et al. (2006) used the V98 approach in which synthetic spectra are matched to two observed spectral regions of an M dwarf spectrum; one region contained strong atomic lines (8670-8700 Å), and another one contained a TiO bandhead (7078-7103 Å). They found that the metallicities of M dwarfs derived in this manner are lower than the values of the primaries by an average of 0.56 dex. They considered that this systematic discrepancy could be reduced by improvements on the method and the model atmospheres. Their modified approach along with new model atmospheres provided a technique for determining metallicities of M dwarfs consistent to 0.11dex with the techniques applied to FGK stars (for details of the modification to the V98 approach see Bean et al. 2006).

Önehag et al. (2011) took advantage of the absence of the large molecular contribution in the infrared *J*-band and derived the metallicity of eight M dwarfs based on best-fit synthetic spectra to the high-resolution ($\lambda/\Delta\lambda \approx 50{,}000$) observed spectra. They tested their approach by using FGK+M binaries and concluded that spectroscopic abundance analysis in the *J*-band provides a reliable method for establishing the metallicity scale for M dwarfs.

del Burgo et al. (2011) characterized a sample of 11 nearby, late-type M dwarfs with spectral types between M5 and M9.5. They derived the effective temperature and surface gravity of the stars by comparing high-resolution ($\lambda/\Delta\lambda\approx$ 20,000), NIR spectra with synthetic model atmospheres. Their results were in good agreement with those found in the literature.

Most recently, Rajpurohit et al. (2014) presented high-resolution ($\lambda/\Delta\lambda\sim$ 40,000) spectra of 21 subdwarfs, covering the optical region from 6400 Å up to the NIR at 10,000 Å, and produced an effective temperature versus spectral type relation all over the subdwarf spectral sequence. To estimate the metallicity of these dwarfs, they chose the spectral interval from 8440 Å to 8900 Å where molecular absorptions are relatively weak and atomic lines appear clearly, and then performed a detailed comparison of line profiles of individual elements such as Fe I, Ca II and

Ti I between those from the synthetic spectra calculated by the BT-Settl models and those from the observed spectra.

3.2.2 *Equivalent widths of Atomic Absorption Lines in High-Resolution Spectra*

Atomic spectral analyses of low-mass stars are severely hindered by strong molecular absorption bands, especially at optical and near infrared (NIR) wavelengths. In the regions that these molecular bands are strong, they blend with the atomic lines such that it is impossible to determine chemical abundances of elements using only equivalent width[50] analysis. In the regions within the molecular bands, there is often a multitude of closely spaced weak lines, forming a pseudo continuum well below the true continuum level. As a result, the identification of the continuum level in a low-mass dwarf spectrum is often challenging. However, in early-type M and late-type K dwarfs, there are some specific regions essentially with low molecular line opacity, and only high S/N and high-resolution optical (or NIR) spectra provide reliable abundance analyses for these dwarfs.

Woolf and Wallerstein (2004) estimated the metallicity of Kapteyn's star (HD 33793, spectral type ≅ M1) by determining the chemical abundances of 12 elements[51] through the high-resolution ($\lambda/\Delta\lambda \approx$ 33,000) spectrum of the star. The chemical abundances were determined by making use of the local thermodynamic equilibrium (LTE) stellar line analysis program MOOG. They measured the equivalent widths (EWs) of the atomic lines present in the spectrum of the star using IRAF[52] software. The chemical abundances of Kapteyn's star were calculated by using the measured EWs of the atomic spectral lines, except for Rb and V whose abundances were derived using the synthetic spectrum analysis[53]. They found an iron abundance of [Fe/H] =

[50]The equivalent width of a spectral line is a measure of the area of the line on an intensity- wavelength diagram. It can be determined by forming a rectangle with a height equal to that of the emission, and finding the width such that the area of the rectangle is equal to the area of the spectral line, taken from:
http://en.wikipedia.org/wiki/Equivalent_width

[51] Al, Ca, Sc, Ti, V, Cr, Fe, Ni, Rb, Y, Zr, Ba I and Ba II

[52] Image Reduction and Analysis Facility (http://iraf.noao.edu/) is a general purpose software system written at the National Optical Astronomy Observatory (NOAO) which is designed for the reduction of astronomical images in pixel array form.

[53]Woolf and Wallerstein (2004) used the *synth* driver of MOOG for these two elements. Using synthetic spectrum analysis, they tested whether hyperfine splitting affected abundances that they had already determined by EW

-1.13 ± 0.01 and a weighted mean metallicity of [M/H] = -0.98 $\pm$ 0.1for the star. This metallicity can be compared with previous studies for this star: [M/H] = -1.5 ± 0.5 (Gizis 1997), [M/H] = -1.0 ± 0.3 (Jones et al. 2002), [M/H] = -1.75 ± 0.18 (Krawchuk et al. 2000).

Woolf and Wallerstein (2005) estimated the metallicities of 35 M and K dwarf by calculating the abundances of only two elements, Fe and Ti, using the EWs measured from high-resolution spectra. For each star, they obtained the NextGen model atmosphere (see Chapter 3) for the photometrically estimated temperature and surface gravity, and an assumed metallicity of [M/H] = -1.0 as starting values. The calculated Fe and Ti abundances were exploited to estimate the model atmosphere metallicity to be used in the next iteration. This procedure was repeated until the metallicity derived using the Fe and Ti abundances equalled the model atmosphere metallicity.

3.2.3 *Empirical Calibrations Based on Molecular Band Indices in Low-to-Moderate- Resolution, Optical Spectra*

Although accurate values of metallicity for M dwarfs can be estimated using atomic line EWs and spectral synthesis in high resolution spectra, the development of less complicated methods applicable for fainter stars is needed. Due to the intrinsic faintness of M dwarfs, only a few of these cool stars are close enough for high resolution spectra to be measured (Woolf and Wallerstein 2006). The optical and NIR spectra of M dwarfs are dominated by molecular absorption bands of metal oxides and hydrides, most prominently TiO and CaH bands (Bessel 1991). The ratio between of the oxide and hydride bands has long been known as a metallicity indicator (Bessel 1982). Several metallicity calibrations for M dwarfs (as well as for sdM and esdM) have been made based on four spectroscopic indices[54] (CaH1, CaH2, CaH3 and TiO5) defined by Reid et al. (1995).

---

analysis. Rb and V were the only elements changed their abundances when using hyperfine structure test. This investigation is beyond the scope of the thesis (For more details see: Woolf and Wallerstein 2004).

[54] The strength of each molecular band is measured with a spectral index defined as the magnitude of the difference between the integrated flux within a wavelength window containing the given feature and the integrated flux inside a nearby window, or windows, used to define the continuum (see for example, Carrera 2012).

Woolf and Wallerstein (2006) reported a metallicity calibration using CaH2 and TiO5 measured in moderate-resolution ($\lambda/\Delta\lambda \approx$ 3,000), flux-calibrated spectra. This method can be applied to stars at least 3 magnitudes fainter and considerably more distant than stars which can be observed at high-resolution (Woolf and Wallerstein 2004, Woolf and Wallerstein 2005 or Bean et al. 2006). To test their method, Woolf and Wallerstein (2006) used binaries with FGK-dwarf primaries and M-dwarf secondaries and realized this method gives reliable metallicities for M stars warmer than 3,500 K (i.e., stars earlier than M2).

Lépine et al. (2007) introduced a metallicity parameter, $\zeta_{\mathrm{TiO/CaH}}$, defined by:

$$\zeta_{\mathrm{TiO/CaH}} = \frac{1-\mathrm{TiO5}}{1-[\mathrm{TiO5}]_{Z_\odot}} \tag{3.1}$$

where

$$[\mathrm{TiO5}]_{Z_\odot} = -0.164\,(\mathrm{CaH2}+\mathrm{CaH3})^3 + 0.670\,(\mathrm{CaH2}+\mathrm{CaH3})^2$$

$$-0.118\,(\mathrm{CaH2}+\mathrm{CaH3}) - 0.050 \tag{3.2}$$

This index quantifies the weakening of the TiO bandstrength due to a metallicity effect, with values ranging from $\zeta_{\mathrm{TiO/CaH}} = 1$ for stars of near-solar metallicity to $\zeta_{\mathrm{TiO/CaH}} \cong 0$ for the most metal-poor (and TiO depleted) subdwarfs. Using this metallicity index, Lépine et al. (2007) redefined the classification system of M dwarfs on the MS (i.e., dM, sdM, and esdM, initially suggested by Gizis 1997, see above) and improved upon the previous scheme by introducing a new class, named ultrasubdwarfs (usdM), as one of the sequences in formal classification standards.

Woolf et al. 2009 empirically calibrated a molecular index-metallicity relation using 88 M dwarfs with known metallicity (derived from high-resolution spectra) as follows:

$$[\mathrm{Fe/H}] = a + b\,\zeta_{\mathrm{TiO/CaH}} \tag{3.3}$$

where $a = -1.685 \pm 0.079$ and $b = 1.632 \pm 0.096$. With this calibration, molecular indices measured from moderate-resolution ($\lambda/\Delta\lambda \gtrsim$ 3,000) spectra can be employed to estimate the

metallicity of M stars with 3,500 $\lesssim T_{eff} \lesssim$ 4,000 K and -1.5 $\lesssim$ [Fe/H] $\lesssim$ +0.05 dex. This calibration is accurate to 0.3 dex for stars with [Fe/H] > -1.0 dex and to 0.5 dex for stars with [Fe/H] < -1.0 dex.

Using a new calibration sample, Mann et al. (2013a) recalibrated the Equation (3.3) as follows:

$$[Fe/H] = 1.55\,\zeta_{TiO/CaH} - 1.62 \quad (3.4)$$

with R_{ap}^2[55] = 0.58 and derived a relation for overall metallicity:

$$[M/H] = 1.29\zeta_{TiO/CaH} - 1.35 \quad (3.5)$$

with R_{ap}^2=0.52. Dhital et al. (2012) recalibrated the definition of $\zeta_{TiO/CaH}$, or ζ for simplicity, and showed that this new ζ could be a significantly better indicator of metallicity for early M-type dwarfs (between M0 and M3). Mann et al. (2013a) tested the parameter ζ defined in Lépine et al. (2007) by their sample and found that this parameter is not only sensitive to metallicity (and temperature) but also to some other stellar characteristics such as activity and surface gravity which could lead to an incorrect identification of some metal-poor stars as near-solar metallicity stars. They pointed out that although ζ correlates well with [Fe/H] for supersolar metallicities, it does not always diagnose metal-poor M dwarfs correctly. More importantly, Lépine et al. (2013) remarked that the parameter ζ, defined in Lépine et al. (2007) overestimated the metallicity of early-type M dwarfs while the parameter defined in Dhital et al. (2012) underestimated the metallicity of these stars, and redefined the index ζ.

3.2.4 *Empirical Calibrations based on Atomic and Molecular Indicators in Moderate-Resolution, NIR Spectra*

Measuring accurate stellar parameters from the optical spectra of M dwarfs is not straightforward. As the abundances of diatomic and triatomic molecules in the photospheric layers increases with spectral subtype, the forest of weak lines eventually erases the spectral

[55] The adjusted square of the multiple correlation coefficient; a R_{ap}^2 closer to 1 implies that the model accurately explains the variance of the sample, while R_{ap}^2 indicates that it can explain none (for more details see, e.g., Mann et al. (2013a)).

continuum and makes a line-by-line spectroscopic analysis very difficult. Employing metallicity and temperature tracers in the infrared region of M dwarf spectra can give more accurate values of fundamental parameters.

Bonfils et al. (2005) were first to realize that those M dwarfs which are in FGK+M binary systems, very likely have the same metallicities as the readily-measured metallicity of their FGK-dwarf companions, and then used these values for an empirical (photometric) calibration of M-dwarf metallicity. Using a sample of 17 such M dwarfs, Rojas-Ayala et al. (2010) presented a *K*-band calibration for estimating the iron abundances of an early-to-mid-type M dwarf (with a dispersion of 0.15 dex), based on a *K*-band water index, defined by Covey et al. (2010), and the strength of several spectral lines (i.e., the Na I doublet and the Ca I triplet), which all can be measured in moderate-resolution ($\lambda/\Delta\lambda \approx 2700$) *K*-band spectra.

Terrien et al. (2012) updated the calibration of Rojas-Ayala et al. (2010) through their calibrator sample, including 22 M dwarfs having FGK companions with reliable metallicities. They also performed a spectral analysis to estimate the metallicity of M dwarfs via moderate-resolution ($\lambda/\Delta\lambda \approx 2{,}000$) *H*-band spectra by measuring the strengths of three metallicity-dependent features and an *H*-band H_2O index from Covey et al. (2010), with an accuracy of ± 0.12 dex.

Rojas-Ayala et al. (2012) developed a modified water index as defined by

$$H_2O\text{–}K2 = \frac{<F(2.070-2.090)>/<F(2.235-2.255)>}{<F(2.235-2.255)>/<F(2.360-2.380)>} \quad (3.6)$$

where $<F(a\text{-}b)>$ denotes the median flux level in the wavelength range defined by *a* and *b* in μm. In their sample, there were 68 stars having KHM spectral types (see Chapter 1) which allowed them to calibrate this index as a proxy for KHM spectral type as follows:

$$\text{M subtype} = A + B\,(H_2O\text{–}K2) \quad (3.7)$$

where $A = 24.699 \pm 0.930$ and $B = -23.788 \pm 1.067$. They also presented revised formalisms to determine [Fe/H] and [M/H] calibrated by 18 M dwarfs (one M dwarf was added to the sample of Rojas-Ayala et al. 2010) in binary systems with reliable metallicity estimates (as inferred from corresponding FGK primaries):

$$[Fe/H] = A_1 + B_1 \frac{Na\ I_{EW}}{H_2O\text{–}K2} + C_1 \frac{Ca\ I_{EW}}{H_2O\text{–}K2} \qquad \text{(RMSE=0.141 dex)} \qquad (3.8)$$

$$[M/H] = A_2 + B_2 \frac{Na\ I_{EW}}{H_2O\text{–}K2} + C_2 \frac{Ca\ I_{EW}}{H_2O\text{–}K2} \qquad \text{(RMSE=0.100 dex)} \qquad (3.9)$$

where A_1= -1.039 $\pm$ 0.170, B_1= 0.092 $\pm$ 0.023, C_1= 0.119 $\pm$ 0.033, A_2= -0.731 $\pm$ 0.120, B_2= 0.066 $\pm$ 0.016, and C_2= 0.083$\pm$ 0.023. Na I_{EW} and Ca I_{EW} stand for the equivalent widths of the atomic Na I and Ca I lines. It should be noted that due to the small calibration sample, the techniques of Rojas-Ayala et al. (2012) are restricted to only M dwarfs with spectral types between M0 and M4 and metallicities in the range of -0.5 < [Fe/H] < +0.4.

To extend the applicability ranges, Mann et al. (2013a) used a calibrator sample of 112 late-K and M dwarfs in common proper motion pairs with an FGK-type dwarf of known metallicity. They employed moderate-resolution, visible and NIR spectra of these stars to identify the largest possible set of ($\sim$ 120) metal-dependent spectral features as well as four temperature-sensitive parameters in the *JHK* and optical bands, and derived a set of metallicity relations for different spectral regions with RMSE $<$ 0.1 dex (Equations 29-34 in their paper). These new calibrations are applicable to dwarfs with spectral types from K7 to M5 and metallicities of -1.04 < [Fe/H] < 0.56 dex.

Mann et al. (2013b, hereafter M13b) collected a sample of late K- and M-dwarf planet hosts from the Kepler Objects of Interest (KOIs, Batalha et al. 2013) to explore the relation between the metallicity of the host stars and the size and multiplicity of the planets orbiting them. However, due to their low S/N observations, large errors arose when they applied the calibrations from Mann et al. (2013a) (who made high S/N observations) on features blueward of 6000 Å. To avoid S/N errors, they recalibrated the optical metallicity relations of Mann et al. (2013a) to a single equation using only the indices redward of 6000 Å, yielding a RMSE of 0.08 dex:

$$[Fe/H] = 0.68F1 + 0.53F2 – 0.32F3 -1.0\ Colour1 – 0.26 \qquad (3.10)$$

where F1, F2, and F3 correspond to the equivalent widths of features at 8191-8225 Å , 8860-8880 Å, and 9179-9199 Å, respectively, and Colour1 is a temperature sensitive index from Hawley et al. (2002).

Mann et al. (2014) extended the previous studies of Mann et al (2013a, 2013b) to later-type M dwarfs with spectral types between M4.5 and M9.5 using 44 M dwarfs in wide binaries with an FGK- or early M-dwarf primary of known metallicity. They found a best fit in the *K*-band as follows:

$$[Fe/H] = 0.131\ (Na\ I_{EW}) + 0.210\ (Ca\ I_{EW}) - 3.07\ (H_2O\text{–}K2) + 1.341 \qquad (3.11)$$

which is accurate to ~ 0.07 dex for M dwarfs with -0.58 < [Fe/H] < +0.56 dex.

After a carful investigation of 27 spectral lines and 10 spectral indices for metallicity-sensitive features, Newton et al. (2014) derived a relation for metallicity in terms of the EW of the Na I doublet at 2.2 μm, as the only metallicity indicator, with a standard deviation of ≅ 0.12 dex:

$$[Fe/H] = -1.96 + 0.569\ (Na\ I_{EW}) - 0.0392\ (Na\ I_{EW})^2 \qquad (3.12)$$

which is calibrated for $Na\ I_{EW}$ between 3 and 7.5 Å, corresponding to metallicitiesof -0.6 < [Fe/H] < 0.3 dex and for spectral types from M1 to M5. Their calibrations sample included 36 M dwarfs in common proper pair with an F-, G-, or K-dwarf primary with reliable metallicity. Newton et al. (2014) showed that this metallicity calibration can also be extrapolated to metallicities as low as -1.0 dex and spectral types as late as M7[56].

3.3 *Photometric Techniques*

Although spectroscopic analyses have proven valuable to assess fundamental stellar properties and have considerably been improved in the last few years, there is a clear need for more straightforward and efficient methods to be established. For this purpose, several photometric approaches have been developed to evaluate the metal content of M dwarfs. There are also several theoretical and empirical colour-temperature relations which can be used to determine the

[56] Newton et al. (2014) compared the metallicities estimated for members of 22 M dwarf-M dwarf binary systems with a range of spectral types. This comparison indicated that Equation (3.12) can be extrapolated as late as M7.

effective temperature of M stars. In the following subsections the most widely used photometric approaches will briefly discussed.

3.3.1 *Colour-Absolute Magnitude Diagrams*

Bonfils et al. (2005) pointed out that lower-metallicity M dwarfs have a bluer *V-K* colour at a constant *K*-band absolute magnitude M_K, and used the position of a star in a M_K vs. *V-K* diagram as a useful metallicity indicator. As described in Neves et al. (2012), increased TiO and VO abundances in metal-rich M dwarfs shift the radiative flux from the visible range, where these species dominate the opacities, to the NIR. For a fixed mass, an increased metallicity also reduces the bolometric luminosity. These two effects work together to decrease flux at visible wavelengths, but they largely cancel out in the near infrared. Consequently, the absolute magnitude M_V of an M dwarf is very sensitive to its metallicity, while its near infrared absolute magnitude does not have such a sensitivity. As a result the position of a star in a colour-absolute magnitude diagram like the M_K versus *V-K* diagram can be used as a metallicity proxy. They derived a polynomial fit, relating metallicity to M_K and *V-K*.

Although the relation of Bonfils et al. (2005) has been used in several studies (for example, Jenkins et al. 2009), its application has been contested. By performing several tests, Johnson and Apps (2009) found that while the relation of Bonfils et al. (2005) could reasonably reproduce the metallicity of metal-poor M dwarfs, it underestimated the metallicities of their high metallicity stars by an average of 0.32 dex. They created an empirical model in which the distance of an M dwarf to the mean main sequence along M_K in the (*V-K*) - M_K plane indicated its metallicity[57]. Johnson and Apps (2009) argued the local M and FGK dwarfs should have the same metallicity distribution. In other words, the mean metallicity of a population of M dwarfs could be characterized by the easily-measured mean metallicity of a similar population of FGK stars. Accordingly, they equated their mean M dwarf metallicity with the value (-0.05 dex) derived from a volume-limited sample of FGK dwarfs (Valenti & Fischer 2005). They then assumed that the main sequence was an isometallicity contour with the metallicity equal to the mean value, and fitted a fifth-order polynomial to this contour by using a volume-limited sample of K and M dwarfs.

[57] Similar to the approach of Johnson et al. 2012 described in Section 3.3.2.

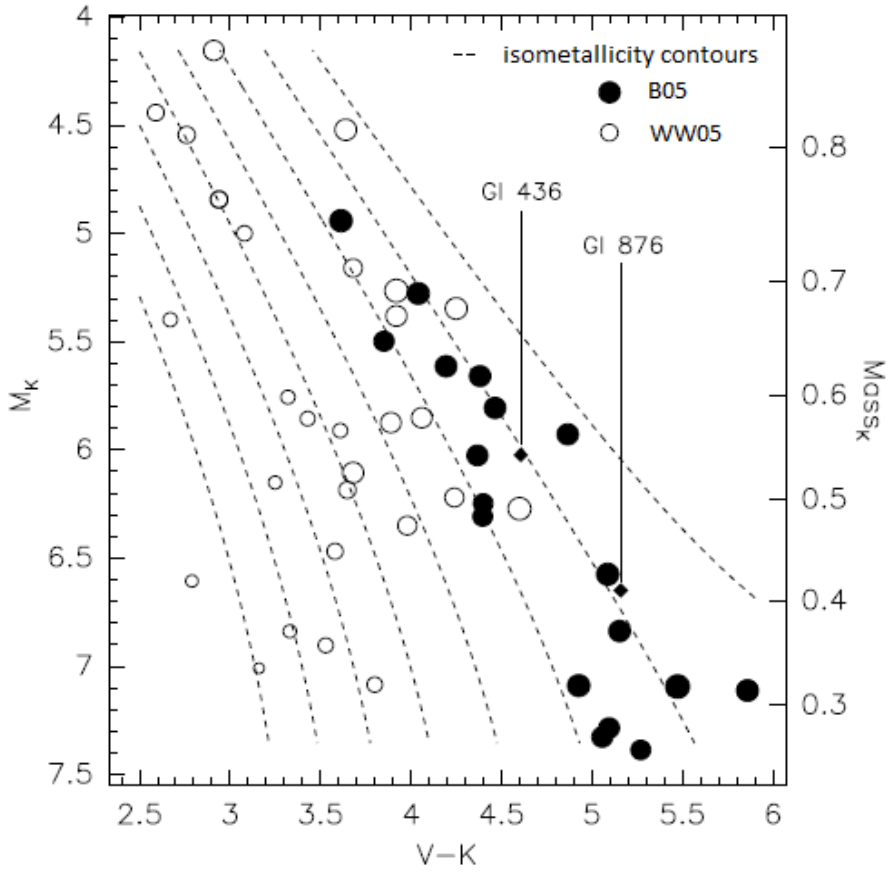

Figure 3.1 Colour-absolute magnitude diagram *V-K* vs. M_K from Bonfils et al. (2005). The filled circles correspond to stars from the calibration sample of Bonfils et al. (2005) and the open circles to that of Woolf and Wallerstein (2005). The symbol size is proportional to the metallicity. The dashed lines represent isometallicity contours obtained by the calibration of Bonfils et al. (2005). The right-hand axis shows masses from the *K*-band mass-luminosity relation in Delfosse et al. (2000).

Schlaufman & Laughlin (2010) improved upon Bonfils et al. (2005) and Johnson and Apps (2009) in two ways. First, they pointed out the various kinematic populations of the Milky Way have very different mean metallicities. Therefore, for M and FGK dwarfs in a given sample to have the same metallicity, matched kinematics is as important as volume completeness (see also Neves et al. (2012)). They demonstrated that a volume-limited, kinematically-matched sample of Sun-like stars gives a better estimated value of the mean M dwarf metallicity in the solar neighborhood. In this way, they measured a value of $\cong$ -0.17 $\pm$ 0.07 for the mean metallicity via such a sample drawn from the Geneva-Copenhagen Survey. Second, they used stellar evolution models and theoretical isochrones from Baraffe et al. (1998) to better parameterize metallicity in the (*V-K*) - M_K plane. They found out, with all other parameters constant, metallicity should best correlate with the horizontal shift in this plane. For this reason, they calculated the distance from

the M dwarf main sequence in the horizontal direction (i.e., *V-K*) for each M dwarf in their calibration sample. They then derived a linear fit with a dispersion of 0.14 dex (but with a higher dispersion of 0.19 dex assessed by the calibration sample of Neves et al. (2012)) by considering this distance as a metallicity indicator.

Neves et al. (2012) assembled a sample of M dwarfs which have a hotter FGK-dwarf companion with securely determined metallicity. Using the metallicities of these primaries, they compared the dispersions of the metallicity calibrations from Bonfils et al. (2005), Johnson and Apps (2009), and Schlaufman & Laughlin (2010). They found the scale of Schlaufman & Laughlin (2010), which is intermediate between Bonfils et al. (2005) and Johnson and Apps (2009), has the lowest dispersion and slightly modified that by readjusting its coefficients from their own sample as follows:

$$[\mathrm{Fe/H}] = 0.57\,\Delta(V\text{-}K) - 0.17 \qquad (\mathrm{RMSE} = 0.17\ \mathrm{dex}) \tag{3.12}$$

where $\Delta(V\text{-}K) = (V\text{-}K)_{observed} - (V\text{-}K)_{MS}$. In this case, $(V\text{-}K)_{MS}$ as a function of $(\mathrm{M}_K)_{MS}$ can be obtained by

$$(V\text{-}K)_{MS} = \sum_{i=0}^{5} b_i (\mathrm{M}_K)_{MS}^{i} \tag{3.13}$$

where $\{b_i\} = \{51.1413, -39.3756, 12.2862, -1.8392, 0.1343, -0.0038\}$.

We should mention that to apply this relation, the accurate absolute magnitude of the star of interest is required, making it difficult to determine the metallicities of dwarf stars whose distances are not available. This limitation can be removed if the metallicities of stars are found using a colour-colour diagram (instead of an absolute magnitude-colour diagram) which can provide a more productive approach to estimate stellar metallicities.

3.3.2 *Colour-Colour Diagrams*

There have been some studies in which optical and NIR colour-colour diagrams have been used to probe the Galaxy. For example, Gizis (1997) showed the *V-I* vs. *B-V* diagram for their

classified objects. The well-known tendency for metal-poor M subdwarfs to have redder *B-V* at a given *V-I* (which had already been discovered by Mould and McElroy 1978 and Dahn et al. 1995) was clearly evident for *V-I* > 1.7. This offset appeared to be strongly related to metallicity, as the esdM were approximately 0.3 magnitudes redder than the disk stars in *B-V*, with the sdM being found between the two sequences. As a result, they suggested that a *V-I* vs. *B-V* diagram could therefore be useful in identifying disk dwarfs, red subdwarfs and extreme subdwarfs.

Several metallicity-colour-colour calibrations have been undertaken in the last few years. SDSS studies have shown the *g-r* colour of M dwarfs appears to correlate with metallicity (West et al. 2004; Lépine & Scholz 2008; West et al. 2011)[58]. West et al. (2011) used their large spectroscopic sample of M dwarfs to find the correlation between photometric properties and the spectroscopically derived parameter ζ. While they showed there was a decreasing trend of ζ with *g-r*, the change in *g-r* was not the same for various spectral types[59]. As a result, the *g-r* colour alone was not adequate as a metallicity indicator, and they used two colours, *g-r* and *r-z* for their study. By examining the ζ values as a function of these two colours, they found a strong trend of decreasing ζ in the *g-r* and *r-z* space along diagonal lines and perpendicular to the stellar locus[60] (Covey et al. 2007). Figure 3.2 shows a region of *g-r* vs. *r-z* diagram of M dwarfs in the spectroscopic sample of West et al. (2011) (SDSS DR7). The bins have been colour coded based on the ζ values. By using a minimization technique[61], West et al. (2011) obtained a two-dimensional fit that related ζ to the *g-r* and *r-z* colours:

$$\zeta = 1.04 - 0.98(g - r)^2 - 0.07(r - z)^2 + 1.07(g - r) - 0.53(r - z) + 0.63(g-r)(r-z) \qquad (3.14)$$

with typical uncertainties of 10% - 20%. They suggested this relation could be helpful in identifying low metallicity subdwarfs in upcoming large photometric surveys.

However, Bochanski et al. (2013) pointed out that the relation (3.19) is only limited to (near) solar metallicity M dwarfs. In order to quantify the shift in *g-r* due metallicity effects, they

[58] We will also show this correlation by using the most recent atmosphere models as well as by our calibration sample (see Chapter4).

[59] In general, a colour (like *g-r*) not only depends on the metallicity but also the temperature and surface gravity of the star of interest.

[60] In a colour-colour space, ordinary stars (main sequence stars) fall onto a locus, which in this case runs from lower-left to upper-right.

[61] Levenberg-Marquardt technique: http://en.wikipedia.org/wiki/Levenberg%E2%80%93Marquardt_algorithm

introduced a quantity, $\delta_{(g-r)}$, measuring the difference in g-r between a subdwarf and its solar metallicity counterpart as a function of *r-z* colour, defined by

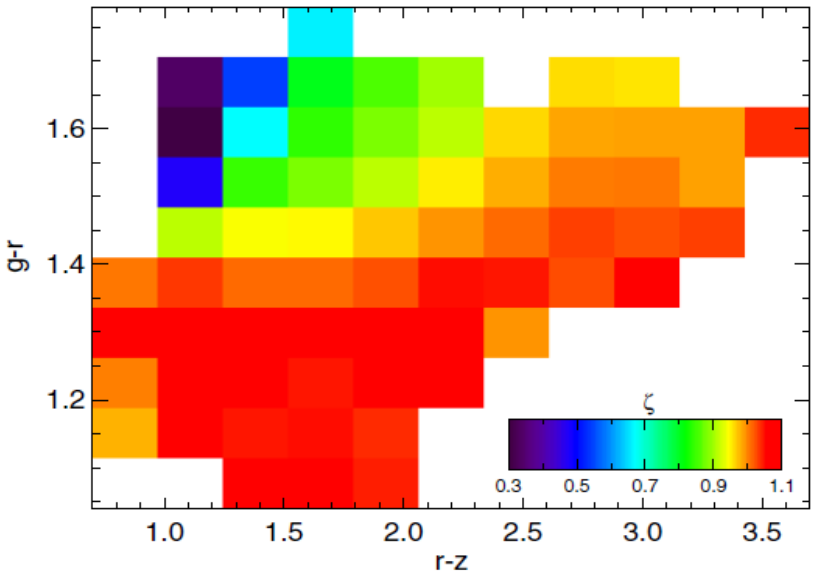

Figure 3.2 *g-r* vs. *r-z* diagram of M dwarfs in the SDSS DR7 spectroscopic sample from West et al. (2011). The bins are colour coded according to their ζ values. It demonstrates metallicity decreases roughly along diagonal lines and perpendicular to the stellar locus.

$$\delta_{(g-r)} = (g-r)_{subdwarf} - (g-r)_{dM} \tag{3.15}$$

where $(g-r)_{dM}$ is

$$(g-r)_{dM} = \sum_{n=0}^{6} C_n (r-z)^n \tag{3.16}$$

with coefficients $C_0 ... C_6$ (see Table 3 in Bochanski et al., 2013) and $(g-r)_{subdwarf}$ is the g-r colour of the subdwarf. The polynomial fit described by relation (3.21) was derived by fitting the locus of the main sequence M dwarfs (from SDSS DR9) on the g-r vs. *r-z* colour-colour diagram. Low-mass subdwarfs generally have redder g-r colours at the same value of *r-z* colour. The $\delta_{(g-r)}$ metric can, therefore, be considered as a crude measure of metallicity. Figure 3.3 represents the plot of ζ vs. $\delta_{(g-r)}$ for a sample of subdwarfs. It can be seen that $\delta_{(g-r)}$ roughly

traces ζ; smaller values of ζ (more metal poor) correspond to larger values of $\delta_{(g-r)}$ (redder values of g-r colour).

In another study, Johnson et al. 2012 investigated the locations of low mass dwarfs in the *J*-*K* vs. *V*-*K* diagram and found a dramatic change in the sequence (stellar locus) beyond V-*K* ≈ 4, corresponding to the onset of strong molecular bandheads characteristic of the M spectral type. Figure 3.4 demonstrates such a colour-colour diagram for a sample of low mass stars in the solar neighborhood. Four M dwarfs (shown by orange circles) are known to be metal-rich[62] ([Fe/H] > 0.25), and reside above the main sequence. In contrast, six known metal-poor ([Fe/H] < - 0.25) M dwarfs (shown by green circles), lie under the main sequence.

This suggests that the increased scatter in *J*-*K* colour is due to the effects of metallicity. Johnson et al. (2012) explained that the colour-metallicity effect can most likely be due to changes in continuous opacities from species such as H_2^-, H^-, He^-, H_2^+, and C^- (Allard & Hauschildt 1995). The *J*-band spectra of M dwarfs show deep potassium (K) and iron hydride (FeH) absorption features as well as dozens of shallower metal lines such as Na, Mg, Fe, and Si. On the other hand, the *K*-band is rather featureless (as compared to the *J*-band), having a few relatively shallow Na and Ca lines as the only prominent absorption features[63]. Hence stars with higher metallicities have preferentially suppressed *J*-band flux, causing the *J*-*K* colour of the stars to get redder.

To calibrate the colour-metallicity relation, Johnson et al. 2012 first fitted a two-part function to the locations of the main sequence stars in the colour-colour diagram (Figure 3.4). This locus can be approximated by a constant for $3.8 \leq V\text{-}K < 5.5$ and a polynomial of second degree for $V\text{-}K \geq 5.5$:

[62] Based on the [Fe/H] values of their FGK dwarf companions

[63] However, RA10 and RA12 used these lines as their main metallicity indicator.

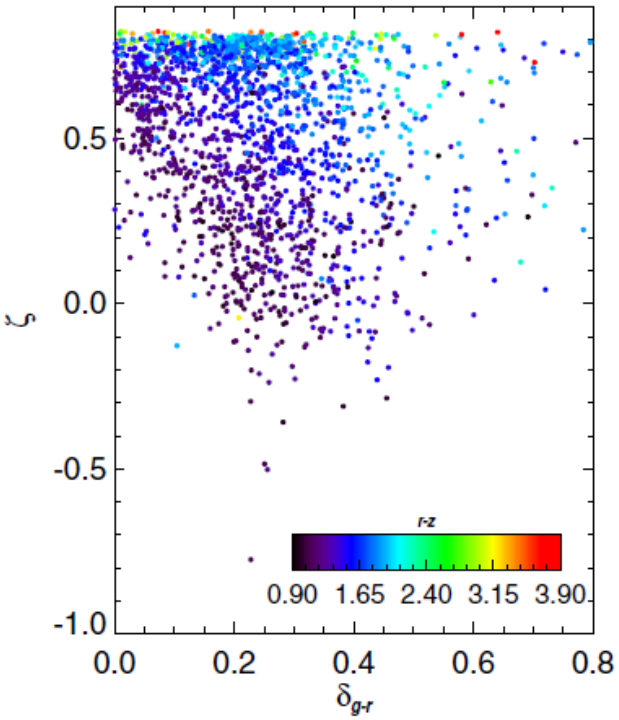

Figure 3.3 ζ vs. $\delta_{(g-r)}$ for a sample of subdwarfs. Smaller values of ζ correspond to larger values of $\delta_{(g-r)}$. Each point is colour-coded by the *r-z* colour of the star.

$$(J\text{-}K)_{\mathrm{MS}} = \begin{cases} 0.835 & \text{for} \quad 3.8 \leq V\text{-}K < 5.5 \\ \sum_{i=0}^{2} a_i (V\text{-}K)_{MS}^{i} & \text{for} \quad V\text{-}K \geq 5.5 \end{cases} \tag{3.17}$$

where $(J\text{-}K)_{\mathrm{MS}}$ and $(V\text{-}K)_{MS}$ are *J-K* and *V-K* colours of the main sequence stars respectively, and $\{a_i\}$ = {1.637, -0.2910, 0.02557}. They assumed the main sequence in this colour-colour plane to be an isometallicity contour with a value equal to the mean [Fe/H] of the solar neighborhood, ≈ - 0.05 (Johnson & Apps 2009).

By selecting 30 M dwarfs with widely separated FGK-type companions of known metallicity as their calibration sample, Johnson et al. 2012 plotted [Fe/H] against Δ (*J-K*) = $(J\text{-}K)_{observed}$ - $(J\text{-}K)_{MS}$ which indicates the distance of the location of a star from the main sequence along *J-K*

colour . Then they fitted a linear relationship, holding [Fe/H] = -0.05 at Δ (*J-K*) = 0, of the form (Figure 3.5):

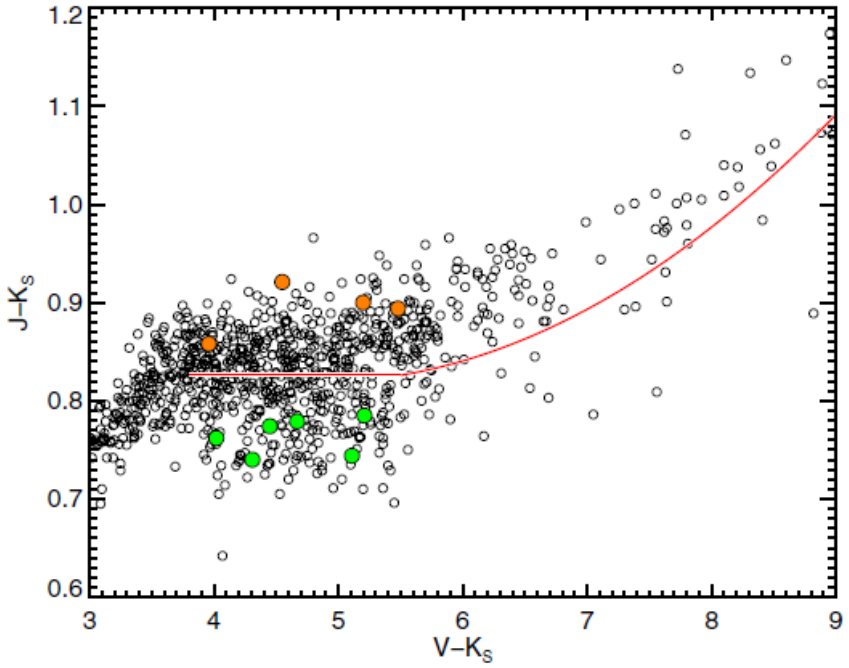

Figure 3.4 *J-K* vs. *V-K* diagram for a sample of low mass stars in Johnson et al. (2012). The known metal- rich stars are shown by the orange circles and the known metal-poor dwarfs are presented by the green circles. The main sequence stars are fitted by a constant for *V-K* < 5.5, and a polynomial of second order for *V-K* ≥ 5.5 (the red line).

$$[\mathrm{Fe/H}] = -0.05 + 3.52\ \Delta(J\text{-}K) \qquad (\mathrm{RMSE} = 0.15\ \mathrm{dex}) \qquad (3.18)$$

which is valid for -0.1 < Δ (*J-K*) < 0.1, roughly corresponding to -0.5 < [Fe/H] < 0.5.

Mann et al. (2013a) attempted to improve on this calibration and derived the relations below:

$$[\mathrm{Fe/H}] = -0.11 + 3.14\ \Delta(J\text{-}K) \qquad (\mathrm{RMSE} = 0.19\ \mathrm{dex}) \qquad (3.19)$$

$$[\mathrm{M/H}] = -0.09 + 2.14\ \Delta(J\text{-}K) \qquad (\mathrm{RMSE} = 0.16\ \mathrm{dex}) \qquad (3.20)$$

in which no restriction was made to keep [Fe/H] = -0.05 at Δ (*J-K*) = 0 .

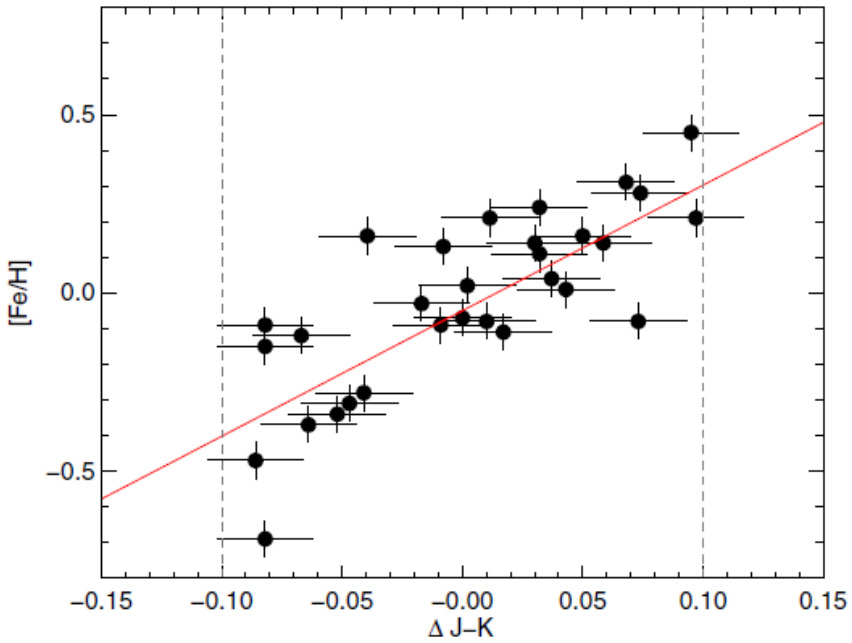

Figure 3.5 The metallicity plotted against Δ(*J-K*) from the calibration sample of Johnson et al. (2012). The red solid line represents the best fit given by Equation (3.18). The dashed lines denote the Δ(*J-K*) limits.

There is another approach in which synthetic colours are used. The main idea of this method is that the location of an M dwarf in a colour-colour diagram theoretically depends on its metallicity, temperature, and surface gravity. However, the surface gravity of M dwarfs can be taken approximately constant, log (g) ≈ 5.0, as a fixed parameter in such studies. If a synthetic diagram is constructed from a grid of atmosphere models, the location of any star on the diagram can be specified. The temperature and metallicity of the star can be determined by interpolation through the grid of models. Krawchuk et al. (2000) used the synthetic spectra from NextGen to calculate synthetic colours, and then constructed the synthetic *I-J* vs. *J-H* diagram which they found to have better diagnostic utility than the other colour-colour diagrams. They then determined the temperature and metallicity of a dozen late-type dwarfs via this diagram and compared the results with other available indications of the two parameters for those dwarfs. Krawchuk et al. (2000) found some systematic discrepancies between their values and those obtained by other means, which could be attributed to photometric errors and systematic flaws in the underlying model atmospheres. We will explore this method and extend it to some other sets of broad-band filters with the most recent model atmospheres (see Chapter 4).

Newton et al. (2014) employed their sample of 447 M dwarfs with metallicities calculated by their own spectroscopic calibration to develop a photometric technique for determining M-dwarf

metallicity. By testing all possible *JHK* colour combinations they found that the *J-K* colour of an M dwarf is the best single-colour diagnostic of its metallicity, consistent with Johnson et al. (2012). They also plotted the Bessell & Brett (1988) M-dwarf main sequence tracks for all colour-colour diagrams which coincided with the loci of their solar metallicity stars. Similar to the method of Johnson et al. (2012), they used the vertical (*J-K*) distance from the *J-K*, *H-K* Bessell & Brett dwarf main sequence, D_{MS}, as the diagnostic for metallicity of an M dwarf. They derived a relation between metallicity and D_{MS} as follows:

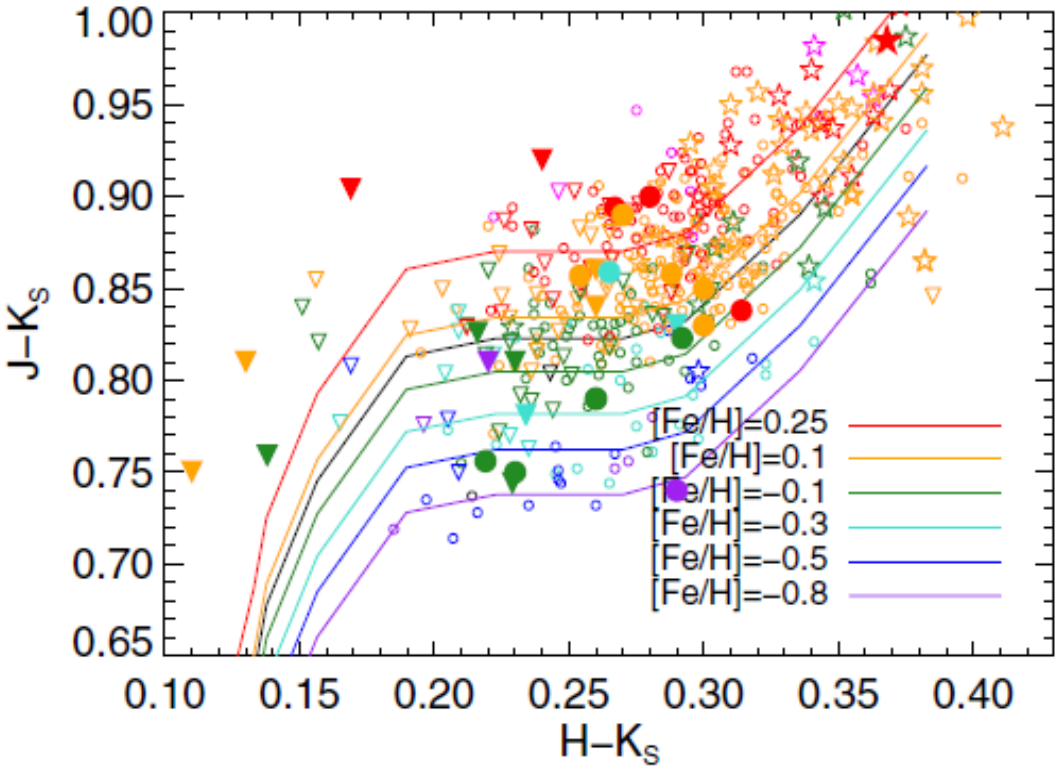

Figure 3.6 *J-K* vs. *H-K* diagram from Newton et al. (2014) for all M dwarfs observed with the NASA Infrared Telescope Facility (IRTF) star are colour-coded based on metallicity: stars with -1.0 < [Fe/H] < -0.6 are shown in purple, with -0.6 < [Fe/H] < -0.4 in blue, with -0.4 < [Fe/H] < -0.2 in cyan, with -0.2 < [Fe/H] < 0.0 in green, with 0.0 < [Fe/H] < +0.2 in orange, and with +0.2 < [Fe/H] < +0.3 in red. The symbols indicate spectral types: K7-M3 as triangles, M4-M5 as circles, and M6-M9 as stars. Large filled symbols are stars from the calibration sample in Newton et al. 2014. Overplotted are isometallicity contours for the best fit (Equation (3.26)) which relates distance from main sequence to metallicity.

$$[Fe/H] = 0.0299 + 6.47\,(D_{MS}) - 38.4\,(D_{MS})^{2} \qquad (3.21)$$

This calibration is valid for stars with metallicities of -0.7 < [Fe/H] < 0.3 dex and 0.2 < H-K < 0.35. Figure 3.6 shows the resulting photometric calibration from Equation (3.21).

Chapter 4

New Photometric Methods for Determining Metallicity and Temperature of M dwarfs

4.1 *Introduction*

Our main goal in this Chapter is to derive optical-NIR photometric calibrations for estimating the metallicity and temperature of M dwarfs which can readily be applied to large samples without the need for parallaxes, moderate-to-high resolution spectra or time-intensive, complicated calculations. This would allow us to statistically study metallicity distributions and to test the theoretical relations between metallicity and fundamental properties for large samples of M dwarfs.

We will first collect a metallicity calibration sample of 71 late-type K and early- to mid-type M dwarfs and derive two kinds of empirical photometric metallicity calibrations based on SDSS-2MASS photometry. We will then use the synthetic colours from the BT-Settl models to test if there are any synthetic colour-colour diagrams which can give reasonable values of metallicity for our calibrators. Although the models are not sufficient to photometrically determine metallicity, they can be used to estimate the approximate temperature of M dwarfs. Using the estimated effective temperature of the 71 stars either drawn from the literature or derived by a

recent temperature-spectral type relation as well as the SDSS-2MASS synthetic colours, an approximate photometric method for temperature determination is developed.

In section 4.2, the selection of the metallicity calibration sample is described in detail and the best fit for a polynomial relation between metallicity and colours is derived. The BT-Settl colour-colour diagrams are tested for metallicity sensitivity in Section 4.3. Finally, an approximate method for estimating the temperature of M dwarfs via a synthetic colour-colour diagram is offered in Section 4.4.

4.2 *Metallicity Calibration*

Since we apply the dust maps of Schlegel et al. (1998)[64] to correct our large SDSS-2MASS sample (see Chapter 5) for Galactic extinction, the metallicity calibrations to be used for this large sample must be based on calibrators with photometry corrected by the same way. For this reason, we corrected the photometry of all stars in our calibration sample through the maps above. These maps, one covering the northern Galactic hemisphere and one covering the southern hemisphere, are in pairs of 4096×4096 pixel Lambert projections[65].Using relevant equations, Galactic coordinates (*l*,*b*) are converted to pixel positions (x,y), usable for the maps.

In general, neighbouring SDSS images partially overlap one another, yielding multiple detections of some sources. Under some processes, one imaging run of an object is selected as PRIMARY detection and the others are assigned as SECONDARY detections[66]. To collect clean samples of point sources, it is highly recommended to select objects with PRIMARY status (unless users are specifically looking for time variability). In this study, we choose only PRIMARY objects by setting a variable called "mode" to 1 for collecting our calibration and large samples. As point sources are studied in this work, we adopted point-spread function (PSF)

[64] http://www.astro.princeton.edu/~schlegel/dust/data/data.html
[65] A conformal projection in which meridians are represented as straight lines converging toward the nearest pole and parallels as arc segments of concentric circles.
[66] https://www.sdss3.org/dr8/algorithms/resolve.php

magnitudes of SDSS objects. For isolated stars, which are well-described by the PSF, the optimal measure of the total flux is determined by fitting a SPF model to the object[67].

To derive our metallicity calibrations, we need some M dwarfs with reliable photometry and securely determined metallicities. Many nearby M dwarfs are members of binary systems, having an FGK- star primary with a spectroscopically determined metallicity. We identified 17 such M dwarfs (except two of them which are companions of an early-type M dwarf) with unsaturated SDSS *g*[68] and unsaturated 2MASS *JHK* magnitudes (while for most of them photometry in the *r*, *i* or *z* bands is saturated). We used the SDSS_phot Flag to check the saturation status of stars; the g magnitude is unsaturated if the saturation flag for this band is not set. To have unsaturated *JHK* photometry, we chose only those stars whose 2MASS read flags[69] are '222'[70].

In order to add more stars with reliable metallicities to our calibration sample, we refer to the work of Dahab & Strauss[71] (personal communication) who showed that by filtering the saturated objects in SDSS that have certain flags set, the photometry of remaining saturated objects are trustworthy. By careful comparisons, they demonstrated that the PSF magnitudes[72] are usable if none of the flags EDGE, INTERP_CENTER and PSF_FLUX_INTERP are set[73]. An object which is too close to the edge of an imaging frame is flagged EDGE in the SDSS photometry. Among PRIMARY objects, only large extended objects should be flagged EDGE. Therefore, for point sources, there is no need for concern about the PRIMARY objects having EDGE flag set. As a result, by filtering out the saturated objects in SDSS whose INTERP_CENTER and

[67] https://www.sdss3.org/dr10/algorithms/magnitudes.php#mag_psf
[68] The imaging data of SDSS *u, g, r, i* and *z* filters saturate at about 13, 14, 14, 14 and 12 magnitude, respectively.
[69] http://www.ipac.caltech.edu/2mass/releases/allsky/doc/sec2_2a.html
[70] The flag consists of a 3 character string, where the 1st character corresponds to the J band, the 2nd to the H band, and the 3rd to the K band.
[71] Unpublished undergraduate Honor's thesis of W.E. Dahab under supervision of M.A. Strauss, Princeton University.
[72] For isolated stars, which are well-described by the point spread function, the optimal measure of the total flux is determined by fitting a PSF model to the object, called PSF magnitude. This is the magnitude which we chose for our study.
[73] To understand the meaning of these flags, see :
https://www.sdss3.org/dr8/algorithms/flags_detail.php
http://classic.sdss.org/dr6/products/catalogs/flags_detail.html#status

PSF_FLUX_INTERP flags are set, we can have stars with rather reliable photometry. In this way, we found 4 M dwarfs in FGK-M binaries which have unsaturated photometry in *JHK* bands, but the *g* magnitudes of these stars are saturated while none of the two flags, INTERP_CENTER and PSF_FLUX_INTERP, of the *g* band are set. In these cases, the *g* magnitudes are even fainter than the saturation limit of the *g* band ($\sim$ 14 mag), and we thus call these "weakly saturated" magnitudes. According to Dahab & Strauss, we can be certain that the *g* magnitudes of these stars are usable for our study.

Now, there are 21 M dwarfs with trustworthy *gJHK* photometry and reliable metallicities, forming the building blocks of our metallicity calibration. The metallicity of 18 of these stars were accurately determined through their FGK-star primaries using spectroscopic analyses of high-resolution spectra. The metallicity of the other M dwarfs were obtained by spectroscopic analyses of moderate-resolution spectra of their FGK-dwarf or M-dwarf primaries. Note that only two M dwarfs in the calibration sample are in M+M binaries with an M-dwarf primary of early type (M1) whose metallicities were determined empirically using moderate-resolution spectra.

Table 4.1 The equatorial coordinates, extinction-corrected photometry and g-band saturation status of 21 M dwarfs in FGK+M or M+M binaries

Name	RA	DEC	*g*	*J*	*H*	*K*	saturation
NLTT 2478	11.30661	0.26416	15.282	10.1040	9.5548	9.2600	un.sat
NLTT 57675	355.43814	-5.97075	15.260	10.3790	9.8009	9.5778	un.sat
GJ 3628 B	162.65939	51.75045	14.892	9.8186	9.241	9.0112	un.sat
LSPM J1248+1204	192.22272	12.07574	16.775	11.3770	10.856	10.5610	un.sat
LHS 3084	233.66708	2.20412	14.125	10.4950	9.9657	9.7681	un.sat
NLTT 40692	233.85694	60.08548	14.203	9.2443	8.6836	8.4015	un.sat
LSPM J0849+0329W	132.25940	3.49640	15.850	10.7210	10.154	9.8968	un.sat
Gl173.1B	69.93025	9.86299	14.772	10.1950	9.6719	9.3935	un.sat
2M 1743+2136	265.81415	21.60285	17.686	11.4680	10.989	10.6820	weak.sat
LSPM J1425+2035W	216.35788	20.59602	17.809	12.4410	11.992	11.7070	weak.sat
LSPM J1000+3155	150.20961	31.92943	17.246	10.2350	9.6268	9.2648	weak.sat
NLTT 28180	175.08684	9.51259	14.192	10.1010	9.5348	9.3032	un.sat
NLTT 42396	243.72070	60.64107	14.564	9.7904	9.2774	9.0118	un.sat
LSPMJ1210+1858E	182.54123	18.96898	21.140	13.6690	13.038	12.6820	un.sat
LSPM J1604+3909W	241.21222	39.15999	14.900	9.8504	9.4194	9.1376	un.sat
LSPM J1237+3549	189.31447	35.82158	15.453	11.3390	10.748	10.5130	un.sat
NLTT 36190	211.23263	1.956407	14.268	10.1140	9.4735	9.2630	un.sat

NLTT 39578	227.96436	39.55067	14.317	9.8510	9.262	9.0601	un.sat
I10005+2717	150.14884	27.28486	20.194	12.9700	12.384	12.0160	un.sat
NLTT 21671	141.09943	6.378282	15.423	10.5820	10.026	9.7105	un.sat
NLTT 8870	41.421633	44.95085	16.813	11.0120	10.490	10.1540	weak.sat

Notes: "un.sat" denotes unsaturated and "weak.sat" represents weakly saturated status.

The name, right ascension, declination, extinction-corrected magnitudes and saturation status in the *g* band of these 21 stars are listed in Table 4.1. The Galactic coordinates and extinction coefficients in the *gJHK* bands are represented in Table 4.2. As expected (see Chapter 5), the stars with higher absolute values of Galactic latitude (|*b*|) have smaller extinction coefficients. The spectral types, metallicities of primaries and relevant sources are given in Table 4.3.

Table 4.2 The Galactic coordinates and extinction coefficients in *gJHK* bands of 21 M dwarfs in FGK+M or M+M binaries

Name	Gal_ lat	Gal_long	A_g	A_J	A_H	A_K
NLTT 2478	-62.32099697	120.96879370	0.041	0.0100	0.0062	0.004
NLTT 57675	-63.26919731	83.24307613	0.054	0.0130	0.0081	0.005
GJ 3628 B	57.07205071	157.22111840	0.039	0.0094	0.0060	0.004
LSPM J1248+1204	74.67571966	123.10095760	0.096	0.0230	0.0150	0.009
LHS 3084	43.07786208	58.17481680	0.154	0.0370	0.0233	0.015
NLTT 40692	46.88196304	94.02098745	0.108	0.0257	0.0164	0.011
LSPM J0849+0329W	28.11696262	201.51639670	0.147	0.0350	0.0220	0.014
Gl173.1B	-22.88112653	187.64824270	0.284	0.0680	0.0431	0.027
2M 1743+2136	23.76506187	45.99535623	0.181	0.0430	0.0270	0.018
LSPM J1425+2035W	66.99484741	44.94667380	0.089	0.0210	0.0140	0.009
LSPM J1000+3155	53.41598426	195.47430320	0.106	0.0260	0.0162	0.010
NLTT 28180	65.87692911	168.40646610	0.060	0.0140	0.0092	0.006
NLTT 42396	42.23979559	91.79770892	0.116	0.0276	0.0176	0.011
LSPM J1210+1858E	77.73298421	171.64390930	0.094	0.0220	0.0140	0.010
LSPM J1604+3909W	47.95197350	62.16262977	0.222	0.0526	0.0336	0.021
LSPM J1237+3549	81.21657802	138.77968270	0.058	0.0140	0.0090	0.006
NLTT 36190	58.73267337	84.21916915	0.062	0.0150	0.0095	0.006
NLTT 39578	58.08758290	64.62866436	0.092	0.0220	0.0140	0.009
I10005+2717	52.78740420	203.14338730	0.218	0.0520	0.0340	0.022
NLTT 21671	37.19881847	199.32928760	0.088	0.0210	0.0130	0.008
NLTT 8870	-12.91431900	143.72670490	0.656	0.1560	0.1000	0.063

Table 4.3 The spectral types of secondaries, metallicities of primaries and corresponding references of 21 M dwarfs in FGK+M or M+M binaries

Name	Spec.Type	Spec.Type Ref	[Fe/H] Prim	±[Fe/H]	[Fe/H] Ref
NLTT 2478	M3.8	M13a	0.02	0.03	VF05
NLTT 57675	M3.6	M13a	-0.03	0.03	VF05
GJ 3628 B	M4.1	M13a	-0.04	0.10	SOP
LSPM J1248+1204	M5	N14	0.08	0.03	VF05
LHS 3084	M0	WW05/R10-13	-0.73	0.05	WW05
NLTT 40692	M4.1	M13a	0.11	0.03	VF05
LSPM J0849+0329W	M4	N14	0.10	0.03	VF05
Gl173.1B	M3.2	M13a	-0.34	0.03	N12
2M 1743+2136	M4.5	M14	-0.39	0.05	F08
LSPM J1425+2035W	M5	M14	-0.57	0.05	Ram07
LSPM J1000+3155	M6	M13a	0.20	0.03	VF05
NLTT 28180	M1.6	M13a	-0.12	0.03	M13a-Calib.Sample
NLTT 42396	M3.5	M13a	-0.25	0.04	M13a-Calib.Sample
LSPM J1210+1858E	M6.5	M14	0.30	0.03	M13a-Calib.Sample
LSPM J1604+3909W	M5	N14	-0.69	0.03	VF05
LSPM J1237+3549	M1.8	M13a	-0.05	0.03	M13a-Calib.Sample
NLTT 36190	M1.8	M13a	-0.03	0.03	M13a-Calib.Sample
NLTT 39578	M2.8	M13a	-0.09	0.03	M13a-Calib.Sample
I10005+2717	M5.5	M14	0.26	0.10	M14-13a Empir.Calib
NLTT 21671	M4	M13a	0.21	0.07	Rob07
NLTT 8870	M5	M14	0.11	0.10	M14-13a Empir.Calib

Notes:

Source of Spectral types: M13a=Mann et al. (2013a), N14=Newton et al. (2014), WW05/R10-13= Temperature taken from Woolf & Wallerstein (2005) and spectral type estimated by the temperature-spectral relations of Rajpurohit (2010; 2013)

Source of [Fe/H]:

VF05=Valenti & Fischer (2005), using the software package SME (Spectroscopy Made Easy analysis; Valenti & Piskunov 1996) with an adopted uncertainty of 0.03 dex for [Fe/H] and [M/H]. High-resolution observed spectra were applied.

SOP=Bouchy & The Sophie Team (2006), Metallicity taken from spectra of the SOPHIE Spectrograph. High-resolution observed spectra were applied.

N12=Neves et al. (2012), based on the method of Santos et al. (2002;2004). High-resolution observed spectra were applied.

F08=Fuhrmann (2008). High-resolution observed spectra were applied.

Ram07=Ramírez et al. (2007). High-resolution observed spectra were applied.

M13a-Calib.Sample=Mann et al. (2013a) in their calibration sample, based on the software package SME as mentioned above and a set of tuned lines from the SPOCS catalog (Valenti & Fischer 2005).High- resolution observed spectra were applied.

M14-13a Empir.Calib=Mann et al. (2014), based on the empirically spectroscopic calibration. Moderate-resolution observed spectra were applied.

Rob07=Robinson et al. (2007).Moderate-resolution observed spectra were applied.

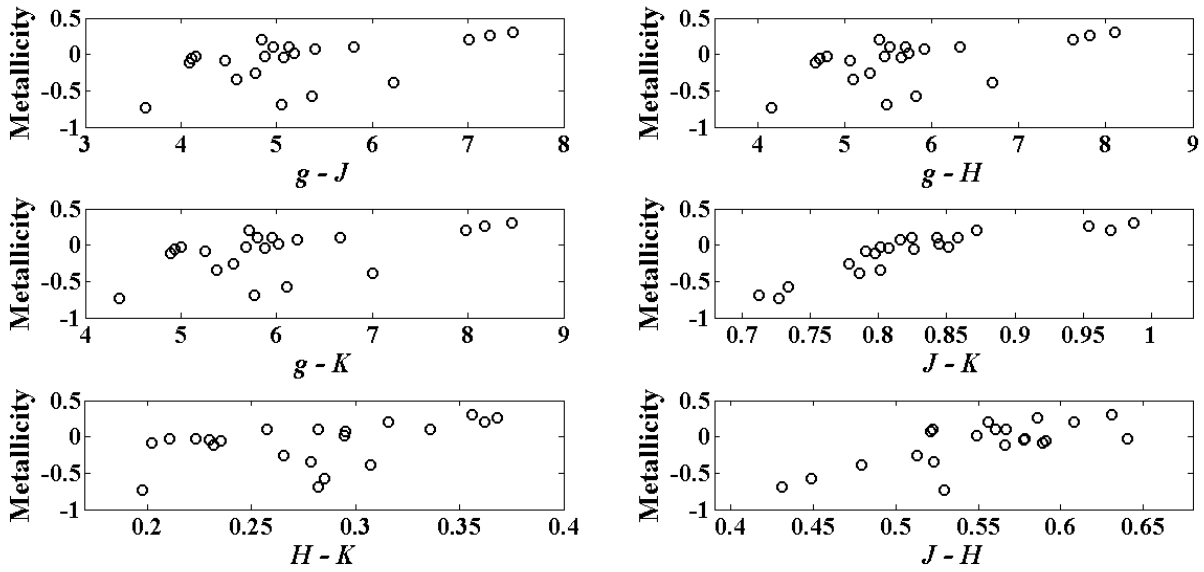

Figure 4.1 Metallicity versus six different colours of *g*, *J*, *H* and *K* magnitudes for M dwarfs in the calibration sample.

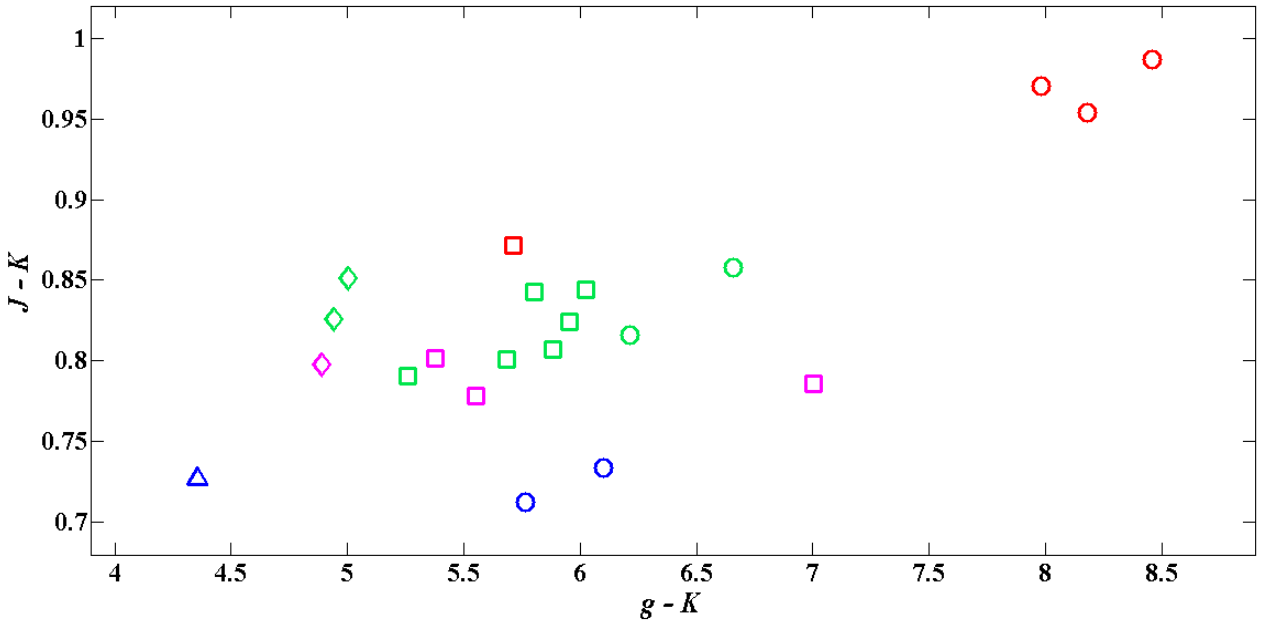

Figure 4.2 The (*g*-*K*)-(*J*-*K*) colour-colour diagram for the 21 M dwarfs in the calibration sample in common proper motion pairs with FGK- or M-dwarf primaries. The metallicity values are colour-coded: stars with [Fe/H] ≥ +0.15 dex are plotted in red, with -0.1 ≤ [Fe/H] < +0.15 dex in green, with -0.4 ≤ [Fe/H] < -0.1 dex in purple and with [Fe/H] <-0.4 dex in blue. The spectral types are symbol-coded: spectral types around M0 are shown by triangle, around M2 by diamond, between around M3 and M4 by square, and between around M5 or M6 by circle.

We investigated the relation between colours and metallicity by plotting metallicity versus all possible colours involving *g, J, H* and *K* magnitudes as shown in Figure 4.1. It can be seen that among all the colours, the *J-K* colour is the best metallicity indicator with the least scatter in the corresponding plot. This is in agreement with the previous studies of Johnson et al. (2012) and Newton et al. (2014). As Johnson et al. (2012) nicely suggested (See Section 3.3.1), due to the deep potassium (K) and iron hydride (FeH) absorption features as well as dozens of shallower metal lines in the *J*-band spectra of M dwarfs, stars with higher metallicity have preferentially suppressed *J*-band flux, as compared to *K*-band spectra where there are only a few relatively shallow Na and Ca lines as the prominent absorption features. This causes the *J-K* colour of the metal-rich M dwarfs to be redder.

We found that the (*g-K*)-(*J-K*) colour-colour diagram can well separate metal-poor from metal-rich M dwarfs. Figure 4.2 shows such a diagram for the 21 M dwarfs in our calibration sample. The metallicity values are coded by colours and the spectral types are coded by symbols. Overall, for a given spectral type, the metal-poor stars are bluer than metal-rich ones, and clearly the *J-K* colour is a better diagnostic for metallicity than *g-K*. It can also be seen that the *g-K* colour is a better indicator for spectral type than *J-K*, and for a given metallicity, the earlier-type M dwarfs are bluer than stars of later spectral types. However, these stars are not sufficient for fitting the (*g-K*)-(*J-K*) plane because there are some empty regions which must be filled in and more M-dwarf calibrators are needed. For this purpose, we will add some other early- to mid-type M dwarfs and late-type K dwarfs with spectroscopically determined metallicity through moderate-resolution spectra; their selection in the first step is by eye, based on their locations on the (*g-K*)-(*J-K*) diagram with respect to the 21 M dwarfs using the two rules above: 1) at a given spectral type, the metal-poor stars are bluer in *J-K* than the metal-rich ones 2) at a given metallicity (or a metallicity range), the earlier-type stars are bluer in *g-K* than the later-type ones. In this way, we collect 58 more stars, yielding a total 79 M or K dwarfs in our calibration sample. We should note that in addition to metallicity and spectral type (temperature), the location of an M dwarf on a colour-colour diagram relies on other stellar properties such as surface gravity (Figure 2.2). In this study, we assumed a constant log (g) ($\approx$ 5) for all M dwarfs, however, to calibrate metallicity more accurately, a careful investigation of surface gravity is required.

Now we can obtain the best fit of a low-order polynomial in general form between metallicity and *g-K* and *J-K* colours for the 79 stars as follows:

$$[\text{Fe/H}] = c_1 + c_2(g-K) + c_3(J-K) + c_4(g-K)^2 + c_5(J-K)^2 + c_6(g-K)(J-K) \quad (4.1)$$

This is of the same order (second order) as that from Johnson et al. (2012) which had an optical-NIR calibration with a filter set similar to ours. The only difference is that we employed the g magnitude instead of the *V* magnitude used in the calibration of Johnson et al. (2012). It should be remarked that for the purely NIR photometric calibration of Newton et al. (2014), the isometallicity curves (Figure 3.6 in Chapter 3) could be reproduced by a third-degree polynomial. Clearly, the shape of isometallicity contours in colour-colour diagrams depends on the filter magnitudes and the combinations of colours used in the corresponding calibrations.

We rejected 8 outliers for lying more than 2.5-sigma in three steps as follows. The RMSE of the entire sample of 79 stars is 0.127 dex, in which three stars have RMSEs larger than 2.5σ. By excluding these three stars, a sample of 76 dwarfs with an RMSE equal to 0.100 dex was obtained. In this sample, two stars having RMSEs larger than 2.5σ were rejected, leading to a sample of 74 stars with an RMSE = 0.091. Finally, by removing three stars whose RMSE were larger than 2.5σ, we achieved our final calibration sample of 71 dwarf stars, having an RMSE = 0.078 dex. The astrometry, photometry, and metallicity of these 8 outliers are given in Table 4.4.

The astrometry, photometry, spectral type and metallicity of our final calibrators are listed in Tables 4.5, 4.6 and 4.7, respectively. The (*g-K*)-(*J-K*) colour-colour diagram of the sample is demonstrated in Figure (4.3).

The coefficients of the best fit for the 71 stars in the calibration sample are:

$$\{c_i\} = \{-12.7170, -0.0381, 26.7638, -0.0699, -17.4375, 1.0570\} \quad (4.2)$$

with R^2_{ap}= 0.90, yielding elliptical isometallicity contours. It should be noted this metallicity calibration is applicable for stars of spectral types between K6 and M6.5 with -0.73 ≤ [Fe/H] ≤ +0.3 dex, 3.37 ≤ *g-K* ≤ 8.46 and 0.71 ≤ *J-K* ≤ 1.01. We tested our metallicity calibration by

comparing the values obtained by Equation (4.1) and those taken from other studies for our calibrators, as represented in Figure (4.4).

We will apply the metallicity calibration of Equation (4.1) to our large SDSS-2MASS sample and test the resulting metallicity distribution for each one (see Chapter 6).

Table 4.4 The equatorial coordinates, extinction-corrected photometry metallicity and metallicity references of the 8 outliers

Name	RA	DEC	*g*	*J*	*H*	*K*	[Fe/H]	[Fe/H] Ref
KIC 4551429	288.69063	39.66132	15.663	11.9650	11.3070	11.1620	0.18	M13b/Non-KOI
NLTT 57972	356.83604	42.63558	16.602	10.8540	10.2910	10.0830	-0.06	N14
NLTT 18833	120.59533	3.33879	14.223	9.5719	9.0278	8.8066	-0.07	N14
KIC 5080636	285.01310	40.22075	15.874	11.8980	11.2450	11.0350	0.25	M13b/KOI
NLTT 36732	213.88557	4.65868	15.100	9.4178	8.9263	8.6118	-0.41	N14
NLTT 21531	140.24143	3.36844	14.039	9.3298	8.7768	8.5065	-0.28	N14
KIC 2010738	290.53420	37.40245	16.979	13.8860	13.2080	13.0640	0.21	M13b/Non-KOI
GJ 3183	42.95721	29.48699	14.392	9.3997	8.8974	8.6378	0.06	N14

Notes:

Source of [Fe/H]:N14=Based on an empirical metallicity calibration of moderate-resolution, NIR spectra in Newton et al. (2014), M13b/KOI =The sample taken from Mann et al. (2013b) with metallicities based on a modified empirical calibration of moderate-resolution, optical spectra in Mann et al. (2013a, 2013b), M13b/Non-KOI = The sample taken from Mann et al. (2013b) with metallicities based on the weighted means of *J*-, *H*-, and *K*-band calibrations described in Mann et al. (2013a)

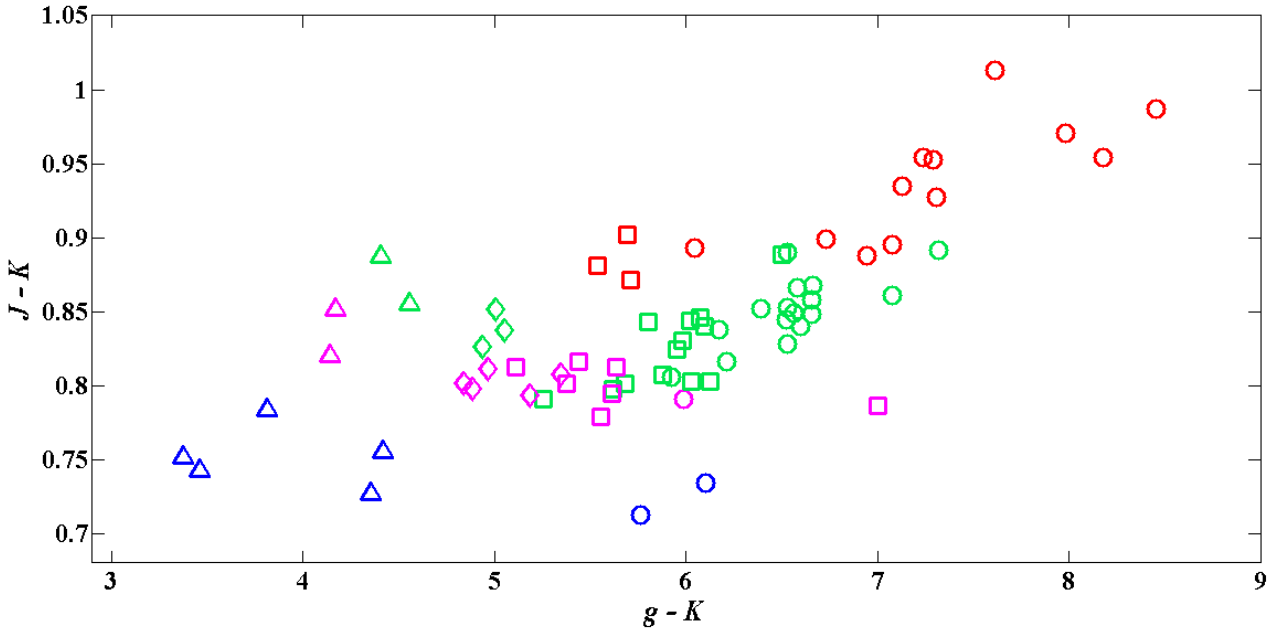

Figure 4.3 The (*g*-*K*)-(*J*-*K*) colour-colour diagram for the 71 dwarfs in the calibration sample. The metallicity values are colour-coded as described in Figure 4.2. The spectral types are symbol-coded: spectral types between around K6 and M0 are shown by triangle, between around M1 and M2 by diamond, between around M3 and M4 by square, and between around M5 or M6 by circle.

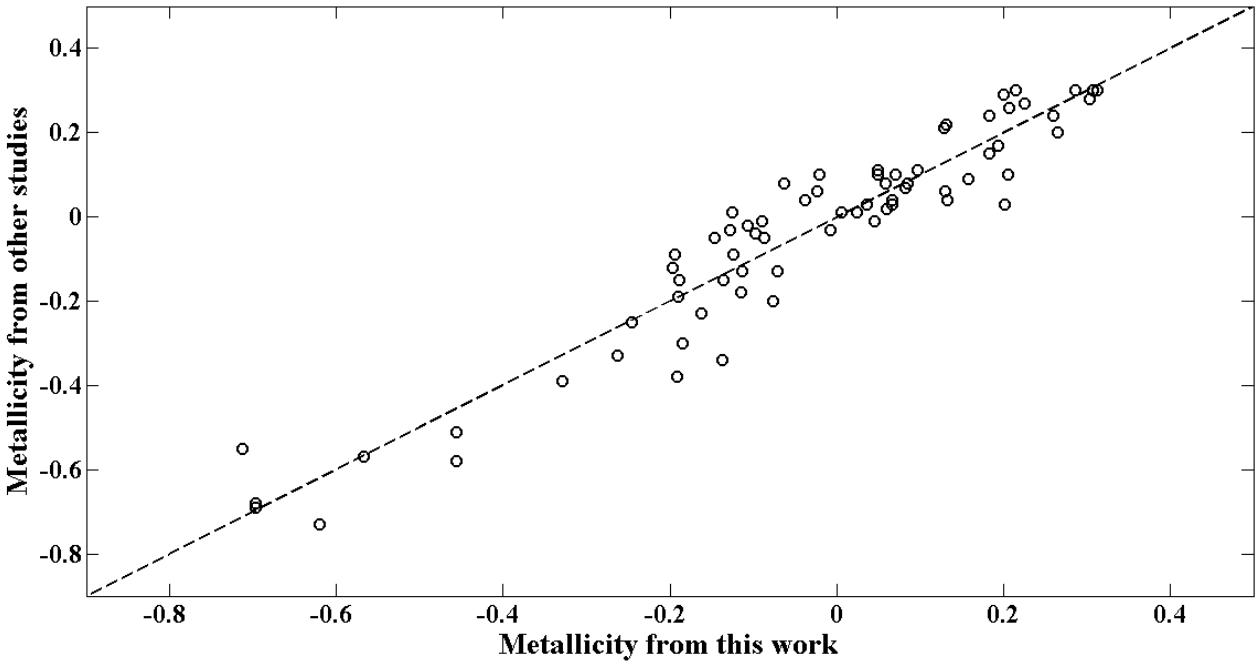

Figure 4.4 The metallicities derived by other studies versus metallicities calculated by Equation (4.1), see Table 4.3.

Table 4.5 The equatorial coordinates, extinction-corrected photometry and *g*-band saturation status of 50 M dwarfs in the calibration sample

Name	RA	DEC	*g*	*J*	*H*	*K*	saturation
LP 655-23	67.71681	-8.82204	15.055	9.8242	9.2656	8.9783	un.sat
LSPM J0959+4712	149.94150	47.20319	14.903	9.7498	9.1951	8.9195	un.sat
LSPM J1056+0319	164.24890	3.325909	16.143	10.8180	10.2570	10.015	un.sat
LSPM J1148+5305	177.19700	53.08603	15.376	10.1180	9.5478	9.2778	un.sat
LSPM J1309+2859	197.39560	28.98516	14.993	9.4554	8.8988	8.6036	un.sat
LSPM J1432+1600W	218.04490	16.01375	14.388	9.2686	8.7026	8.4631	un.sat
LSPM J0856+1239	134.08150	12.66391	15.221	9.5435	9.0065	8.6911	un.sat
LSPM J1005+1703	151.31840	17.05736	16.831	11.1160	10.5540	10.2500	un.sat
LSPM J1021+0804	155.32950	8.074137	16.452	10.7710	10.2210	9.9267	un.sat
LSPM J1110+4757	167.71460	47.95058	15.292	10.0680	9.5242	9.2654	un.sat
LSPM J1352+6649	208.21080	66.81847	16.587	10.5320	9.9496	9.6442	un.sat
LSPM J1345+2852	206.29600	28.86702	14.483	9.8621	9.2983	9.0459	un.sat
KIC 6183511	283.40190	41.51634	17.194	12.8030	12.2310	12.0100	un.sat
KIC 5252367	283.19390	40.49562	16.192	11.6540	11.0220	10.8470	un.sat
KIC 3426367	285.92890	38.52099	15.960	11.8040	11.1930	10.9930	un.sat
KIC 4243354	285.40000	39.31271	16.412	13.0920	12.4610	12.2720	un.sat
KIC 4139816	286.07910	39.27832	16.896	13.8630	13.2210	13.0800	weak.sat
J20515725-0111317*	312.98850	-1.1923	19.376	15.7120	15.0030	14.9570	un.sat
LSPM J0918+6037W	139.59590	60.62529	16.620	10.9830	10.3790	10.0930	un.sat
LSPM J0001+0659	0.31581	6.993214	17.492	11.2740	10.7330	10.4130	un.sat
LSPM J0237+0021	39.37381	0.357592	15.848	10.5130	9.9450	9.6750	un.sat
LSPM J0917+5825	139.44170	58.4229	16.050	10.2430	9.6863	9.3945	un.sat
LSPM J0958+0558	149.73540	5.966691	15.531	9.9210	9.3838	9.0325	un.sat
LSPM J1031+5705	157.87820	57.08833	15.472	9.7155	9.1756	8.8758	un.sat
LSPM J1112+0338	168.16100	3.645988	16.803	11.0870	10.5440	10.2380	un.sat
LSPM J1314+4846	198.62270	48.77799	13.919	9.6189	9.0392	8.8066	un.sat
LSPM J1419+0254	214.87330	2.910145	15.726	9.9301	9.3468	9.0623	un.sat
LSPM J1530+0926	232.62640	9.433736	15.968	9.5408	8.9880	8.6495	un.sat
LSPM J1531+4702	232.88470	47.03985	15.377	10.5540	10.0120	9.7564	un.sat
LSPM J2012+0112	303.24980	1.216242	16.062	10.3630	9.8092	9.5348	un.sat
LSPM J0024+2626	6.0156890	26.44166	15.322	10.1710	9.5593	9.2781	un.sat
LSPM J0738+1829	114.71170	18.48904	17.023	10.7400	10.1150	9.7861	un.sat
LSPM J1002+4827	150.70570	48.45927	16.293	9.9534	9.3268	9.0011	un.sat
LSPM J1038+4831	159.62420	48.52914	14.274	9.4847	8.8324	8.5828	un.sat
LSPM J1348+0429	207.03820	4.488044	16.566	10.733	10.1670	9.8339	un.sat
LSPM J1418+1812N	214.67120	18.20572	13.918	9.2584	8.6003	8.3774	un.sat

LSPM J1432+0811	218.03540	8.192037	16.465	10.0840	9.5140	9.1564	un.sat
LSPM J1631+4051	247.82830	40.86433	15.620	9.4271	8.8474	8.4922	un.sat
KIC 3935942	285.22380	39.03017	17.165	12.9510	12.2940	12.1140	un.sat
KIC 4543236	285.26700	39.63153	17.317	13.2790	12.7250	12.4780	un.sat
KIC 5513769	284.29610	40.71587	16.708	13.0030	12.3610	12.1480	un.sat
KIC 4725681	283.86640	39.89808	16.703	13.1820	12.5100	12.2950	un.sat
LSPM J0738+4925	114.69670	49.42423	16.754	10.5710	9.9569	9.6761	un.sat
J10173873+5651466*	154.41140	56.86296	19.146	15.8260	15.1150	14.9750	un.sat
LSPM J1239+0410	189.94470	4.179774	17.649	11.0470	10.4240	10.0340	un.sat
KIC 2850521	291.04750	38.09008	15.831	13.2070	12.5810	12.4560	weak.sat
LSPM J1101+0300	165.33190	3.004777	14.890	9.6910	9.2191	8.9001	un.sat
LSPM J1316+2752	199.13680	27.87494	14.071	9.2493	8.7167	8.4368	un.sat
LSPM J1709+3909	257.35840	39.16068	14.640	9.8190	9.2763	9.0247	un.sat
KIC 4543619	285.45780	39.63213	15.873	13.1530	12.5350	12.4110	un.sat

Note: The asterisk sign stands for 2MASS source designation and will hold throughout the thesis. "un.sat" denotes unsaturated and "weak.sat" represents weakly saturated status.

Table 4.6 The Galactic coordinates and extinction coefficients in *gJHK* bands of 50 M dwarfs in calibration sample

Name	Gal_lat	Gal_long	A_g	A_J	A_H	A_K
LP 655-23	-34.60480	204.50190	0.121	0.0288	0.0184	0.0117
LSPM J0959+4712	51.60538	170.42030	0.026	0.0062	0.0039	0.0025
LSPM J1056+0319	54.02414	175.92620	0.044	0.0100	0.0070	0.0040
LSPM J1148+5305	61.99240	142.40110	0.054	0.0130	0.0082	0.0052
LSPM J1309+2859	85.19635	53.46951	0.087	0.0206	0.0132	0.0084
LSPM J1432+1600W	63.54531	53.13410	0.082	0.0194	0.0124	0.0079
LSPM J0856+1239	33.90059	210.08720	0.174	0.0415	0.0265	0.0169
LSPM J1005+1703	50.91604	206.44590	0.058	0.0140	0.0090	0.0060
LSPM J1021+0804	50.11945	191.06000	0.076	0.0180	0.0120	0.0073
LSPM J1110+4757	61.96614	159.28250	0.058	0.0140	0.0088	0.0056
LSPM J1352+6649	49.38107	113.42910	0.029	0.0070	0.0044	0.0028
LSPM J1345+2852	77.53443	43.04549	0.084	0.0199	0.0127	0.0081
KIC 6183511	16.95805	71.49651	0.231	0.0550	0.0350	0.0220
KIC 5252367	16.72194	70.44610	0.160	0.0380	0.0240	0.0150
KIC 3426367	14.00718	69.41918	0.313	0.0740	0.0470	0.0300
KIC 4243354	14.70339	69.99524	0.292	0.0690	0.0440	0.0280
KIC 4139816	14.20858	70.18153	0.375	0.0890	0.0570	0.0360
J20515725-0111317*	-27.59760	47.15305	0.195	0.0460	0.0300	0.0190
LSPM J0918+6037W	41.69857	154.48480	0.080	0.0190	0.0120	0.0080

LSPM J0001+0659	-53.71990	102.70450	0.051	0.0120	0.0080	0.0050
LSPM J0237+0021	-51.93290	170.68080	0.145	0.0340	0.0220	0.0140
LSPM J0917+5825	42.30564	157.33580	0.077	0.0180	0.0117	0.0075
LSPM J0958+0558	44.32331	192.96540	0.067	0.0160	0.0102	0.0065
LSPM J1031+5705	51.67471	152.64740	0.095	0.0225	0.0144	0.0092
LSPM J1112+0338	56.94238	171.30800	0.048	0.0110	0.0070	0.0050
LSPM J1314+4846	68.06079	111.71030	0.097	0.0231	0.0148	0.0094
LSPM J1419+0254	57.33165	77.62421	0.100	0.0239	0.0152	0.0097
LSPM J1530+0926	47.95556	50.40473	0.119	0.0282	0.0180	0.0115
LSPM J1531+4702	52.74375	75.85253	0.048	0.0110	0.0070	0.0046
LSPM J2012+0112	-17.95810	44.13586	0.519	0.1230	0.0788	0.0502
LSPM J0024+2626	-35.82540	116.11230	0.216	0.0510	0.0327	0.0209
LSPM J0738+1829	19.12503	201.56170	0.226	0.0540	0.0340	0.0219
LSPM J1002+4827	51.73023	168.24190	0.041	0.0096	0.0062	0.0039
LSPM J1038+4831	57.13993	164.15070	0.043	0.0103	0.0066	0.0042
LSPM J1348+0429	63.09859	88.77775	0.053	0.0130	0.0080	0.0051
LSPM J1418+1812N	67.42797	52.27933	0.057	0.0136	0.0087	0.0056
LSPM J1432+0811	58.96278	66.37580	0.099	0.0240	0.0150	0.0096
LSPM J1631+4051	42.89327	64.62317	0.142	0.0339	0.0216	0.0138
KIC 3935942	14.71562	69.67103	0.221	0.0530	0.0340	0.0210
KIC 4543236	14.92471	70.25529	0.193	0.0460	0.0290	0.0190
KIC 5513769	16.03151	70.98980	0.263	0.0620	0.0400	0.0250
KIC 4725681	16.01987	70.07324	0.177	0.0420	0.0270	0.0170
LSPM J0738+4925	28.29479	169.16630	0.258	0.0610	0.0391	0.0249
J10173873+5651466*	50.23117	154.61510	0.080	0.0190	0.0120	0.0080
LSPM J1239+0410	66.67585	128.81540	0.078	0.0190	0.0120	0.0080
KIC 2850521	10.19673	70.78982	0.307	0.0730	0.0470	0.0300
LSPM J1101+0300	54.55372	174.21970	0.072	0.0170	0.0109	0.0069
LSPM J1316+2752	83.88131	39.04471	0.074	0.0177	0.0113	0.0072
LSPM J1709+3909	35.47597	63.26710	0.097	0.0230	0.0147	0.0093
KIC 4543619	14.79020	70.31644	0.275	0.0650	0.0420	0.0270

Table 4.7 The spectral type, metallicity and corresponding references of 50 M dwarfs in calibration sample

Name	Spec.Type	Spec.Type Ref	[Fe/H]	±[Fe/H]	[Fe/H] Ref
LP 655-23	M3	M14	0.03	0.10	M14
LSPM J0959+4712	M4	N14	0.01	0.12	N14
LSPM J1056+0319	M4	N14	0.01	0.13	N14
LSPM J1148+5305	M4	N14	-0.01	0.13	N14
LSPM J1309+2859	M5	N14	0.08	0.13	N14
LSPM J1432+1600W	M5	N14	-0.02	0.13	N14
LSPM J0856+1239	M6	N14	0.07	0.12	N14
LSPM J1005+1703	M6	N14	0.06	0.12	N14
LSPM J1021+0804	M5	N14	0.10	0.12	N14
LSPM J1110+4757	M4	N14	-0.09	0.13	N14
LSPM J1352+6649	M5	N14	0.15	0.12	N14
LSPM J1345+2852	M3.5	D13/R10-13	-0.13	0.12	D13
KIC 6183511	M1.5	P12/R10-13	-0.15	0.06	M13b/KOI
KIC 5252367	M2	P12/R10-13	-0.18	0.13	M13b/Non-KOI
KIC 3426367	M1.5	P12/R10-13	-0.15	0.13	M13b/Non-KOI
KIC 4243354	M0	P12/R10-13	-0.33	0.12	M13b/Non-KOI
KIC 4139816	K7.5	P12	-0.51	0.07	M13b/KOI
J20515725-0111317*	K7	SSPP/ST	-0.58	0.05	SSPP/M
LSPM J0918+6037W	M5	N14	0.10	0.12	N14
LSPM J0001+0659	M5	N14	0.10	0.12	N14
LSPM J0237+0021	M5	N14	0.03	0.12	N14
LSPM J0917+5825	M5	N14	0.08	0.12	N14
LSPM J0958+0558	M4	N14	0.03	0.12	N14
LSPM J1031+5705	M5	N14	0.01	0.13	N14
LSPM J1112+0338	M5	N14	0.04	0.13	N14
LSPM J1314+4846	M3	N14	-0.13	0.12	N14
LSPM J1419+0254	M5	N14	0.04	0.13	N14
LSPM J1530+0926	M6	N14	0.09	0.12	N14
LSPM J1531+4702	M4	N14	-0.05	0.13	N14
LSPM J2012+0112	M6	N14	0.06	0.12	N14
LSPM J0024+2626	M5	N14	0.29	0.12	N14
LSPM J0738+1829	M6	N14	0.30	0.12	N14
LSPM J1002+4827	M6	N14	0.28	0.12	N14
LSPM J1038+4831	M3	N14	0.24	0.12	N14
LSPM J1348+0429	M5	N14	0.27	0.12	N14
LSPM J1418+1812N	M3	N14	0.22	0.12	N14

LSPM J1432+0811	M6	N14	0.24	0.12	N14
LSPM J1631+4051	M6	N14	0.30	0.12	N14
KIC 3935942	M1	P12/R10-13	0.04	0.05	M13b/Non-KOI
KIC 4543236	M1	P12/R10-13	-0.19	0.06	M13b/Non-KOI
KIC 5513769	M0	P12/R10-13	-0.05	0.09	M13b/Non-KOI
KIC 4725681	M0	P12/R10-13	-0.01	0.07	M13b/KOI
LSPM J0738+4925	M6	N14	0.17	0.13	N14
J10173873+5651466*	K7	SSPP/ST	-0.38	0.03	SSPP/M
LSPM J1239+0410	M6	N14	0.30	0.12	N14
KIC 2850521	K6	P12	-0.68	0.11	M13b/Non-KOI
LSPM J1101+0300	M5	N14	-0.30	0.13	N14
LSPM J1316+2752	M4	N14	-0.20	0.14	N14
LSPM J1709+3909	M4	N14	-0.23	0.14	N14
KIC 4543619	K6.5	MQ14	-0.55	0.12	M13b/Non-KOI

Notes:
Source of Spectral types: M14=Mann et al. (2014), N14=Newton et al. (2014), D13/R10-13=Temperature taken from Deshpande et al. (2013) and spectral type determined by the temperature-spectral relations of Rajpurohit (2010; 2013), P12/R10-13=Temperatures taken from Pinsonneault et al. (2012) and spectral type determined by the temperature-spectral relation of Rajpurohit (2010; 2013), P12= Spectral type estimated by temperatures taken from Effective temperature scale for KIC stars (Pinsonneault et al. 2012), SSPP/ST= Spectral type estimated by temperature taken from the Sloan Extension for Galactic Understanding and Exploration (SEGUE) Stellar Parameter Pipeline (SSPP, Lee et al. 2008), and MQ14=Spectral type estimated by temperature taken from Rotation periods of Kepler main sequence stars (McQuillan 2014)

Source of [Fe/H]: N14=Based on an empirical metallicity calibration of moderate-resolution, NIR spectra in Newton et al. (2014), M13b/KOI =The sample taken from Mann et al. (2013b) with metallicities based on a modified empirical calibration of moderate-resolution, optical spectra in Mann et al. (2013a, 2013b), M13b/Non-KOI = The sample taken from Mann et al. (2013b) with metallicities based on the weighted means of *J*-, *H*-, and *K*-band calibrations described in Mann et al. (2013a), and SSPP/M= Based on multiple approaches of SSPP.

4.3 *Testing Synthetic Colours*

Theoretically, the location of an M dwarf on a colour-colour diagram correlates with its physical parameters such as metallicity, surface temperature and surface gravity. We positioned all M dwarfs in the calibration sample on all possible synthetic colour-colour diagrams from *gJK* magnitudes[74] (see Chapters 2), assuming log (g) = 5.0. Using biharmonic spline interpolation[75],

[74] We did not use *H* magnitude since a few stars in the calibration sample have saturated magnitude in this filter.
[75] The v4 method in the MATLAB's griddata is the biharmonic spline algorithm (Sandwell 1987) which is used for surface interpolation of irregularly distributed points. This algorithm is based on a linear combination of Green's

we determined the metallicity of these stars on each diagram and tabulated the results along with the corresponding RMSE in Table 4.8. For comparison, the measured metallicities drawn from the literature are also included in this table. Obviously, there are large discrepancies between the measured values and those determined by synthetic colour-colour diagrams.

We rejected the dwarfs with metallicities estimated by each synthetic diagram outside the metallicity range of the calibration sample, [-0.73,+0.3] dex. The number of remaining stars in the calibration sample corresponding to each diagram and resulting RMSEs are indicated in Table 4.9. Although these new samples have significantly smaller RMSEs ($\sim$ 0.3 dex) than that of the original calibration sample, more than half of the dwarfs were rejected, making the synthetic colour-colour diagrams insufficient for metallicity determination. This insufficiency could be related to the missing molecular opacities in the models. Although the BT-Settl synthetic spectra reproduce the slope of the spectral energy distribution and most of its features, some molecular opacities, especially the CaOH band at 5570 Å, TiO and VO opacities around 8200 Å, and AlH and NaH hydrides in the blue part of the spectra, are still missing (Rajpurohit et al. 2013).

As an approximation, we assumed all M dwarfs have a surface gravity of log (g) = 5.0, though it is not a very good approximation for all M dwarfs. As explained in Chapter 2, the early type M stars (M0-M1) have surface gravities which differ from log (g) =5.0 by around 0.2 dex. Our calculations show this discrepancy could lead to a mean difference in metallicity as large as 0.25 dex. As a result, this approximation could be a source of uncertainty for those metallicities determined through synthetic colours.

functions centered at each data point. The amplitudes of the Green's functions are found by solving a linear system of equations.

Table 4.8 The metallicity of stars in the calibration sample measured by other studies and estimated by interpolating through three synthetic colour-colour diagrams. The last row shows the corresponding RMSE of each diagram.

Name	Measured Metallicity	(*g*-*J*)-(*g*-*K*)	(*g*-*J*)-(*J*-*K*)	(*g*-*K*)-(*J*-*K*)
NLTT 2478	0.02	0.6813	0.7023	0.7125
NLTT 57675	-0.03	-0.5609	-0.2693	-0.5903
GJ 3628 B	-0.04	-0.4313	-0.353	-0.5706
LSPM J1248+1204	0.08	-0.1214	-0.0002	-0.1624
LHS 3084	-0.73	-1.2166	-1.5898	-2.3367
NLTT 40692	0.11	0.4533	0.5498	0.5118
LSPM J0849+0329W	0.10	0.3597	0.2704	0.1811
Gl173.1B	-0.34	-1.3677	-0.6689	-1.0147
2M 1743+2136	-0.39	1.0391	3.2400	3.0853
LSPM J1425+2035W	-0.57	-1.1027	-1.0294	-1.3506
LSPM J1000+3155	0.20	-9.4272	11.3665	12.1676
NLTT 28180	-0.12	-0.6091	-0.6082	-0.5954
NLTT 42396	-0.25	-0.6604	-1.1021	-0.7247
LSPM J1210+1858E	0.30	-20.1186	16.9439	16.8435
LSPM J1604+3909W	-0.69	-1.7398	-1.4280	-1.7278
LSPM J1237+3549	-0.05	-0.0965	-0.0195	-0.1501
NLTT 36190	-0.03	0.3206	0.4452	0.4452
NLTT 39578	-0.09	-0.2403	-0.7821	-0.4957
I10005+2717	0.26	-13.0766	14.1374	14.3598
NLTT 21671	0.21	0.5547	0.7047	0.9333
NLTT 8870	0.11	0.3255	0.2984	0.4119
LP 655-23	0.03	0.1496	0.4692	0.3270
LSPM J0959+4712	0.01	0.5984	0.5044	0.5397
LSPM J1056+0319	0.01	-0.4637	-0.463	-0.4876
LSPM J1148+5305	-0.01	-0.0392	0.2095	0.0973
LSPM J1309+2859	0.08	0.0134	0.5070	0.2358
LSPM J1432+1600W	-0.02	-0.0226	-0.0236	-0.3526
LSPM J0856+1239	0.07	-0.1549	-0.0794	-0.1361
LSPM J1005+1703	0.06	0.0197	-0.0007	0.0164
LSPM J1021+0804	0.10	-0.1931	-0.1476	-0.1883
LSPM J1110+4757	-0.09	-0.1927	-0.0221	0.0191
LSPM J1352+6649	0.15	0.4845	2.0511	2.4919
LSPM J1345+2852	-0.13	-0.4322	0.0306	-0.2159
KIC 6183511	-0.15	-1.0271	-0.6456	-0.8384
KIC 5252367	-0.18	-1.0178	-0.8326	-0.8349
KIC 3426367	-0.15	-0.5916	-0.3600	-0.3358

KIC 4243354	-0.33	-0.1642	0.2751	0.2468
KIC 4139816	-0.51	-3.2800	-3.0710	-2.1561
J20515725-0111317*	-0.58	-1.0299	-1.419	-1.3010
LSPM J0918+6037W	0.10	-0.0409	0.3253	0.1097
LSPM J0001+0659	0.10	0.3706	3.2849	3.6768
LSPM J0237+0021	0.03	-0.2003	-0.1687	-0.2138
LSPM J0917+5825	0.08	0.3277	0.2740	0.3534
LSPM J0958+0558	0.03	-0.0934	0.4187	0.1342
LSPM J1031+5705	0.01	0.0644	-0.0763	-0.0487
LSPM J1112+0338	0.04	-0.0571	-0.1253	-0.1185
LSPM J1314+4846	-0.13	-0.0312	0.0648	-0.3166
LSPM J1419+0254	0.04	0.3276	0.3325	0.4786
LSPM J1530+0926	0.09	-0.9399	5.2319	5.8738
LSPM J1531+4702	-0.05	-0.6541	-0.6353	-0.7688
LSPM J2012+0112	0.06	-0.2331	-0.2896	-0.2928
LSPM J0024+2626	0.29	1.1891	0.9692	1.0106
LSPM J0738+1829	0.30	-0.9496	3.8554	4.9000
LSPM J1002+4827	0.28	-1.2641	4.3329	5.4036
LSPM J1038+4831	0.24	0.7895	1.0094	1.2490
LSPM J1348+0429	0.27	0.4560	0.7378	1.0133
LSPM J1418+1812N	0.22	1.0125	1.2022	0.9644
LSPM J1432+0811	0.24	-1.1754	4.7301	5.6443
LSPM J1631+4051	0.30	-0.2925	3.1367	3.9859
KIC 3935942	0.04	-0.1422	-0.1491	-0.1252
KIC 4543236	-0.19	-0.9540	-0.9043	-0.5408
KIC 5513769	-0.05	0.7256	0.6809	0.7334
KIC 4725681	-0.01	-0.0370	1.8331	-0.1153
LSPM J0738+4925	0.17	0.1462	3.0207	3.6164
J10173873+5651466*	-0.38	0.5375	1.0613	1.2061
LSPM J1239+0410	0.30	-4.6024	6.6245	8.1756
KIC 2850521	-0.68	-9.4799	-8.4456	-6.6802
LSPM J1101+0300	-0.30	0.0138	-0.0492	-0.1802
LSPM J1316+2752	-0.20	-0.4796	-0.3999	-0.5575
LSPM J1709+3909	-0.23	-0.6893	-0.6977	-0.8026
KIC 4543619	-0.55	-7.8431	-7.1038	-5.6784
RMSE		3.5036	3.5207	3.6120

Table 4.9 The number of stars in the calibration sample with metallicities determined by synthetic colour-colour diagrams, which are within the metallicity range of the sample and the corresponding RMSEs

Colour-Colour Diagram	(*g*-*J*)-(*g*-*K*)	(*g*-*J*)-(*J*-*K*)	(*g*-*K*)-(*J*-*K*)
Number	34	30	31
RMSE (dex)	0.2945	0.2939	0.2982

4.4 *Temperature Calibration*

In order to estimate both the metallicity and temperatures of stars in our large sample simultaneously, we wished to construct a temperature calibration sample which covers the same spectral type and colour ranges as the metallicity calibration sample. For this reason, we used the metallicity calibration sample to calibrate the temperature of M dwarfs. More importantly, this sample provides us with a sufficient number of late-type K- and M- dwarfs having trustworthy *gJK* photometry.

The temperatures of the 71 calibrators are listed in Table 4.9. We compiled the temperatures of 25 stars from literature. For other stars without available data, we estimated temperatures from spectral types by applying the spectral type-temperature relations in Rajpurohit et al. (2010, 2013). However, these temperatures are not accurate enough for deriving an empirical temperature calibration. After careful searching, we could not find securely determined temperatures for our calibrators. Only those temperatures which were determined by relatively precise techniques, such as those which use luminosities and radii (for example, see the work of Dawson & De Robertis 2004 on Barnard's star), would be acceptable to empirically calibrate M-dwarf temperatures.

Rajpurohit et al. (2013) showed an agreement between theoretical and observed colours and demonstrated a rather good consistency for colour-temperature relations between various studies. Motivated by their work, we investigated all possible synthetic colour-colour diagrams from *gJK* magnitudes to estimate temperatures. The temperatures of stars in the calibration sample were obtained by the biharmonic spline interpolation for each diagram as given in Table 4.10. The corresponding RMSEs are also shown in this Table.

Table 4.10 The temperature of stars in the calibration sample measured and the corresponding references.

Name	Temp (K)	Temp Ref	Name	Temp (K)	Temp Ref
NLTT 2478	3120	R10-13	**KIC 4243354**	3913	P12
NLTT 57675	3200	K13	**KIC 4139816**	4097	P12
GJ 3628 B	3260	M08	**J20515725-0111317***	4153	SSPP/T
LSPM J1248+1204	2960	R10-13	**LSPM J0918+6037W**	2960	R10-13
LHS 3084	3780	WW05	**LSPM J0001+0659**	2960	R10-13
NLTT 40692	3068	R10-13	**LSPM J0237+0021**	2954	J09
LSPM J0849+0329W	3080	R10-13	**LSPM J0917+5825**	2885	J09
Gl173.1B	3380	M08	**LSPM J0958+0558**	3080	R10-13
2M 1743+2136	3020	R10-13	**LSPM J1031+5705**	3050	M08
LSPM J1425+2035W	2960	R10-13	**LSPM J1112+0338**	2960	R10-13
LSPM J1000+3155	2829	R12	**LSPM J1314+4846**	3270	R10-13
NLTT 28180	3540	R10-13	**LSPM J1419+0254**	2960	R10-13
NLTT 42396	3160	R10-13	**LSPM J1530+0926**	2800	R10-13
LSPM J1210+1858E	2700	R10-13	**LSPM J1531+4702**	3080	R10-13
LSPM J1604+3909W	3051	R12	**LSPM J2012+0112**	2800	R10-13
LSPM J1237+3549	3500	R10-13	**LSPM J0024+2626**	2960	R10-13
NLTT 36190	3500	R10-13	**LSPM J0738+1829**	2800	R10-13
NLTT 39578	3306	R10-13	**LSPM J1002+4827**	2800	R10-13
I10005+2717	2880	R10-13	**LSPM J1038+4831**	3270	R10-13
NLTT 21671	3080	R10-13	**LSPM J1348+0429**	2960	R10-13
NLTT 8870	2960	R10-13	**LSPM J1418+1812N**	3270	R10-13
LP 655-23	3200	K13	**LSPM J1432+0811**	2800	R10-13
LSPM J0959+4712	3080	R10-13	**LSPM J1631+4051**	3013	S13
LSPM J1056+0319	3080	R10-13	**KIC 3935942**	3695	P12
LSPM J1148+5305	3080	R10-13	**KIC 4543236**	3637	P12
LSPM J1309+2859	2960	R10-13	**KIC 5513769**	3813	P12
LSPM J1432+1600W	2960	R10-13	**KIC 4725681**	3905	P12
LSPM J0856+1239	2800	R10-13	**LSPM J0738+4925**	2800	R10-13
LSPM J1005+1703	2800	R10-13	**J10173873+5651466***	4131	SSPP/T
LSPM J1021+0804	2960	R10-13	**LSPM J1239+0410**	2800	R10-13
LSPM J1110+4757	3080	R10-13	**KIC 2850521**	4382	P12
LSPM J1352+6649	2960	R10-13	**LSPM J1101+0300**	2960	R10-13
LSPM J1345+2852	3200	D13	**LSPM J1316+2752**	3080	R10-13
KIC 6183511	3566	P12	**LSPM J1709+3909**	3080	R10-13
KIC 5252367	3499	P12	**KIC 4543619**	4258	MQ14
KIC 3426367	3546	P12			

Notes:

Source of Temperatures: R10-13=Temperatures determined using spectral types and temperature-spectral type relations of Rajpurohit et al. (2010, 2013), K13= Temperatures taken from RAVE 4th data release (Kordopatis et al. 2013), M08= Temperatures taken from Distance and atmospheric parameters of MSU stars (Morales et al. 2008), R12=Rojas-Ayala et al. (2012), D13= Deshpande et al. (2013), P12=As described in Table 4.6, SSPP/T=Temperatures taken from SSPP, J09= Jenkins et al. 2009, based on the technique of Casagrande et al. (2008), S13= Temperatures taken from UV/X-ray activity of M dwarfs within 10 pc (Stelzer et al. 2013), WW05= Woolf and Wallerstein (2005), and MQ14=As described in Table 4.6

Since there are a complete set of synthetic spectra with temperatures between [3000,4200] K (in steps of 100 K) and metallicities between [-2.5,+0.5] dex (in steps of 0.5 dex), we limited our studies to determine temperatures close to this temperature range. We rejected those stars in the calibration sample with temperatures outside the range [2954,4258] K, leading to a smaller sample of 57 stars as our temperature calibration sample. Table 4.11 represents the temperatures of these 57 stars estimated by three synthetic colour-colour diagrams. The last row shows the RMSE associated with each diagram.

Table 4.11 The temperatures of 57 dwarfs estimated by interpolating through three synthetic colour-colour diagrams and those determined by other means, all in terms of Kevin. The last row shows the corresponding RMSE of each diagram.

Name	Measur. Temp	(*g*-*J*)-(*g*-*K*) Temp	(*g*-*J*)-(*J*-*K*) Temp	(*g*-*K*)-(*J*-*K*) Temp
NLTT 2478	3120	3208.82	3209.44	3209.67
NLTT 57675	3200	3268.66	3278.86	3252.43
GJ 3628 B	3260	3158.36	3164.14	3149.44
LSPM J1248+1204	2960	3083.81	3090.63	3080.50
LHS 3084	3780	3852.50	3849.66	3699.86
NLTT 40692	3068	3267.92	3287.33	3285.33
LSPM J0849+0329W	3080	3197.85	3191.87	3186.11
Gl173.1B	3380	3298.28	3292.82	3296.69
2M 1743+2136	3020	743.12	1644.75	2012.24
LSPM J1425+2035W	2960	3061.87	3083.91	3065.54
NLTT 28180	3540	3514.75	3479.37	3496.40
NLTT 42396	3160	3270.93	3246.84	3288.39
LSPM J1604+3909W	3051	3107.64	3165.13	3145.87
LSPM J1237+3549	3500	3616.12	3555.55	3593.16
NLTT 36190	3500	3586.04	3598.77	3595.99
NLTT 39578	3306	3444.34	3363.39	3403.56
NLTT 21671	3080	3341.19	3339.53	3366.46
NLTT 8870	2960	3024.13	3017.13	3003.89

LP 655-23	3200	3168.77	3180.39	3168.83
LSPM J0959+4712	3080	3207.86	3202.63	3205.00
LSPM J1056+0319	3080	3092.30	3094.68	3092.50
LSPM J1148+5305	3080	3146.41	3154.54	3144.85
LSPM J1309+2859	2960	3053.74	3077.76	3065.58
LSPM J1432+1600W	2960	3177.61	3179.25	3155.91
LSPM J1021+0804	2960	2998.81	3001.72	3003.00
LSPM J1110+4757	3080	3162.09	3163.40	3168.30
LSPM J1352+6649	2960	1693.00	2440.44	2241.86
LSPM J1345+2852	3200	3315.96	3330.88	3308.91
KIC 6183511	3566	3410.97	3421.79	3417.9
KIC 5252367	3499	3316.79	3287.61	3340.49
KIC 3426367	3546	3545.09	3522.49	3543.11
KIC 4243354	3913	4096.29	4175.77	4144.35
KIC 4139816	4097	4197.70	4210.39	4197.61
J20515725-0111317*	4153	3812.36	3822.1	3779.47
LSPM J0918+6037W	2960	3002.29	3036.85	3017.45
LSPM J0001+0659	2960	241.89	1622.01	1555.2
LSPM J0237+0021	2954	3096.86	3098.52	3096.57
LSPM J0958+0558	3080	3011.34	3051.67	3028.35
LSPM J1031+5705	3050	3024.30	3008.77	3004.33
LSPM J1112+0338	2960	3003.92	2998.63	2999.52
LSPM J1314+4846	3270	3523.21	3515.17	3447.80
LSPM J1419+0254	2960	3018.72	3016.05	2998.40
LSPM J1531+4702	3080	3254.04	3256.79	3248.78
LSPM J0024+2626	2960	3240.95	3238.96	3237.97
LSPM J1038+4831	3270	3356.27	3384.62	3406.6
LSPM J1348+0429	2960	2919.67	2997.77	2904.25
LSPM J1418+1812N	3270	3431.03	3463.00	3430.46
LSPM J1631+4051	3013	0.85	1725.18	1173.82
KIC 3935942	3695	3470.07	3469.19	3470.48
KIC 4543236	3637	3474.37	3469.99	3521.82
KIC 5513769	3813	3920.73	3890.3	3936.47
KIC 4725681	3905	3696.51	4086.57	3753.09
J10173873+5651466*	4131	4222.39	4299.71	4252.13
LSPM J1101+0300	2960	3176.56	3172.27	3165.20
LSPM J1316+2752	3080	3264.98	3266.31	3255.93
LSPM J1709+3909	3080	3251.69	3254.28	3249.16
KIC 4543619	4258	3760.17	4221.00	4206.89
RMSE		656.28	343.59	372.90

Around 93% (53 out of 57) of stars in the temperature calibration sample have consistent temperature estimates in each synthetic diagram within the range mentioned above with rather reasonable RMSE. Among the three colour-colour diagrams, the (*g*-*K*)-(*J*-*K*) has the smallest RMSE ≅141 K. If the 7% outliers are excluded, the RMSEs decrease remarkably, as shown in Table 4.12. Among the three colour-colour diagrams, the (*g*-*K*)-(*J*-*K*) has the smallest RMSE ≅140 K.

Table 4.12 The number of stars in the calibration sample with temperatures determined by synthetic colour-colour diagrams, which are within the temperature range of the temperature calibration sample and the corresponding RMSEs

Colour-Colour Diagram	(*g*-*J*)-(*g*-*K*)	(*g*-*J*)-(*J*-*K*)	(*g*-*K*)-(*J*-*K*)
Number	53	53	53
RMSE (K)	156.61	145.30	140.00

We realized that for those stars whose temperatures determined using this diagram are outside the range of the temperature calibration sample, have a $g\text{-}K > 6.9$. It seems that the BT-Settl models are not sufficient for the estimate of M-dwarf temperatures in this range of *g*-*K* colour. We, therefore, use this colour-colour diagram to restrict the temperature of stars in our large SDSS-2MASS sample with $g\text{-}K < 6.9$ (see Chapter 6). Note that the synthetic colours for a given metallicity and temperature depend on surface gravity. We found that a difference of 0.2 dex in log (g) could change a temperature, on average, by 100 K. Accordingly, taking log (g) = 5.0 for M dwarfs is not always a good approximation in photometric analyses.

A more precise method for determining the effective temperature of M dwarfs would require calibrators with more reliable temperatures and photometry, especially in other filter bands, as well as more accurate stellar model atmospheres.

Summary

We established an empirical photometric calibration to determine the metallicity of dwarfs with spectral types from K6 to M6.5 in the metallicity range -0.73 to +0.3 dex. We also found a synthetic colour-colour diagram that best approximates the temperature of early-to-mid-type M dwarfs. Although these methods are not as accurate as spectroscopic techniques, they can be readily applied to large numbers of stars without any complication. This allows us to explore statistically the evolution of the Galaxy (see Chapters 6 and 7).

Chapter 5

Observations

5.1 *Introduction*

We have assembled an extinction-corrected photometric sample of low-mass stars with spectral types ranging from M0 to M6.5 drawn from the matched SDSS-2MASS catalog. In this Chapter, the selection of the sample is described in detail. To acquire an appropriate sample, we collect late-type K and M dwarfs with good photometric quality. Furthermore, several colour cuts for separating giants, using a photometric parallax, and applying our metallicity and temperature calibrations are also applied.

In Section 5.2, the method used for correcting the Galactic extinction effects is stated. The photometric surveys (the SDSS and 2MASS) in this study are described in Section 5.3. The flag filtering to get clean photometry and the colour cut to remove M giants from our sample are explained in Sections 5.4 and 5.5, respectively. In Section 5.6, the necessary colour cuts for using a photometric parallax to estimate the distance of our M dwarfs are presented.

5.2 *Extinction Correction*

To minimize extinction effects[76], we chose stars with high Galactic latitudes b > 50˚. Studies have shown that extinction is generally low at high latitudes, mainly due to the low column densities found along these lines of sights (Zagury 2000 & 2006, Larson and Whittet 2005).

We employed the dust maps of Schlegel et al. (1998) to correct the photometry of stars for Galactic extinction. Currently, these maps provide the most widely used dust data of the Milky Way on a large scale, including two two-dimensional full-sky maps (one for northern and one for southern Galactic hemisphere) with total line-of-sight dust column densities determined from far-infrared (100 and 240 μm) emission data. These maps have a resolution of 6.1 arcmin and are shown to predict reddening with an accuracy of 16%. We also used the relative extinctions given in Table 6 of Schlegel et al. (1998) to convert the extinction corrections in *V* magnitude to SDSS-2MASS filter bands.

Although the maps mentioned above give an efficient tool for dust study, these measure the total Galactic extinction along the line of sight and it may overestimate the true extinction to nearby stars (Covey et al. 2007; Jones et al. 2011). As a matter of fact, the objects inside the Galaxy lie in front of only a portion of the Milky Way's total dust and thus are likely attenuated and reddened by only a fraction of the total dust column. Using spectra of more than 56,000 M dwarfs from the SDSS, Jones et al. (2011) created a high-latitude, three-dimensional extinction map of the local Galaxy. In their technique, spectra from the stars in the SDSS DR7 dwarf sample along low-extinction lines of sight were compared to other SDSS M-dwarf spectra for deriving distances and accurate line-of-sight extinctions. However, the three-dimensional map is most appropriate for stars within around 500 pc from the Galactic plane ($H \lesssim 500$ pc) and since low-mass stars as high as 1600 pc from the plane are studied in this work, we prefer to apply the Schlegel's higher resolution map which are most useful for high vertical distances. As mentioned in Jones et al. (2011), it can safely be assumed that stars with Galactic heights larger than 500 pc are behind essentially the entire dust column.

[76] The absorption and scattering of electromagnetic radiation by dust and gas between an emitting source and the observer, for more details see: http://en.wikipedia.org/wiki/Extinction_(astronomy).

5.3 *Matched SDSS and 2MASS data*

The SDSS is one of the most influential surveys in modern astronomy. During its operations, it obtained multi-colour images of high quality, covering more than a quarter of the sky. Multi-band photometry was obtained using a 2.5-m wide-angle optical telescope at Apache Point Observatory, in New Mexico. The camera of the telescope was composed of thirty CCD chips each with 2048×2048 pixels (with a total of 120 Megapixels). These chips were organized in five columns of six chips per column. Each column had a different optical filter bandpass, designated *u*, *g*, *r*, *i*, and *z* (Fukugita et al. 1996), with average wavelengths of 355.1, 468.6, 616.5, 748.1 and 893.1 nm and with 95% photometric completeness of point sources in typical seeing to magnitudes of 22.0, 22.2, 22.2, 21.3, and 20.5, respectively (Gunn et al. 1998). The SDSS imaging covers several thousand square degrees of sky and over this region the SDSS photometric calibrations achieved an accuracy of ≈ 0.01-0.03 mag in *ugriz* (Ivezić et al. 2004, 2007; Adelman-McCarthy et al. 2006; Tucker et al. 2006; Padmanabhan et al. 2008).

When the conditions of the sky at Apache Point Observatory were not photometric, the SDSS switched to the spectroscopic operation with resolution of R∼ 1800. In this way, the spectra of a large number of galaxies and high-redshift quasars were measured, and hundreds of thousands of stellar spectra were obtained as well[77].

The SDSS Data Release 10 is the latest data set from the Sloan Digital Sky Survey, however, the SDSS imaging camera has been retired and no new photometric data have been included in DR10[78] with respect to the previous release, DR9[79]. We therefore compiled the data required for our study from the SkyServer DR9.

Our calibrations use both optical (the SDSS *g*) and NIR (the 2MASS *JHK*) broadband filters. In order to obtain a maximal photometric coverage for our large sample, we cross-matched the SDSS and 2MASS data. The 2MASS[80] was a survey of the whole sky in three IR broadband filters *J*, *H* and *K*, with average wavelengths of 1.25 μm, 1.65 μm and 2.17 μm, respectively. The

[77] For details see: http://www.sdss.org/
[78] http://www.sdss3.org/dr10/
[79] http://www.sdss3.org/dr9/
[80] http://www.ipac.caltech.edu/2mass/overview/about2mass.html

measurements were carried out from 1997 to 2001 using two highly-automated 1.3-m telescopes, one at Mt. Hopkins, Arizona for the Northern Hemisphere observations and one at Cerro Tololo Inter-American Observatory, Chile for the southern hemisphere data. Each telescope was equipped with a three-channel camera, each containing a 256×256 array of infrared detectors, capable of scanning the sky simultaneously at the three filters. Point sources brighter than about 1 mJy, with signal-to-noise ratio greater than 10 in each band were characterized and compiled in a separate catalog, the 2MASS Point Source Catalog (2MASS-PSC, Cutri et al. 2003). These bright sources ($\lesssim$ 13 mag) generally have 1-sigma photometric uncertainty[81] of < 0.03 mag (Skrutskie et al. 2006).

We used the SQL Search tool in the SkyServer DR9 to collect the dwarf star sample suitable for our study. The stars were taken from the SDSS DR9 photometric catalog (identified by PhotoObj, Ahn et al. 2012) with the object class specified by Type = 6 (for stars). Each object in the SDSS DR9 catalog has a unique SDSS identifier, called ObjID. These identifiers are also included in the 2MASS-PSC for objects in the regions overlapped with the SDSS, making it easy to find stars which are matched (having cross identifications) between the two surveys. We therefore selected those stars with the same ObjIDs in the two catalogs.

5.4 *Clean Photometry*

As described in Chapter 4, we adopted PSF magnitudes of SDSS sources for our study. By setting the SDSS variable 'mode'=1 (see Chapter 4) and flag CLEAN[82] = 1, we chose those stars whose SDSS photometry has passed appropriate standards of clean photometry. Moreover, by equating the 2MASS read flag to '222', blend flag to '111', and contamination/confusion flag to '000', we selected those stars which have unsaturated, unblended and uncontaminated photometry in the three IR bands (*J*, *H*, and *K*)[83].

[81] When the uncertainty represents the standard error of the measurement in a normal distribution, then there is about 68.2% probability that the true value of the measured quantity falls within one standard deviation of the mean value (http://en.wikipedia.org/wiki/Standard_deviation).
[82] https://www.sdss3.org/dr9/tutorials/flags.php
[83] http://www.ipac.caltech.edu/2mass/releases/allsky/doc/sec2_2a.html

5.5 *Dwarf-Giant Separation*

We collected stars which fall within the typical colour ranges for late-type K and M dwarfs: $r\text{-}i \gtrsim 0.47$ and $i\text{-}z \gtrsim 0.25$ (West et al. 2011). However, there may possibly be some contamination by giants in any colour-selected sample of M dwarfs which needs to be addressed in statistical studies of the Galaxy. Bessell & Brett (1988) found the *JHK* plane useful for distinguishing late-type dwarfs and giants. Figure 5.1 shows the (*H-K*)-(*J-H*) diagram for data combined from different studies taken from Bessell & Brett (1988). There is clearly a bifurcation between M giants and M dwarfs, mainly due to the appearance of TiO bands (where the M-dwarf sequence begins, see Chapter 1); the lower sequence refers to dwarfs and the upper to giants. It can be seen that the giant sequence extends to $H\text{-}K \cong 0.3$ and $J\text{-}H \cong 1.0$.

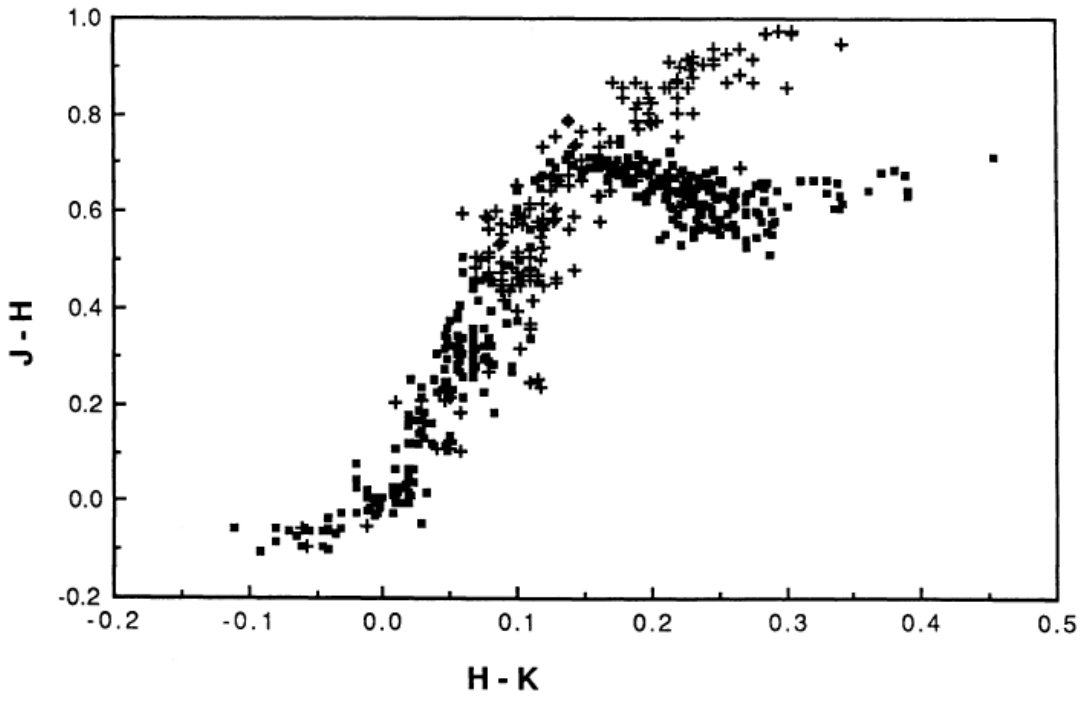

Figure 5.1 The (*J-H*) versus (*H-K*) diagram for a combined data taken from Bessell & Brett (1988). Giant stars are plotted as plus signs and dwarf stars as filled squares.

Using Figure (5.1), the NIR colour ranges typical of M giants are found to be $J\text{-}H > 0.8$ and $0.15 < H\text{-}K < 0.3$ (Covey et al. 2007). By applying these colour cuts, we realized that around 1%

of stars in our SDSS-2MASS sample are giants, consistent with other studies such as the samples of Covey et al. (2008) with less than 2% and West et al. (2011) with around 0.5% giant contamination.

It should be mentioned that this approach for separating giants from dwarfs is not accurate for K-type stars (Bessel & Brett 1988) as they overlap in *JHK* color space. A better way to remove giants employs reduced proper motions of stars as described in Mann et al. (2013b). By using a sample of stars with available proper motions, we can separate giants from dwarfs with higher accuracy.

5.6 *Photometric Parallax and Distance*

The distance and Galactic height of our stars were estimated by means of a photometric parallax technique developed in Bochanski et al. (2010). More specifically, the absolute magnitude in *r*-band, M_r, of low mass stars can be obtained from a colour- absolute magnitude relation given by

$$M_r = 5.190 + 2.474\,(r-z) + 0.4340\,(r-z)^2 - 0.08635(r-z)^3 \qquad (5.1)$$

which is valid for the colour range $0.50 < r\text{-}z < 4.53$ (or $0.32 < i\text{-}z < 1.85$, corresponding to the entire M type sequence, West et al 2011). To apply this relation, we selected only those stars which fall in this colour range. By having the values of M_r, the distance and Galactic height are calculated straightforwardly.

After meeting all requirements described above as well as the colour cuts applicable for our metallicity and temperature calibrations outlined in Chapter 4, we assembled 1,334,478 M dwarf stars for our metallicity and temperature calibration to be applied.

Summary

A large sample of over 1,300,000 late-type K- and early- to mid-type M dwarfs were selected from the merged SDSS and 2MASS catalog. To ensure our analysis will not be affected by reddening, we used the most widely used dust map to correct for Galactic extinction. Moreover, to reject sources with poor photometry, we selected those objects which meet some criteria for

having clean photometry. We also applied the colour cuts which are required to remove giant outliers. Since a photometric parallax is used to estimate the vertical distances (see Chapter 6), the colour cuts necessary for this parallax were also applied. Lastly, those stars which fall within the colour ranges necessary for our calibrations were collected.

In the next Chapter, our metallicity and temperature methods are applied to the SDSS-2MASS large sample and resulting distributions are discussed.

Chapter 6

Results

6.1 *Introduction*

In this Chapter, the metallicity and temperature calibrations outlined in Chapter 4 are applied to the M dwarf stars in the SDSS-2MASS sample. The resulting metallicity distribution can be employed to investigate the relation between the mean metallicity and Galactic height, and in turn, the relation between metallicity and age of M dwarfs. The luminosity-metallicity relation of M dwarfs can be studied statistically through the absolute magnitude distributions with different metallicity ranges. The temperature distribution of our sample and the correlation between the temperature and metallicity of our stars can also be examined.

In Section 6.2, we determine the Galactic height and metallicity distribution of M dwarfs. The Galactic height-metallicity relation of M dwarfs is explored in Section 6.3. The absolute magnitude distribution and its correlation with metallicity is discussed in Section 6.4. In Section 6.5, the M-dwarf metallicity distribution from this study is compared with those of FGK and M dwarfs from other studies. Finally, the temperature distribution is studied in Section 6.6.

6.2 *Galactic Height and Metallicity Distributions*

We applied Equation (4.1) to the sample of 1,334,478 stars described in Chapter 5, and separated those stars with metallicity $-0.73 \leq [Fe/H] \leq +0.3$, giving 1,320,839 stars whose distances, D, were calculated using Equation (5.1). We obtained the Galactic vertical distances of these stars, H, using

$$H = D \sin(b) \qquad (6.1)$$

where b denotes Galactic latitude. It should be remarked that these Galactic heights are the vertical distances from the plane passing through the Sun. Since all the selected dwarfs lie above this plane ($b \geq 50°$), we added the Galactic height of the Sun, $H_{\odot}$ = 20 pc (Jurić et al. 2008) to those derived from Equation (6.1) (which are raw data, uncorrected for geometrical effect) to obtain the Galactic heights from the plane passing through the Galactic center. We limited our studies to stars with $H \leq 2000$ pc, leading to a final sample of 1,312,005 M dwarfs (hereafter, "SampleMetal") having a median extinction in the r band of A_r=0.046 mag. The Galactic height distribution of SampleMetal is illustrated in Figure (6.1) as a dashed histogram, showing a peak around $H \cong 350$ pc. This distribution also indicates that about 94% of stars in SampleMetal are within the Galactic thin disk[84], $H \lesssim 1000$ pc (Gilmore & Reid 1983).

As mentioned above, only those stars with $b \geq 50°$ were selected. This means that stars outside an imaginary cone, perpendicular to the Galactic plane with an opening angle of 40° and apex at Earth, were excluded. As a result, stars with higher vertical distances are distributed through larger volumes of space. In order to remove the effect of this bias on height and metallicity distributions, it is necessary to perform a volume correction. To this end, the stars in SampleMetal were divided into 20 bins of 100 pc in height and the weighting factor proportional

[84] Studies have shown that the thin disk stars or population I stars ($z \lesssim 1$kpc) are young and have relatively high metallicity while the halo stars or population II stars ($z > 5$kpc) are old and metal poor. The thick disk stars or intermediate population II stars ($1 \lesssim z \lesssim 5$kpc) are somewhat younger than the halo stars and have relatively low metallicities compared to the thin disk stars (e.g., Gilmore & Reid 1983, Nykytyuk & Mishenina 2006, Navarro 2010, Brook et al. 2012). As a result, the Galactic halo is expected to be populated by low metallicity stars, but the thin and the thick disks must include more metal rich stars.

to the inverse of the volume of each bin was calculated. The number of stars in each bin was then multiplied by the corresponding weighting factor, leading to the volume-corrected height distribution. The normalized volume-corrected distribution is depicted as a solid histogram in Figure (6.1), showing a maximum at H ≅ 150 pc.

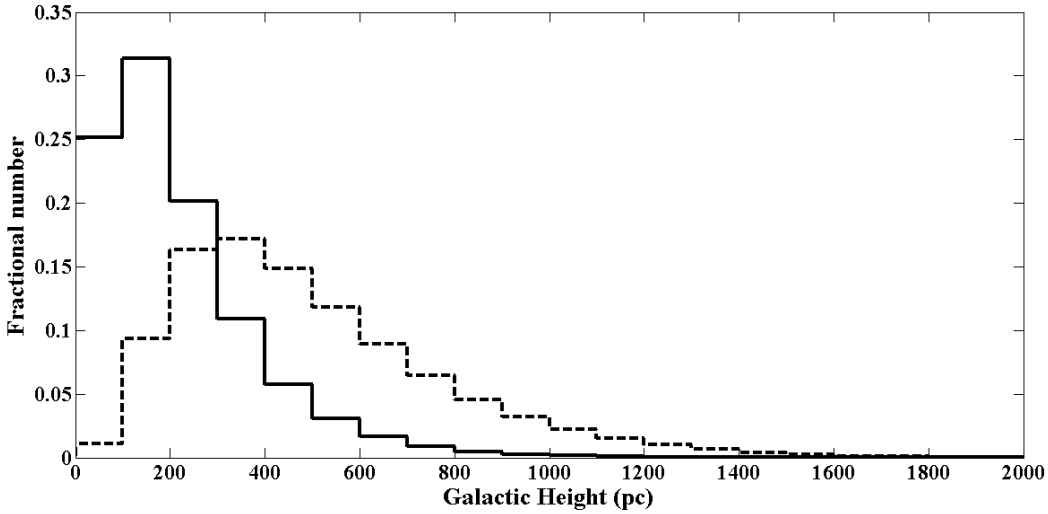

Figure (6.1) The observed Galactic height distribution of stars in SampleMetal (the dashed histogram) and the volume-corrected height distribution (the solid histogram)

The dashed histogram in Figure (6.2) shows the observed metallicity distribution of SampleMetal, peaking at ≅ -0.05 dex. To find the volume-corrected metallicity distribution, the metallicity distributions of the height bins described above were obtained separately and multiplied by the corresponding weighting factors. All these weighted distributions were then added together as the total volume-corrected distribution. The normalized volume-corrected distribution is illustrated in Figure (6.2) as a solid histogram. This distribution shows a maximum at around +0.05 dex, and a mean metallicity [Fe/H] ≅ -0.04 dex. Note that this mean metallicity is not expected to represent the true mean value of the local Galactic disk since those stars with metallicities outside the metallicity range of our calibration were removed from the sample. In order to obtain a more meaningful mean metallicity, a calibration valid over a wider range of metallicity is necessary.

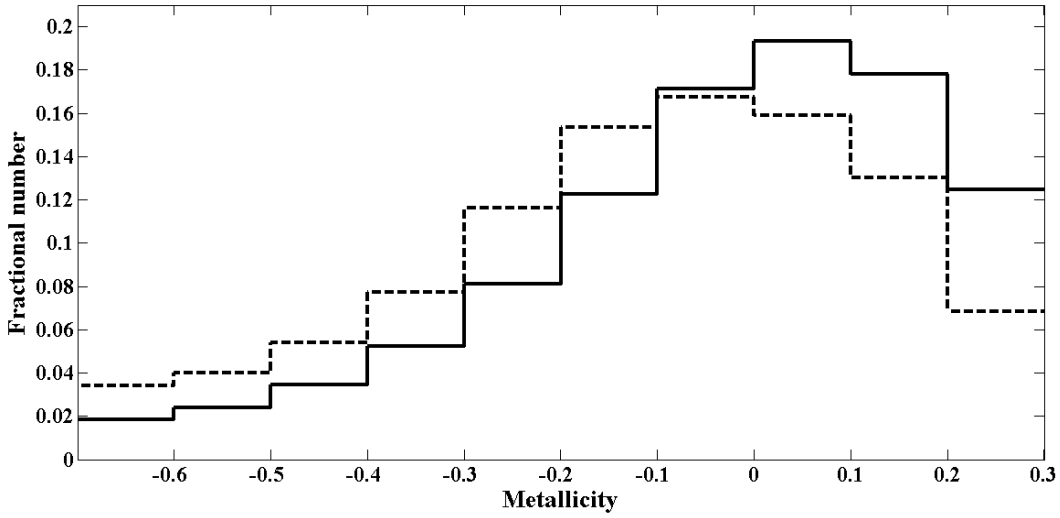

Figure (6.2) The metallicity distribution of stars in SampleMetal from the observed data (dashed histogram) and volume-corrected data (solid histogram)

6.3 *Metallicity-Galactic Height Relation*

The relation between metallicity and Galactic height can be investigated by determining the metallicity distribution of stars as a function of Galactic height. We divided a subsample of our stars with H $\leq$1600 pc into 16 bins of equal ΔH = 100 pc. The metallicity distribution associated with each bin is shown in Figures (6.3) and (6.4). There is a clear shift towards lower metallicities as height increases from 0 to 800 pc. However, no such a shift can be seen in distributions between 800 and 1600 pc in Figure (6.4); the fraction of metal-rich stars slowly decrease and the distributions become more metal-poor with increasing height. The change of distributions between 800 and 1600 pc is less pronounced than those between 0 and 800 pc, indicating a decrease in vertical metallicity gradient as a function of height. Overall, the mean metallicity decreases as height rises from 0 to 1600 pc which is consistent with the age-metallicity-height relation. Studies have shown that stars which formed at earlier times of the Galaxy's history, in general, have lower metallicities and are on average farther from the Galactic plane. Stellar systems in the Galaxy are formed from interstellar gas and, at the end of their lifetimes, they may return a substantial fraction of their initial masses to the interstellar medium (ISM) through stellar winds and supernova explosions. Since the returned material is enriched with elements heavier than hydrogen and helium, these processes can change the metal

content of the ISM. With the passing of time, succeeding generations of stars become more metal-rich than their ancestors (e.g., Pagel 2009; Mo et al. 2010), implying an age-metallicity relation: older stars are, on average, more metal-poor than younger ones. Evidence of this kind was offered by Casagrande et al. (2011) who determined the metallicity distributions of three samples of solar-type stars with different ranges of age (Figure 16 of their paper). The authors showed that young stars (ages < 1 Gyr) have a quite narrow distribution around higher values of metallicity, whereas intermediate-age (between 1 and 5 Gyr) and old-age (> 5 Gyr) stars present broader distributions, significantly extending to lower metallicities. Clearly, the old-star sample includes larger fractions of metal-poor stars than the young-star one, implying a relation between age and metallicity.

In addition to the age-metallicity relation, there is also a relation between age and velocity dispersion[85]. Observations have demonstrated that old stellar populations in the disk have larger velocity dispersions. The term "dynamical heating" is applied to all processes (interaction of stars with perturbers) that cause an increase in velocity dispersion with age.

However, there are different views about the duration of this heating. One view suggests that the stellar velocity dispersion rises steadily at all times as $\sim t^{0.2-0.5}$ where t denotes the time (Wielen 1977). Another opinion is that the heating occurs for the first $\sim$ 2 Gyr but then saturates (Quillen & Garnett 2000). Due to the increased motions, stars will spend a larger fraction of time out of the thin disk where the sources of heating (perturbers) reside and the scattering becomes less effective, causing the motion of stars to level off.

Different mechanisms are responsible for the in-plane and vertical dynamical heating (e.g., Nordström 2008). While the in-plane motions reflect complicated kinematical substructures, the vertical velocities indicate an essentially pure Gaussian distribution at all ages (Seabroke & Gilmore 2007; Nordström 2008). However, the mechanisms characterizing the observed vertical motions are not well-understood. Several scenarios have been suggested for such a mechanism in the thin disk, some of which are (Nordström 2008; Freeman 2011):

[85] The velocity dispersion is the statistical dispersion of velocities about the mean velocity for a group of objects, such as an open cluster, globular cluster, or galaxy cluster (http://en.wikipedia.org/wiki/Velocity_dispersion).

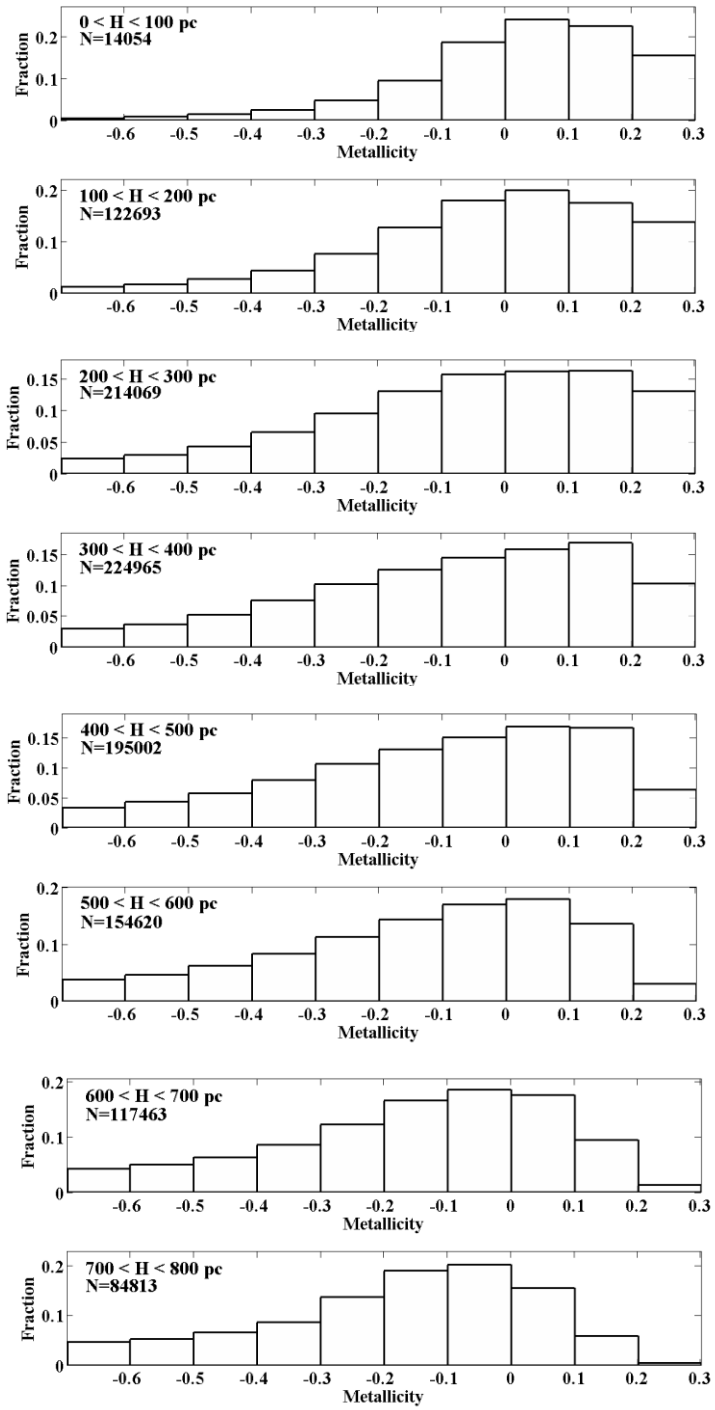

Figure (6.3) The metallicity distributions of M dwarfs in the large sample with different Galactic height ranges between 0 and 800 pc. The height range and number of stars for each distribution are labeled on the corresponding plot.

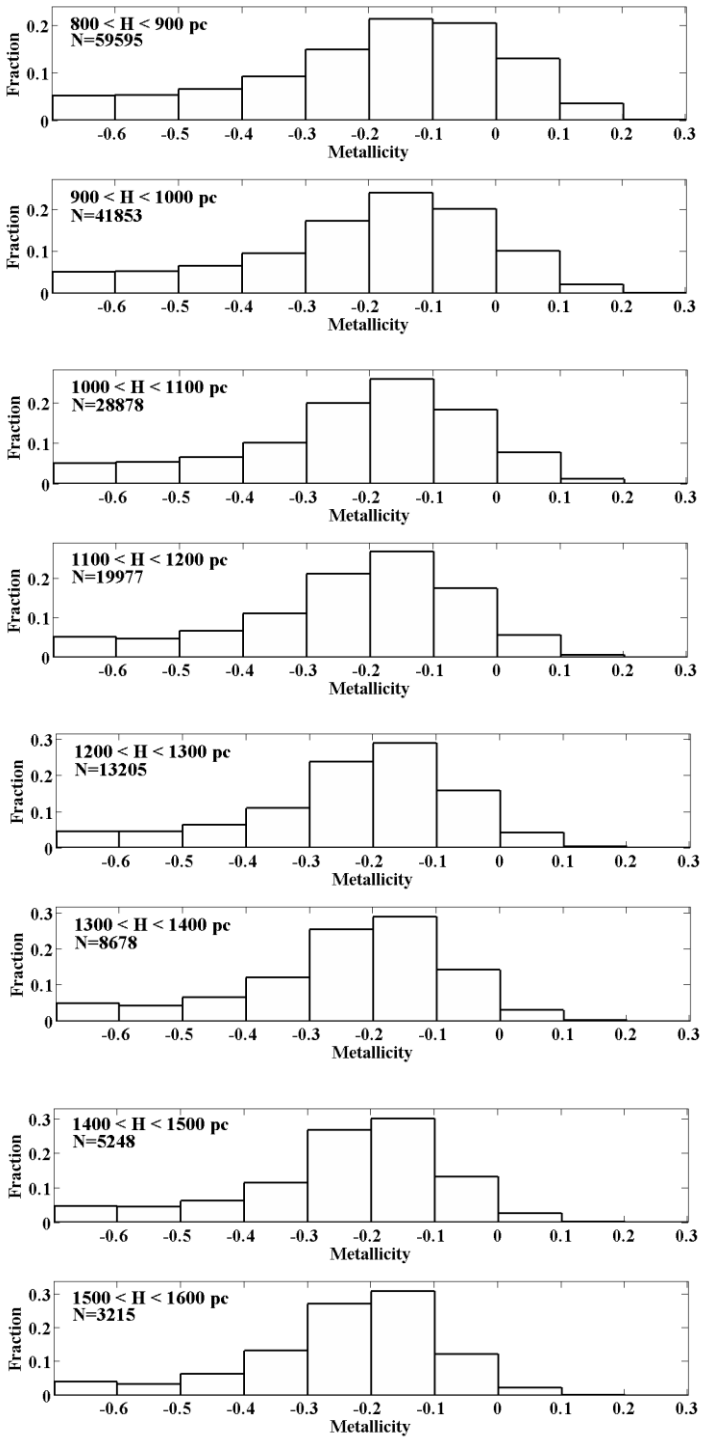

Figure (6.4) The metallicity distributions of M dwarfs in the large sample with different Galactic height ranges between 800 and 1600 pc. The height range and number of stars for each distribution are labeled on the corresponding plot.

1- Scattering of stellar orbits by encounters with large mass concentrations in the ISM such as giant molecular clouds (GMCs)

2- Interaction of stars with transient spiral arms[86]

3- Hierarchical mergers for galaxy formation

Whatever the mechanism is, due to the vertical motions, stars dissipate from the Galactic plane, increasing their vertical distance from the plane in the course of time. One can therefore expect that the older, more dynamically heated stars should be found, on average, at larger Galactic heights than the younger stars. As a consequence, stars farther from the Galactic plane should be on average more metal-poor than those closer to the plane.

Using a metal-sensitive ratio, (CaH2 + CaH3)/TiO5, from Lépine et al. 2003 as a proxy for M-dwarf metallicity, West et al. (2008) demonstrated a decrease in metallicity as a function of Galactic height (up to 1000 pc) which implies that the more distant stars from the Galactic plane have lower metallicities[87]. In an interesting simulation by West et al (2006; 2008), a simple one-dimensional model of the thin disk was applied to investigate the vertical motions and positions of M dwarfs over the Galaxy's lifetime. They also showed a decrease in activity fractions (as traced by Hα emission) as a function of Galactic height for all M-dwarf spectral types, indicating a decline in the magnetic activity of older M dwarfs. All results from this 1D dynamical simulation indicate a good consistency between the model and observed activity and velocity trends.

6.4 *Metallicity-Absolute Magnitude Relation*

The dashed line in Figure (6.5) represents the observed absolute magnitude (M_r) distribution of SampleMetal, showing a considerable number of stars with absolute magnitudes between +8 and +12 mag.

[86] A transient spiral arm appears and disappears over time, as contrasted with a stationary spiral arm which is long lived and persistent. Stationary spiral arms do not affect the stellar motion in the vertical direction significantly (Nordström 2008).

[87] Recently, West et al. in the Cool Stars 18, 2014 applied a new photometric metallicity to a very large sample of M dwarfs and the decrease in metallicity as a function of Galactic height was nicely represented.

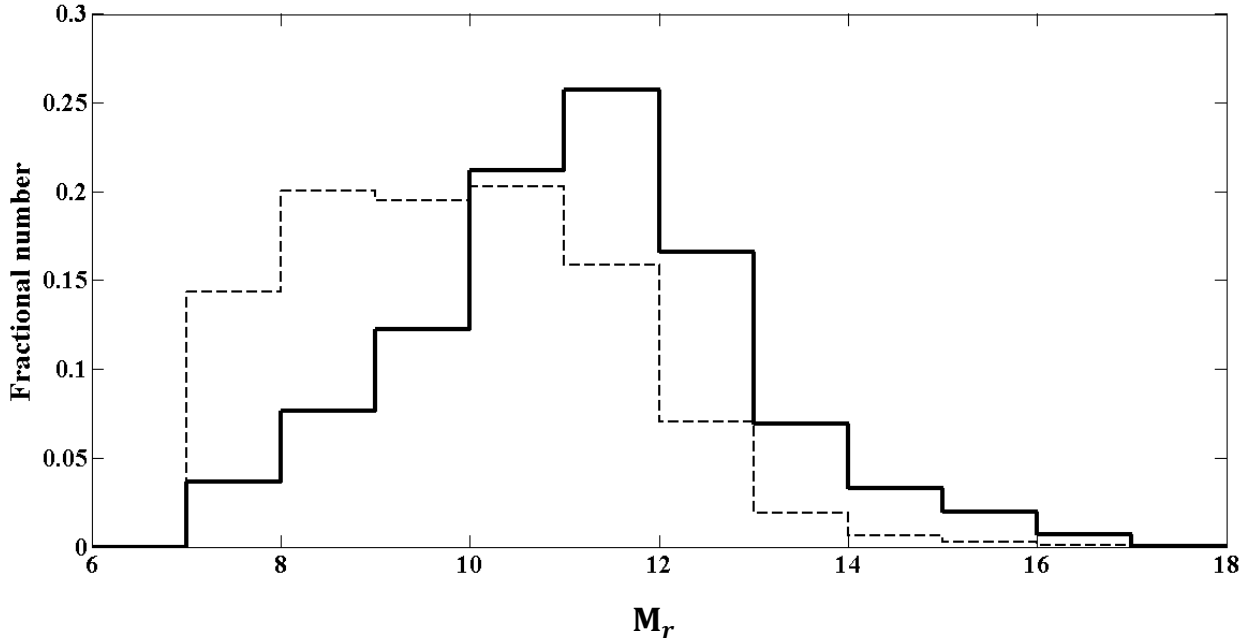

Figure (6.5) The observed absolute magnitude distribution of stars in SampleMetal (the dashed histogram) and the volume-corrected distribution (the solid histogram).

Similar to the metallicity distribution, we determined the absolute magnitude distribution of each Galactic height bin and then added them together, leading to the volume-corrected distribution of the entire sample. The fractional volume-corrected absolute magnitude distribution is illustrated as a solid line in Figure 6.5. In a magnitude-limited sample[88], the faint stars are more detected in closer distances. By the volume correction described above, the contributions of stars in smaller heights were increased while those of larger heights were decreased. As a result, the volume-corrected absolute magnitude distribution is fainter than the uncorrected one.

To trace the relation between metallicity and absolute magnitude, we determine the volume-corrected absolute magnitude distributions of stars in SampleMetal with different metallicity ranges, as shown in Figure (6.6). Our results indicate that the distributions of metal-poor M dwarfs have higher fractions of brighter stars than those of metal-rich M dwarfs. However, we cannot readily conclude that metal-poor dwarfs are more luminous than metal-rich ones as the difference between the luminosity distributions of different metallicity intervals could be, totally

[88] In magnitude-limited samples, stars below a certain apparent brightness are not included.

or partially, a consequence of the existing bias in our magnitude-limited sample. As already stated, the metallicity distribution of M dwarfs tends to be more metal-poor as height increases. This means that the metal-poor M dwarfs are more likely to be found at higher Galactic heights and, on average, have larger distances than metal-rich dwarfs. In a magnitude limited sample, the detected lower-metallicity M dwarfs are, on average, more luminous than higher-metallicity one. To find a more accurate statistical relation between absolute magnitude and metallicity, the effect of this bias must be removed.

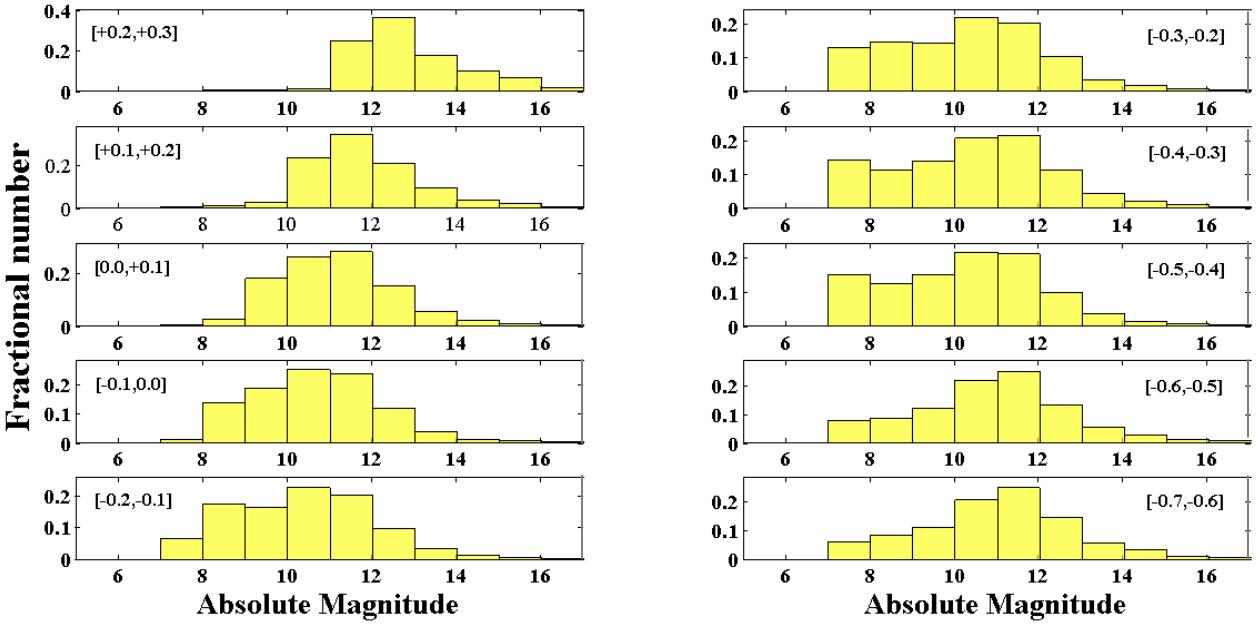

Figure (6.6) The volume-corrected absolute magnitude distributions for 8 subsamples of different

Some studies favour a decrease in luminosity as a function of metallicity. For example, Laughlin (2000) argued that since metal-poor stars are brighter than their metal-rich counterparts of the same mass, there was no observational bias against metal-poor stars in his study. He also pointed out that doubling the metallicity of a solar-mass star from zero to +0.3 dex leads to a 320 K decrease in effective temperature and a factor of 1.3 decrease in luminosity. Using theoretical models of low-mass stars, Cassisi (2011) showed that the HR locus became cooler and fainter with increasing heavy element abundances. We applied the isochrones for low-mass stars of age 5 Gyr (the mean age of Galactic disk) and three different assumed metallicities (0.0, -0.5, and -1.0 dex) taken from Baraffe et al. (1998) and then plotted the luminosity versus mass for these

isochrones, as shown in Figure (6.7). It is clear that at a given mass, the lower-metallicity stars are more luminous than higher-metallicity ones.

To the contrary, Woolf & West 2012 took a different approach and argued that since low-metallicity main sequence stars (subdwarfs) are less luminous than higher-metallicity stars of the same temperature or spectral type, higher metallicity stars should be overrepresented in magnitude-limited samples. In other words, metal-poor M dwarfs must be, on average, closer than the metal-rich ones in such samples. Figure (6.8) represents the luminosity versus temperature of the isochrones described above, showing an increase in luminosity as metallicity rises for a given temperature. Using a sample of stars from Woolf et al. (2009) for which parallax data were available, Woolf & West (2012) derived the luminosity variation with metallicity for M dwarfs in the temperature range $3500 \leq T_{eff} \leq 4000$ K. Based on this variation, they calculated a volume correction factor for different values of [Fe/H] (Table 1 in their paper). Another example which supports this view is the work of Schlesinger et al. (2012) on a sample of G and K dwarfs. In this study, it was noted metal-rich stars are brighter than metal-poor ones for a given *g-r* colour. Therefore, the volume coverage of the sample varies with respect to metallicity for the same magnitude range. Schlesinger et al. specified distance limits for their sample to ensure that there was no bias due to the metallicity-dependent volume coverage.

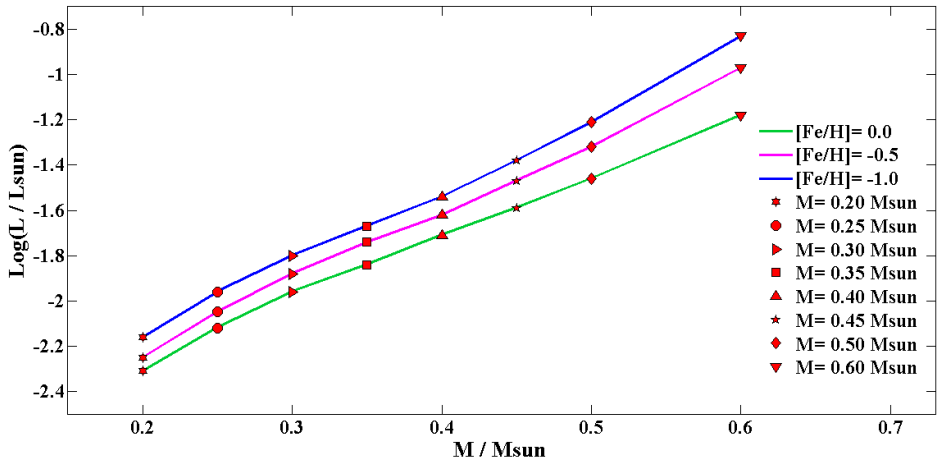

Figure (6.7) The luminosity versus mass for the isochrones of age 5 Gyr and three different metallicities. The metallicities are colour-coded and the masses are symbol-coded.

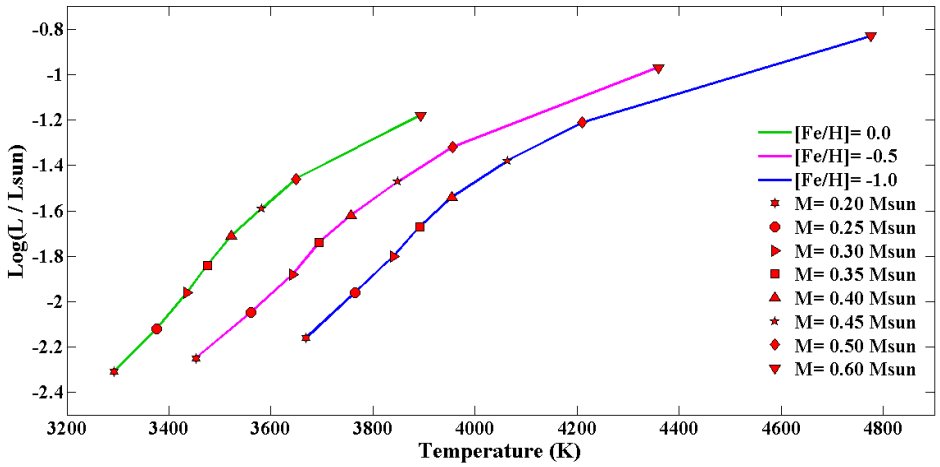

Figure (6.8) The luminosity versus temperature for the isochrones of age 5 Gyr and three different metallicities. The metallicities are colour-coded and the masses are symbol-coded.

Considering the two opposite views described above, in order to make an appropriate volume correction to a magnitude-limited sample like ours, more investigations on the relation between absolute magnitude and metallicity are required.

6.5 *Comparison with Previous Studies*

In this section, we compare our volume-corrected M-dwarf metallicity distribution with previous studies of FGK dwarfs. Figure (6.9) shows such comparisons with the distributions of G and K dwarfs in the Sloan Extension for Galactic Understanding and Exploration (SEGUE) survey from Schlesinger et al. (2012) for three different Galactic height ranges. As noted in Schlesinger et al. (2012), the G- and K- dwarf metallicity distributions have more metal-poor stars as height increases. It can be seen that the M-dwarf distribution exhibits the same trend, which implies a similar star formation history as G and K dwarfs. There is also a discrepancy between the distributions of different spectral types; the cooler spectral type, the more metal rich the distribution includes.

We reproduced several distributions from some other studies for comparison, as shown in Figure (6.10). The blue line shows the M-dwarf distribution of the whole SDSS-2MASS sample from this work, and the black line represents another M-dwarf distribution from Woolf & West (2012) who studied the metallicity of M dwarfs in a large sample (including 4141 M dwarfs) of the spectroscopic SDSS catalog for first time. It should be noted that Woolf & West used Equation (3.3) to determine the metallicity of stars. As shown in the Figure, there is no offset between the

peaks of the two M-dwarf distributions, however, it appears that our sample includes larger fractions of metal-poor stars than in that of Woolf & West. Moreover, the distribution of Woolf & West has a steeper slope towards low metallicities than ours. As already described in Chapter 3, the metallicity index ζ used in Equation (3.3) does not always diagnose metal-poor M dwarfs correctly, and it may identify such stars as near solar-metallicity ones. This could overestimate low-metallicity values as those of higher metallicities, causing a bias toward metal-rich stars in the distribution. The dashed red histogram in Figure (6.11) demonstrates the metallicity distribution of 5691 F and G dwarfs in the Radial Velocity Experiment Data Release 3 (RAVE DR3) from Duran et al. (2013). This distribution has a peak at around 0.3 dex and a steeper drop towards low metallicities as compared to our M-dwarf distribution. We also represented the metallicity distribution of over 13,000 F, G and K dwarfs of the Galactic disk in the SDSS DR7 from Zhao et al. (2013), as a dashed green line. The histogram peaks at about -0.4 dex, showing a shallow slope towards low-metallicity values with respect to the other distributions. Overall, the FGK-dwarf metallicity distributions are more metal-poor relative to the M-dwarf distributions.

Johnson & Apps (2009) argued that the M and FGK dwarfs in the local Galactic thin disk should have the same metallicity distributions and that there should not be a systematic offset between M- and FGK-dwarf metallicity distributions. They related the offset between the metallicity distributions of M dwarfs and FGK dwarfs in some published papers (e.g., Bonfils et al. 2005) to the reliability of the methods by which the metallicity of M dwarfs were determined. Accordingly, they adopted the mean M dwarf metallicity of their sample to be the same as the mean metallicity of a volume-limited sample of FGK dwarfs ($< [Fe/H] > \cong -0.05$ dex) from Valenti & Fischer (2005). Schlaufman & Laughlin (2010) improved upon Johnson & Apps (2009) and remarked that for a fair comparison between samples of M dwarfs and FGK dwarfs in the local Galactic disk, the samples must not only be volume corrected but also have equivalent kinematics. By selecting two volume-completed, kinematically-matched samples of FG and M dwarfs, Schlaufman & Laughlin (2010) derived a mean metallicity of $<[Fe/H]> \cong -0.14 \pm 0.06$ dex for M dwarfs in the solar neighborhood. It should be mentioned that we compared our distribution to those of previous works without any consideration of kinematics of the samples under study. To make proper comparisons between the metallicity distributions of dwarf stars

with different spectral types, volume-corrected samples with equivalent kinematics have to be considered.

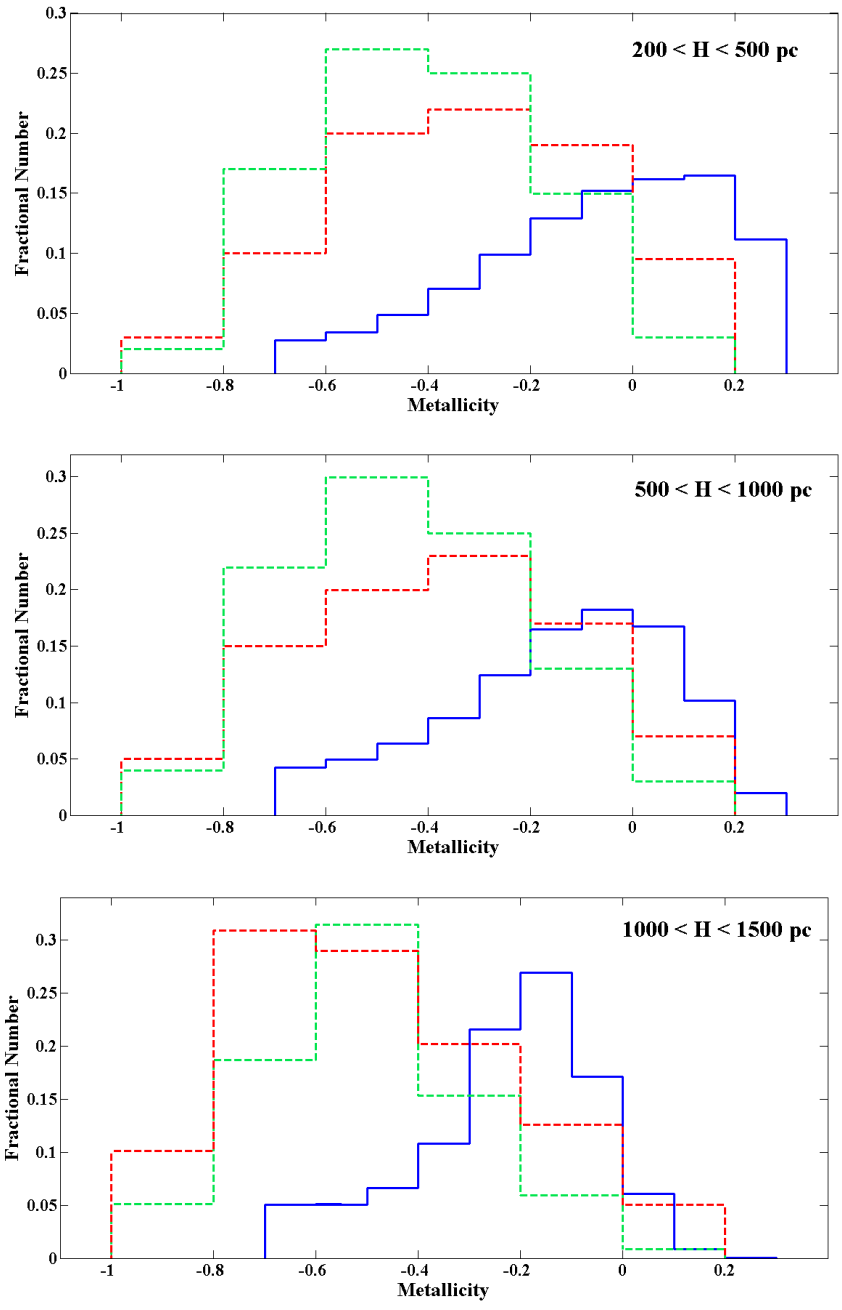

Figure (6.9) The comparison between the metallicity distribution of M dwarfs (blue line) from this study and those of G dwarfs (dashed green line) and K dwarfs (dashed red line) from Schlesinger et al. (2012) for different height ranges.

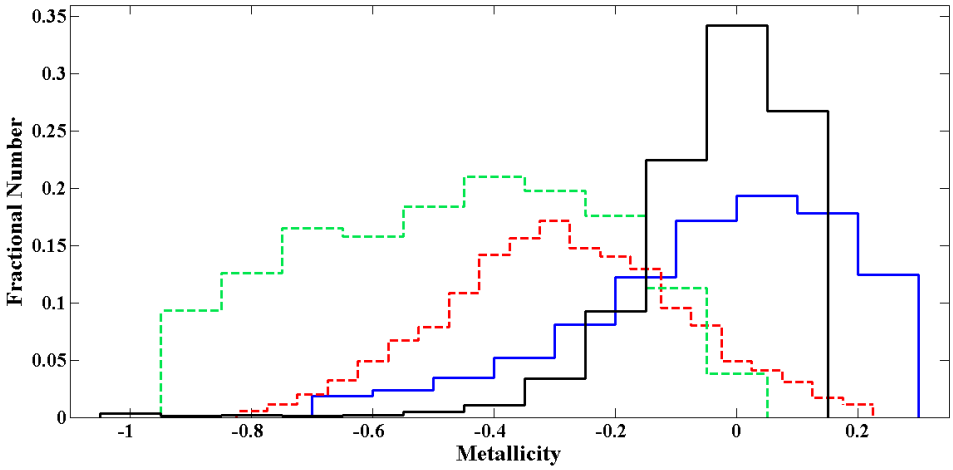

Figure (6.10) The comparison between the M-dwarf metallicity distribution from this work (blue line), the M-dwarf distribution from Woolf & West (2012) (dashed black line), the FG-dwarf distribution from Duran et al. (2013) (dashed red line), and the FGK-dwarf distribution from Zhao et al. (2013) (dashed green line).

On the other hand, the offset between FGK- and M-dwarf distributions might be explained in other ways. For example, similar to Schlesinger et al. 2012, one may expect that since M dwarfs have longer lifetimes than G and K dwarfs, there is a possibility that more metal-rich G and K dwarfs have evolved off the main sequence, causing a metallicity bias in G- and K-dwarf distributions against high-metallicity values which does not happen for cooler M dwarfs. Furthermore, if more lower-mass stars are born as the metallicity of interstellar gas increases, there should be fewer metal-poor M dwarfs than G and K dwarfs.

While there have been discrepancies between the metallicity distributions of different spectral types from various studies and some effort has been made to explain them, we can mention the work of Casagrande et al. (2011) whose metallicity distribution of solar type stars (obtained by a photometric method) has a peak around [Fe/H] $\cong$ 0, very much similar to the M-dwarf distributions shown in Figure (6.11). This is in consistent with the statement of Johnson & Apps (2009) who pointed out there should not be any offset of different metallicity distributions. Refer to the studies of Haywood (2001), Taylor & Croxall (2005), Luck & Heiter (2006), and Fuhrmann (2008) for more examples of metallicity distributions favouring a peak around solar metallicity.

Accurate metallicity distributions of dwarf stars can provide important constraints on Galaxy evolution models. We should always keep in mind that to make a proper comparison, both observationally and kinematically unbiased samples have to be compared. In this study, we did not make any such corrections to our sample. To have a volume-corrected sample, a larger M-dwarf calibration sample with available parallaxes is required for finding an accurate relation between the luminosity and metallicity of M dwarfs. Nevertheless, we do not expect these corrections would change the location of the peak in the distribution significantly and the comparisons made in this section give us, to some extent, important information about the Galactic evolution.

6.6 *Temperature Distribution*

We applied our method developed in Chapter 4 for the determination of M-dwarf temperatures using the synthetic SDSS-2MASS (*g*-*K*)-(*J*-*K*) diagram. We obtained the temperature of stars in SampleMetal and separated those with $3000 \leq T_{eff} \leq 4000$ K and $g\text{-}K < 6.9$. The observed temperature distribution of SampleTemp is indicated in Figure (6.11) as a dashed histogram which has a maximum at ≅ 3,500 K corresponding to the spectral type ≈ M2.5. By adding the temperature distributions associated with the Galactic height bins of 100 pc (see above), we determined the normalized volume-corrected temperature distribution which is shown in Figure (6.11) as a solid line. Although this corrected distribution peaks at the same temperature as the uncorrected one (T_{eff} ≅ 3350 K), it includes cooler stars.

We examined the temperature distributions for subsamples of stars with different ranges of metallicity and did not find any clear relation between temperature and metallicity. A calibration sample with more trustworthy temperatures is required to derive a more accurate temperature calibration, and accordingly, a more reliable temperature distribution.

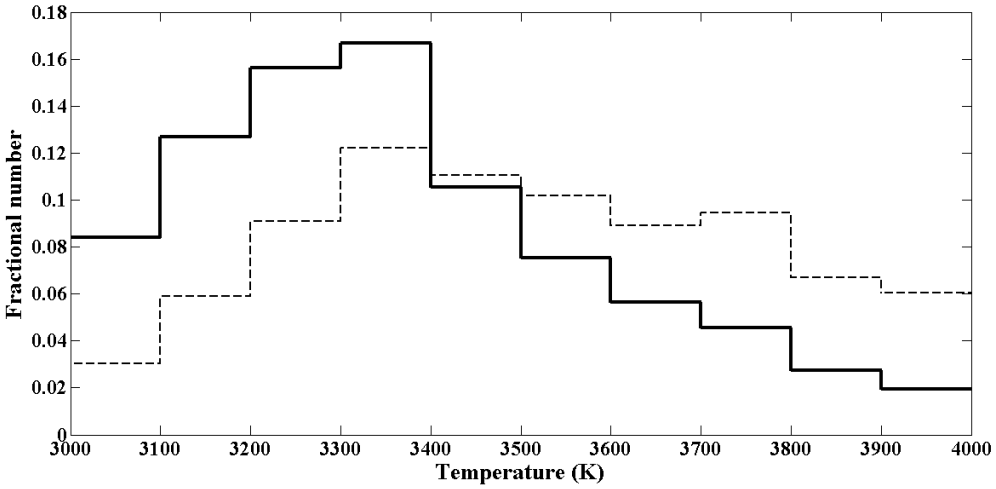

Figure (6.11) The observed temperature distribution of stars in SampleMetal (the dashed histogram) and the volume-corrected distribution (the solid histogram) with temperatures between 3000 K and 4000 K.

Summary

The metallicity distribution of an M-dwarf sample, including over 1.3 million M dwarfs, was studied. The metallicity distributions of subsamples with different Galactic height ranges show that there is a decrease in mean metallicity with Galactic height, indicating that older stars have, on average, lower metallicity than younger ones.

While we found an increase of luminosity with decreasing metallicity, this could be a result of the bias present in our magnitude-limited sample. To find a precise relation between the luminosity and metallicity, this bias needs to be identified and removed from the sample.

The metallicity distribution from this work was compared with those of FGK and M dwarfs from several previous studies, implying a systematic offset between distributions of different spectral types, with earlier types being more metal-poor than later types. This offset could be due to various metallicity calibrations employed in different studies, or caused by different lifetimes or star formation rates of stars with different spectral types. For an accurate explanation, more investigations are needed.

The temperature distribution of our M dwarfs indicates a significant number of stars with a spectral type of $\approx$ M2.5. However, we did not find a relation between the temperature and metallicity of M dwarfs. To derive a better temperature calibration, we require a larger sample of M-dwarf calibrators with more reliable temperatures.

Chapter 7

Testing Models of Galactic Chemical Evolution

7.1 *Introduction*

Galactic Chemical Evolution (GCE) is the study of the evolution of the transformation of gas into stars during star formation (SF) and of the resulting evolution of the chemical composition of the Galaxy. Each star burns H and He in its core and produces heavy elements (metals). Some faction of the metals is returned into the interstellar gas at the end of the star's life through winds and supernova explosions. The remaining metals are locked into the remnant of the star. The chemical abundance of the gas in a galaxy should therefore evolve in time, and accordingly, subsequent generations of stars formed from the metal-enriched interstellar gas have higher values of metallicity than preceding ones. The net result of all these processes is to produce a local Galactic abundance distribution in our neighborhood with a typical hydrogen mass fraction $X \cong 0.70$, helium mass fraction $Y \cong 0.28$, and metal mass fraction $Z \cong 0.02$ mostly including O, C, N, Ne, Mg, Si and Fe (Anders & Grevesse 1989).

In the field of GCE, there are two kinds of elements; primary and secondary elements. Primary elements are produced exclusively from the initial H and He of the star (the abundances of which vary little throughout galactic history), such as C, O, Ne, and Fe. Secondary elements are

generated from metals already present in the star at birth, for example, N which is produced from initial C and O in the CNO cycle[89] (Prantzos 2007).

To better understand the evolution of the Galaxy, different kinds of progressively more sophisticated models of GCE have been developed. The basic ingredients to build such models can be summarized as:

- Initial conditions
- Star formation rate
- Stellar yields (i.e., how elements are produced in stars and restored into the ISM);
- Gas flows (inflow and outflow).

When all these ingredients are determined, a set of equations must be written to describe the evolution of the gas and its chemical abundances. By solving these equations, three variables can be calculated: the mass of gas (g), the abundance of the metal element(s) of interest in the gas (Z), and the mass existing in the form of stars (s). One can expect that the metallicity of stars must be less than that of the gas. The metal yield P is defined as the ratio between the mass of newly produced metals (i.e., those metals created in the star via nucleosynthesis) and the total mass which remains locked up in the star or its remnant. Note that the yields of primary elements are independent of the stellar metallicity, while those of secondaries increase with it. Considering the metallicity relation for the local interstellar gas

$$[Fe/H] = \log (Z/Z_{\odot}) \qquad (7.1)$$

in which Z and $Z_{\odot}$ are the iron mass fraction of the interstellar gas and Sun, respectively, a plot of $ds/d[\log(Z/Z_{\odot})]$ versus $\log(Z/Z_{\odot})$ represents the metallicity distribution of stars[90]. By determining such model distributions, it would be possible to compare them with observed distributions and test the models. It should be remarked that the low-mass stars with less than

[89]The CNO cycle (for carbon–nitrogen–oxygen) is one of the known sets of fusion reactions by which stars convert hydrogen to helium. The proton-proton (PP) chain is another fusion reaction dominant in stars with masses less than the Sun's. For more details see: http://en.wikipedia.org/wiki/CNO_cycle

[90] Since "s" denotes the star mass with metallicity <Z, a graph of "s" versus log ($Z/Z_{\odot}$) shows a cumulative metallicity distribution. Therefore, by using the derivative of s relative to log ($Z/Z_{\odot}$), instead of s, for the y-axis, we can obtain the normal metallicity distribution.

one solar mass have such long lifetimes that they do not play any significant role in GCE (except perhaps minor effects of flares and dwarf novae) and simply serve to lock up some part of the gas and remove it from the birth-death circulation of stars. However, they have remained visible as archaeological tracers of the composition of the ISM (Pagel 2009). As a result, these small stars are often used to constrain the parameters in the models of GCE.

In section 7.2 the Simple Closed Box Model (SCBM) is addressed and compared to our metallicity distribution. The SCBM with initial metal abundances is studied and tested in Section 7.3. A simplified version of inflow gas models with declining rates are examined and discussed in Section 7.4.

7.2 *The Simple Box Model and the M dwarf Problem*

The simplest model of GCE is the "Simple Closed Box Model" (SCBM, Schmidt 1963). Based on the SCBM:

- The system is isolated and there is no mass inflow and outflow,
- There are two types of stars; those that live forever and those that die right after their birth, indicating instantaneous recycling,
- The system initially starts off full of metal-free gas and eventually ends up full of stars.

Studies on the chemical evolution of the local G dwarfs (e.g., van den Bergh 1962, Pagel & Patchett 1975, Wyse & Gilmore 1995) have shown the existence of the "G dwarf problem", which indicates that the SCBM predicts many more low metallicity G dwarfs than those are observed. That is, the model overestimates the number of metal-poor stars compared to what have actually been detected in many surveys. Similarly, the "K-dwarf problem", a paucity of metal-poor K dwarfs relative to the prediction of the SCBM, has also been perceived (e.g., Casuso & Beckman 2004). Woolf &West (2012) were the first to recognize the "M-dwarf problem"; as shown in Figure 2 of their paper, the number of low metallicity M dwarfs is not sufficient to match the SCBM, similar to G and K dwarfs.

To test the SCBM, we compare our metallicity distribution with that predicted by this model. Using the basic equations of the model, it can be shown (Pagel 2009; Mo et al. 2010) that the number of stars with metallicities between Z and Z + dZ is proportional to

$$N_*(Z)\, dZ \propto \exp(-Z/P)\, dZ. \quad (7.2)$$

Considering Equation (7.1), the number of stars with metal abundances between [Fe/H] and [Fe/H] + d[Fe/H] can be determined by:

$$N_*([Fe/H])\, d[Fe/H] \propto Z\exp(-Z/P)\, d[Fe/H] \quad (7.3)$$

which can be rewritten as

$$N_*([Fe/H]) \propto Z \exp(-Z/P). \quad (7.4)$$

The proportionality (7.4) is the metallicity distribution function predicted by the SCBM. Figure 7.1 compares the normalized distribution[91] from the model (the curve) with our volume-corrected metallicity distribution (the histogram). We found that the SCBM distribution with P = 0.022 has a maximum at the same metallicity as our histogram ([Fe/H] = +0.05 dex). This value of P can be compared with the rough estimate of the yield for the solar neighborhood, $\cong 0.012 \pm 0.056$ (Mo et al. 2010), indicating a factor of 1.83 discrepancy. It is also obvious that the SCBM cannot reproduce the low metallicity tail of the distribution. Our M dwarf distribution has a steeper drop in the number of stars with decreasing metallicity than the distribution obtained from the SCBM, which overpredicts the number of metal-poor M dwarfs, implying the existence of the M dwarf problem.

Clearly, some of the assumptions in the SCBM, such as instantaneous recycling, the system's isolation without gas flow or the assumption of a zero initial metallicity are unrealistic. The G and K dwarf problems have motivated a generation of more complicated GCE models. We will address a few such models and test them using our M-dwarf metallicity distribution in the following sections.

[91] This is a distribution whose area under the curve is equal to that of the observed metallicity histogram.

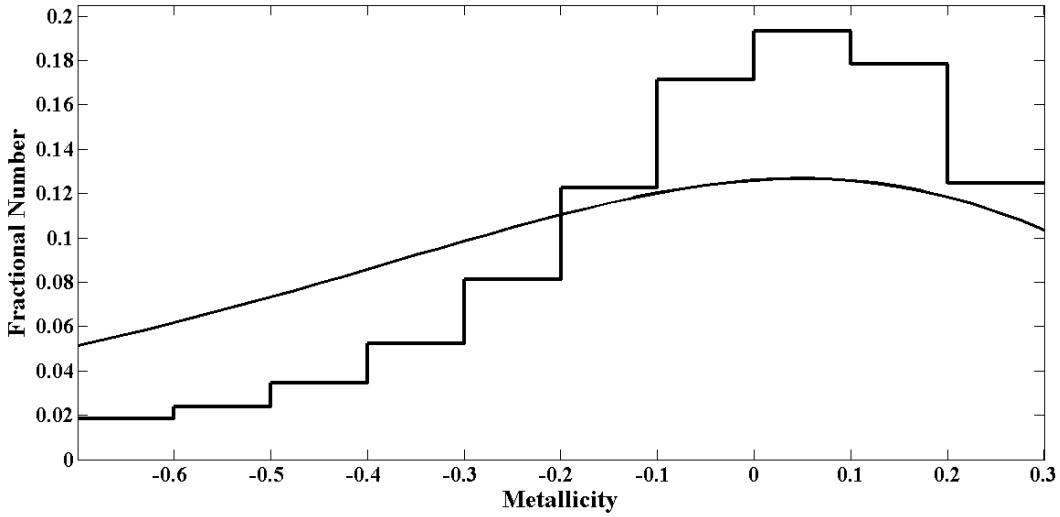

Figure 7.1 Comparison between the volume-corrected metallicity distribution of our sample (the histogram) and that predicted by the SCBM (the curve).

7.3 *The SCBM with Pre-enrichment*

One of the solutions proposed for G dwarf problem is to assume an initial metallicity of $Z_0 \neq 0$ (Prantzos 2007, 2011). If, for some reason, there is a finite initial abundance of order $[Fe/H]_0 \approx$ -1 dex, a good fit to the distribution is obtained at the expense of rejecting some stars with low metallicity. In this case, all metallicities (Z) in Equation (7.4) are replaced by $Z - Z_0$ yielding

$$N_* ([Fe/H]) \propto (Z - Z_0) \exp [- (Z - Z_0)/ P]. \quad (7.4)$$

Figure 7.2 demonstrates the comparison between the M-dwarf metallicity distribution (the histogram) and two normalized distributions calculated by the SCBM with selected initial metal abundances of Z_0 = 0.002 (the red curve) and 0.003 (the blue curve), and yield values of P = 0.020 and 0.019, respectively. The quantity P in the relation above was treated as a fitting parameter and found such that the distributions peak at the same metallicity as our histogram. For a better comparison, the distribution of the SCBM with no pre-enrichment (the black curve) is also overplotted. As can be seen, the distributions of the SCBM with a pre-enrichment give a better fit to our metallicity distribution than that without any initial abundance (the black curve).

There have been several hypotheses to justify such a pre-enrichment. For example, this could come from prior star formation activity in the halo (Ostriker & Thuan 1975) or the bulge. However, it has been argued (Prantzos 2007) that while the Galactic halo reached a maximum metallicity of $Z \sim 0.002$ ($0.1Z_{\odot}$), its mean metallicity is $Z \sim 0.0006$ ($0.03Z_{\odot}$) and its total mass (2×10^{9} $M_{\odot}$) is 20 times less than that of the disk (4.5×10^{10} $M_{\odot}$). Accordingly, there could not be enough mass and metals in the halo to justify an initial enrichment of the disk.

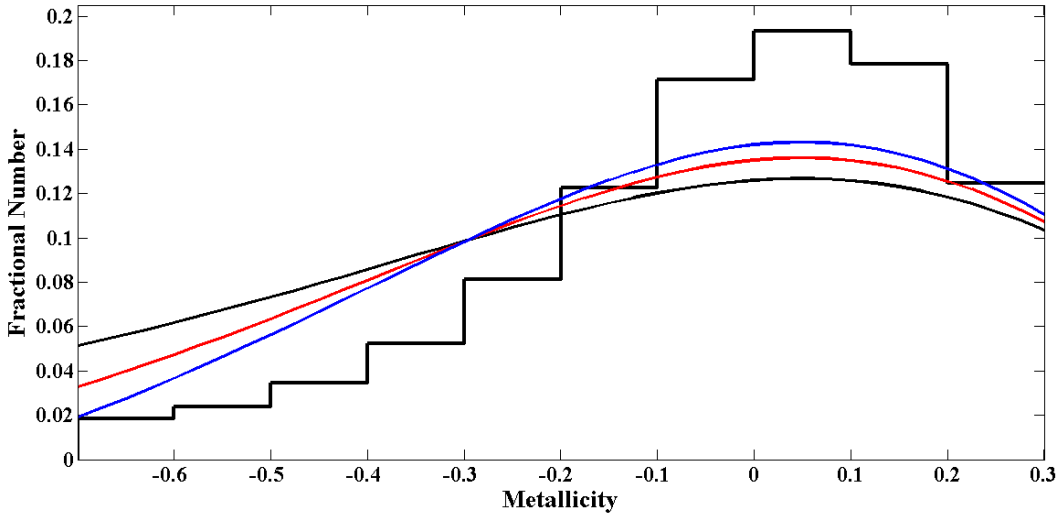

Figure 7.2 The comparison between the metallicity distribution of M dwarfs from this study (the black histogram) and those from the SCBM with different initial metallicities: $Z_0 = 0$ (the blue curve), 0.002 (the red curve), and 0.003 (the green curve).

Köppen & Arimoto (1990) suggested a model in which the bulge evolves with a large yield ($P \approx 0.034$) and ends star formation by ejecting 1/10 of its mass as highly enriched gas with an abundance of 0.05 (i.e., $2.5Z_{\odot}$) in a terminal wind which is captured by the proto-disk. Assuming the proto-disk has a mass the same as the bulge, this mass transformation results in an initial disk abundance of 0.005 (i.e., $0.25Z_{\odot}$) after mixing. This model makes a picture consistent with the metallicity distribution functions of both the bulge and disk (for more discussions, see Pagel 2009).

It should be mentioned that in our analysis we simply chose two values of Z_0, and then found the parameter P which gives the best fit to our distribution for each value. In a more complicated study, both P and Z_0 may be taken as fitting parameters and found when the best fit is obtained.

7.4 *Inflow Models with Declining Rates*

In more realistic models, the disk does not evolve as a closed box and a gas inflow or outflow (or both) is present. Inflow models have been attractive in many studies because of their capacity to reduce the number of low-metallicity stars born at early times, providing an elegant solution to the G dwarf problem, especially in view of the fact that the gas accretion is expected to be a common phenomenon in the Universe (e.g., Prantzos 2007). There is indirect observational evidence for gas infall into the Galactic disk. The star-formation rate in the disk is about a few solar masses per year, while the total gas mass is $\sim 5 \times 10^9$ $M_\odot$. Thus, if there were no accretion of new material, our disk would run out of gas in a fraction of the Hubble time[92] (Mo et al. 2010).

In the SCBM, all the gas of the system is available from the very beginning. A large stellar activity is then required to enrich all that gas to, say, $0.1Z_\odot$, and correspondingly many small and long-lived stars are formed at low Z. In the case of infall models, less gas is available at early ages. It takes, therefore, a small number of processes such as Supernovae or stellar winds to enrich it to $0.1Z_\odot$, and as result, fewer low mass stars are formed at low metal abundances.

Identifying the local disk with the system, the inflowing gas could originate from the gaseous halo, the bulge, the outer parts of the disk, or the accretion of small satellite galaxies. The disk itself may be considered as being formed completely from such inflowing gas or as having an initial mass (usually small compared to its final mass) with or without initial metal abundances.

Even more physically realistic models assume gas inflow with variable rates, and those with declining rates appear especially to be in better agreement with recent observations. In this section, two of the commonly-used inflow models will be addressed and the resulting metallicity distributions will be compared with that from this study.

[92] Hubble time or Hubble age provides an estimate for the age of the universe by presuming the Universe has always expanded at the same rate as it is expanding today, and its value is 13.8 billion years (taken from: http://www.astro.virginia.edu/~jh8h/glossary/hubbletime.htm).

7.4.1 *Lynden-Bell's Models*

Larson (1974, 1976) suggested dynamical models of the formation and evolution of the Galactic disk in which the disk develops outward from the central parts by a gas inflow with a rate which declines over time as gas supply runs out. The total mass of the system approaches an asymptotic limit and the mass of the gas reaches a maximum before dropping at later times more and less similar to the SCBM. Larson pointed out that these models could represent the G-dwarf metallicity distribution.

Lynden-Bell (1975) derived analytical versions of these models including his "Best Accretion Model". For this model, he postulated a non-linear relation between the gas mass and star mass of the system. This relation is the simplest quadratic formalism showing the desirable properties, i.e., the mass of the gas leads to a maximum value and then declines smoothly at later stages when star formation approaches completion. A simplified calculation of this analysis can be found in Pagel (2009) in which the gas mass is obtained by the equation:

$$g(s) = (1\text{-}s/M_f)(1+s\text{-}s/M_f) \tag{7.5}$$

where all quantities are in units of the initial mass and M_f ($\geq$1) is the final mass of the system. In the case of M_f =1, the model reduces to the SCBM. If the metallicity of the inflow gas Z_F= 0, it can be shown that

$$Z(s) = P\left(\frac{M_f}{1+s-s/M_f}\right)^2 [\ln(\frac{1}{1-s/M_f}) - (s/M_f)(1\text{-}1/M_f)] \tag{7.6}$$

and

$$\frac{ds}{d\log(Z)} = \frac{(\frac{Z}{P})[1+s(1-\frac{1}{M_f})]}{(1-\frac{s}{M_f})^{-1}-2(\frac{Z}{P})(1-\frac{1}{M_f})} \tag{7.7}$$

This produces a series of metallicity distributions with different values of M_f. We determined three distributions of this kind, as shown in Figure 7.3, for M_f = 2 (the red curve), 2.5 (the green curve), and 3 (the blue curve) with yield values P = 0.025, 0.027, and 0.028, respectively. By setting these yield values, the model distributions peak at [Fe/H] = +0.05 dex (the same metallicity as the histogram peaks). The distribution from the SCBM (the black curve), which is equivalent to the Lynden-Bell model with M_f = 1, is also demonstrated in the Figure. Although

the Lynden-Bell's models have a very good fit with our distribution, their P values are large relative to the estimated one for the local Galactic disk.

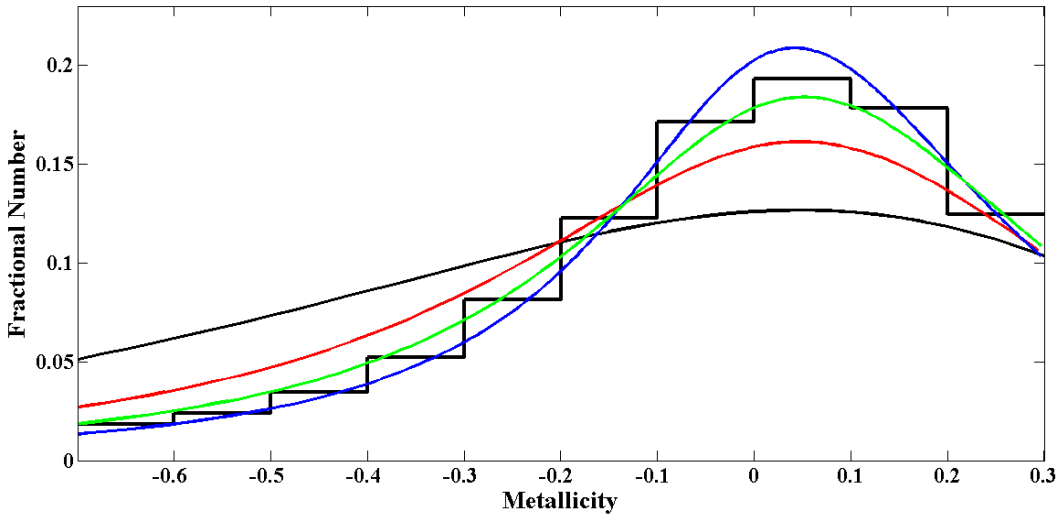

Figure (7.3) The comparison between the metallicity distribution of M dwarfs from this study (the histogram) and those from the Lynden-Bell's model with M_f = 2 (the red curve), 2.5 (the green curve), and 3 (the blue curve) as well as that from the SCBM (the black curve).

7.4.2 *The Exponential Inflow Model*

Some studies have shown that an exponentially decreasing infall rate with a long characteristic time scale ~ 7 Gyr can provide a reasonably good fit to the data. For example, Casuso & Beckman (2004) demonstrated that a model including an exponentially decreasing gas infall seems to model the observed metallicity distributions of G and K dwarfs in the Galactic disk.

To have a more straightforward analysis, some inflow models refer to a specific star formation law as (e.g., Pagel 2009)

$$\frac{ds}{dt} = w\, g\,(t) \tag{7.8}$$

in which w is a constant. By defining a time-like variable u

$$u = wt \tag{7.9}$$

Sommer-Larsen (1991) constructed a dynamical model with the assumption

$$F(u) = Aw \exp(-u) \tag{7.10}$$

where F is the accretion of material from outside the system and A is a constant. It can then be shown that (Pagel 2009)

$$g(u) = (g_0 + Au) \exp(-u) \tag{7.11}$$

where g_0 is the initial mass of the system assumed to be pure gas while the mass of the system is:

$$M(u) = g_0 + A[1 - \exp(-u)] \tag{7.12}$$

and the mass of stars is

$$s(u) = g_0(1-\exp(-u)) + A[1-(1+u)\exp(-u)]. \tag{7.13}$$

If $u \longrightarrow \infty$, the expression for Z can simply be written as

$$Z(u) = Z_F + Pu/2 \tag{7.14}$$

where Z_F is the metallicity of the inflow gas. When $g_0 = Z_F = 0$, some simple relations are obtained:

$$g(u) = Au\exp(-u) \tag{7.15}$$

$$M(u) = A[1-\exp(-u)] \tag{7.16}$$

$$Z(u) = Pu/2 \tag{7.17}$$

$$\frac{ds}{d\log(Z)} = 4A \left(\frac{Z}{P}\right)^2 \exp(-2Z/P) \tag{7.18}$$

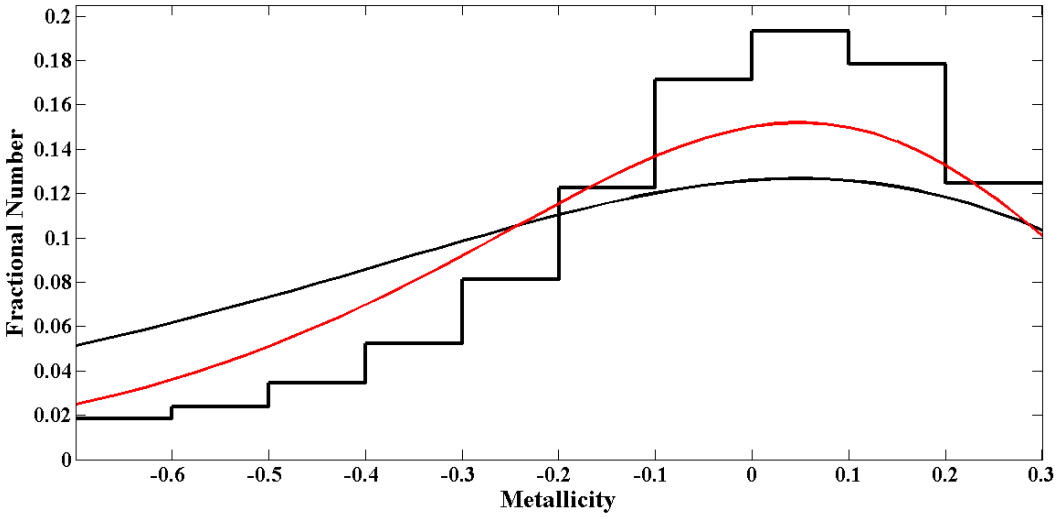

Figure (7.4) The comparison between the metallicity distribution of M dwarfs from this study (the histogram) and that form the exponential infall model (the red curve) as well as the distribution from the SCBM (the black curve).

The last relation is essentially the square of that corresponding to the SCBM. We examined this relation through our M-dwarf metallicity (Figure 7.4) for P = 0.022 (the red curve), having a maximum at [Fe/H] = +0.05 dex. To better compare, the metallicity distribution from the SCBM (the black curve) is also shown in Figure 7.4.

7.4.3 *Clayton's Models*

Clayton (1985; 1987; 1988) has proposed a series of models in which the inflow rate is parameterized by

$$F(t) = \frac{K}{t+t_0}\, g(t) \qquad (7.19)$$

where k is an integer and t_0 (or $u_0 = wt_0$) is arbitrary. By considering Equations (7.8) and (7.9), and assuming $Z_0 = Z_F = 0$, expressions for Z and ds/dlog(Z) in terms of u can be derived (Equations (8.38) and (8.39) in Pagel 2009). The red curve in Figure (7.5) shows a distribution of this kind with k = 7 and P = 0.016, having a peak at [Fe/H] = +0.5 dex. The P value in this case

is in better agreement with the approximate value of solar neighborhood. Although the model fits the low-metallicity tail of our distribution (the histogram) well compared with the SCBM (the black curve), it underestimates the number of supersolar-metallicity stars, and a modification of this model for the high-metallicity tail is needed.

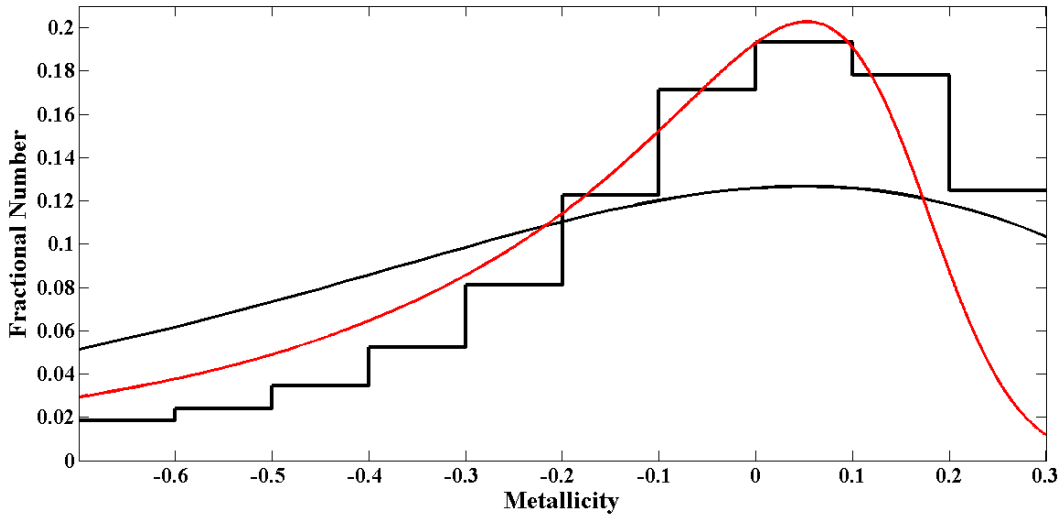

Figure (7.5) The comparison between the metallicity distributions of M dwarfs from this study (the black histogram), Clayton's model (the red curve) and the SCBM (the black curve).

Many other models, including merger models (Nagashima & Okamoto 2006), have been proposed which can mitigate, to some extent, the G and K dwarf problems. These can also be tested through M-dwarf metallicity distributions as well.

Note that it should not be expected that the values determined for the parameter P in this Chapter would be the same if the analyses were made using the observed metallicity distributions of G or K dwarfs, mainly due to the offset between the distributions of different spectral types (Section 6.5). The metallicity distribution of long-lived stars (i.e., G, K and M dwarfs) as well as the age-metallicity relation traced by the metallicity of these dwarfs (Section 6.3) are the most important observational constraints of GCE. These small stars belong to stellar populations of different ages and their metallicity distribution provides a fairly complete record of the evolutionary history of the Galaxy. However, Casuso & Beckman (2004) pointed out that G dwarfs are

sufficiently massive and they have begun to evolve away from the main sequence, and consequently, K dwarfs would make a cleaner sample for the local metal abundance distribution[93]. For the same reason, one can expect that M dwarfs (which are less massive than K dwarfs) would construct even a better sample to represents the local metallicity distribution. Moreover, M dwarfs are more numerous stars, making up around half the total stellar mass of the Galaxy. As a result, the metallicity distribution of M dwarfs offers a strong tool for studying the formation and evolution of the Milky Way. This, in turn, requires more accurate calibrations to estimate the metallicity of M dwarfs.

Summary

We examined the SCBM of GCE by comparing the distribution expected from the model with the M-dwarf distribution from this work. A significant discrepancy between the model and observations in the low metallicity tail leads to the so-called M dwarf problem, similar to the previously known G and K dwarf problems. There have been many more complicated models suggested to resolve the G and K dwarf problems which may also be possible solutions to the M dwarf problem as well. We explored a few of these models such as the SCBM with pre-enrichment and two kinds of declining infall gas models, and showed that these can, more and less, mitigate the M dwarf problem. However, more precise metallicity calibrations are needed to obtain better metallicity distributions and constrain the formation and evolution of the Galaxy more accurately.

[93] The evolutionary corrections which must be made for determining the space density and metallicity distribution of K dwarfs are smaller than those of G dwarfs (Casuso & Beckman 2004).

Conclusion

Using a sample of 71 carefully selected M dwarfs and the most recent BT-Settl model atmospheres, we developed new photometric methods to determine the metallicity and temperature of dwarfs with spectral types between K6 to M6.5 in the metallicity range -0.73 to +0.3 dex and the temperature range 2,950 to 4,250 K. The calibration sample has two parts; the first part includes 21 M dwarfs in common proper motion pairs with an FGK star or early-type M dwarf of known metallicity and the second part contains 50 dwarfs with metallicities obtained through moderate-resolution spectra. Although these methods may not be as accurate as moderate-to-high resolution spectroscopic techniques, they can be consistently applied to a large numbers of stars, facilitating statistical investigations on metallicity, temperature and distance distributions efficiently.

We selected a large sample of over 1,300,000 dwarfs from the merged SDSS and 2MASS catalogs which meet the requirements for clean photometry and fall in colour ranges necessary for our metallicity calibration as well as those ranges required for the separation of giants from dwarfs. To estimate the distance of stars, we used a photometric parallax and the colour range within which this parallax is valid was also taken into account when collecting the large sample. By applying the metallicity calibration to this large sample, we determined the metallicity distribution of late-type K and M dwarfs. Our results indicate there is a shift in metallicity distribution toward lower metallicities as the Galactic height increases. This can be attributed to the age-metallicity-Galactic height relation. Studies have shown that stars which formed at earlier times in the Galaxy's history have on average lower metallicity and are farther from the Galactic plane. We studied statistically the relation between the metallicity and absolute magnitude of our dwarfs. This shows a decrease in luminosity with increasing metallicity. There have been some studies which support this result while some others favour an increase in luminosity as a function of metallicity. More careful investigations are, therefore, needed to conclude a more accurate relation between the absolute magnitude and metallicity of M dwarfs. We also applied our temperature calibration to the large sample to obtain the temperature

distribution of these stars, showing a peak at the spectral type of ≈ M2. However, we did not find a clear relation between temperature and metallicity.

Our metallicity distribution was compared to several distributions of FGK dwarfs from previous studies. This comparison suggests an offset between distributions of different spectral types. There have been two views to explain this discrepancy. In one view, the distributions of FGK dwarfs should be the same as those of M dwarfs in the local Galactic disk and the existing offset is due to the reliability of methods for the metallicity determination in various studies. However, in another opinion, this discrepancy is attributed to different lifetimes or star formation rates of stars with different spectral types, i.e., the formation and evolution of stars depends on their spectral types.

The M-dwarf metallicity distribution from this work also indicates the existence of the M dwarf problem (similar to the previously known G and K dwarf problems), based on which the number of low metallicity M dwarfs is not sufficient to match the simple closed box model for Galactic Chemical Evolution. There have been many suggestions to resolve the G and K dwarf problems, leading to consider a number of more complicated GCE models. We tested several of these models using our volume-corrected M-dwarf metallicity distribution, as M dwarfs are the most populous stars in the Galaxy and due to their very long lifetimes, they can constitute a cleaner sample for the local metallicity distribution than G and K dwarfs. The SCBM with a pre-enrichment [Fe/H] ≅ -0.8 dex makes a better fit to our distribution and could be a promising solution to the M dwarf problem. Infall models with declining rates have also been considered as elegant solutions to the G and K dwarf problems. For this reason, we chose two commonly used models of these kinds; Lynden-Bell's model in which a non-linear, quadratic relation between the gas mass and stellar mass of the system is assumed and the exponential inflow model. It appears that both of these models produce metallicity distributions well matched to the observed M-dwarf histogram, and could resolve the local M dwarf problem. There have been many other successful models which can resolve the G and K dwarf problems and also can be tested using M-dwarf metallicity distributions in future. However, larger, better-calibrated data sets are required in order to discriminate between these models.

Future

The SDSS photometry of many M dwarfs with reliably determined metallicities is unusable because the images are saturated (especially, in the SDSS filters) and so had to be excluded from our calibration sample. A large, more homogeneous calibration sample representing a wider range of metallicities and spectral types would reduce the uncertainties associated with this technique and provide a more rigorous test of the latest synthetic model spectra. We have taken one step in this direction by obtaining data with the 1.82 m Plaskett Telescope at the Dominion Astrophysical Observatory in Victoria, British Columbia. These data will provide us with more trustworthy photometry, and in turn, with more accurate metallicity and temperature calibrations

In general, the location of an M dwarf on a colour-color diagram relates to its fundamental properties such as metallicity, temperature (spectral type), and surface gravity. However, in this study we assumed a constant log (g) for all M dwarfs and ignored its effect on metallicity and temperature. To derive more precise calibrations, we need to consider a finer grid of surface gravity and investigate the change in metallicity and temperature as a function of log (g) as well. Integration of updated model atmospheres and synthetic spectra from the BT-Settl models should also be used in future studies.

To make the volume correction to our metallicity distribution, we require a more accurate relation between metallicity and luminosity (following the work of Woolf & West 2012, but with a larger calibration sample) and then quantify the Malmquist bias. Furthermore, a careful study is needed to determine the kinematics of M dwarfs in the large sample for facilitating comparisons with other kinematically matched samples.

Finally, it is our intention to use data from other deeper surveys, including the Canada-France-Hawaii Legacy Survey (CFHTLS) and the Wide-Field Infrared Camera (WIRCam) Deep Survey (WIRDS), to extend our analyses beyond a Galactic height of ~1.5 kpc and well into the Galactic halo. For this study, we need to establish accurate equations to transform photometry from the SDSS to CFHTLS system as well as from the 2MASS to WIRDS filter set for the M dwarf regions, and then use the metallicity and temperature calibrations for CFHTLS-WIRDS samples.

References

Adelman-McCarthy, J., et al.: 2006, ApJS 162, 38

Adelman-McCarthy, J. K., et al. 2007, ApJS, 172, 634

Ahn, C. P., et al. 2012, ApJS, 203, 21

Anderson, E. & Francis, C. 2012, Extended Hipparcos Compilation, VizierR On-line Data Catalog

Allard, F. & Hauschildt, P. 1995, AJ, 445, 433

Allard, F., et al. 2001, AJ, 556, 357

Allard, F., et al. 2012, Royal Society of London Philosophical Transactions Series A, 370, 2765

Allard, F., et al. 2013, Mem. S.A.It., 24, 128

Asplund, M., et al. 2009, Annual Review of Astronomy & Astrophysics, 47, 481

Baraffe, I., et al. 1998, A&A, 337, 403

Barber, R. J., et al. 2006, MNRAS, 368, 1087

Batalha, N. M., et al. 2013, ApJS, 204, 24

Bean, J. L., et al. 2006, ApJ, 652, 1604

Bessell, M. S. 1982, Proc.ASA, 4, 417

Bessell, M. S. & Brett, J. M. 1988, PASP, 100, 1134

Bessell, M. S. 1991, AJ, 101, 662

Blake, C. H., et al. 2008, AJ, 684, 635

Bochanski, J. J., et al. 2007a, AJ, 133, 531

Bochanski, J. J., et al. 2007b, AJ, 134, 2418

Bochanski, J.J. 2008, M dwarfs in the local Milky Way: The field low-mass stellar luminosity and mass functions [Ph.D dissertation]

Bochanski, J. J., et al. 2010, AJ, 139, 2679

Bochanski, J. J., et al. 2011, AJ, 141, 98

Bochanski, J. J., et al. 2012, AJ, 143, 152

Bochanski, J. J., et al. 2013, AJ, 145, 40

Boeshaar, P. C. 1976, The Spectral Classification of M dwarf Stars (Columbus: Ohio State University Press)

Bonfils, X., et al. 2005, A&A, 442, 635
Breiman, L. 2001, Mach. Learn., 45, 5
Brook, C. B., et al. 2012, MNRAS, 426, 690
Caffau, E., et al. 2011, Sol. Phys., 268, 255
Casagrande, L., et al. 2006, MNRAS, 373, 13
Casagrande, L., et al. 2008, MNRAS, 389, 585
Casagrande, L., et al. 2011, A&A, 530, A138
Cassisi, S. 2011, eprint arXiv:1111.6464
Casuso, E. & Beckman, J. E. 2004, A&A, 419, 181
Chabrier, G. & Baraffe, I. 1997, A&A, 327, 1039
Chabrier, G. 2003, PASP, 115, 763
Chabrier, G. 2005, eprint arXiv: 0509798
Clayton, D. D., 1985, APJ, 285, 411
Clayton, D. D., 1987, APJ, 315, 451
Clayton, D. D., 1988, MNRAS, 234, 1
Covey, K. R., et al. 2007, AJ, 134, 2398
Covey, K. R., et al. 2007, AJ, 134, 2398
Covey, K. R., et al. 2008, AJ, 136, 1778
Cutri, R. M., et al. 2003, The IRSA 2MASS All-Sky Point Source Catalog, NASA/IPAC Infrared Science Archive
Dahn, C. C., et al. 1995, The Bottom of the Main Sequence and Beyond, proceedings of the ESO Workshop, edited C. G. Tinney. Springer-Verlag Berlin Heidelberg New York, p.239
Dawson, P. C. & De Robertis, M. M. 2004, AJ, 127, 2909
del Burgo, C., et al. 2011, Science and Technology of Brown Dwarfs and Exoplantes: Proceedings of an International Conference, Vol. 16, id.04006
Delfosse, X., et al. 1998, A&A, 331, 581
Deshpande, R., et al. 2013, AJ, 146, 156
Dhital, S., et al. 2012, AJ, 143, 67
Duran, S., et al. 2013, PASA, 30, e043
Freeman, K. 2011, arXiv:1108.5028v1
Freytag, B., et al. 2010, A&A, 513, id.A19

Fuhrmann, K. 2008, MNRAS, 384, 173

Fukugita, M., et al. 1996, AJ, 111, 1748

Gaidos, E., et al. 2007, Sci, 318, 210

Gilmore, G. & Reid, N. 1983, MNRAS, 202, 1025

Gizis, J. E. 1997, AJ, 113, 806

Gizis, J. E. & Reid, I. N. 1999, AJ, 117, 508

Gonzalez, G. 1997, MNRAS, 285, 403

Grenfell, J. L., et al. 2013, EGU General Assembly, 15, EGU2013-10404

Grevesse, N., et al 1993, A&A, 271, 587

Gunn, J. E., et al. 1998, AJ, 116, 3040

Hauschildt, P., et al. 1996, MNRAS, 280, 77

Hauschildt, P., et al. 1997, AJ, 490, 803

Hauschildt, P., et al. 1999, ApJ, 512, 377

Hauschildt, P. & Baron, E. 2005, Mem. S.A.It., 7, 140

Haywood, M. 2001, MNRAS, 325, 1365

Hawley, S. L., et al. 2002, AJ, 123, 3409

Homeier, D., et al. 2003, Brown Dwarfs: Proceedings of IAU Symposium, No.211, p. 419

Ivezić, Z., et al. 2004, AN 325, 583

Ivezić, Z., et al. 2007, AJ, 134, 973

Jenkins, J. S., et al. 2009, AJ, 704, 975

Johnson, J. A. & Apps, K. 2009, ApJ, 699, 933

Johnson, J. A., et al. 2012, AJ, 143, 111

Jones, J. B, et al. 1995, PASP, 107, 632

Jones, J. B, et al. 1996, MNRAS, 280, 77

Jones H. R. A, et al. 2002, MNRAS, 330, 675

Jones, D. O., et al, 2011, AJ, 142, 44

Joy, A. H. 1947, ApJ, 105, 96

Jurić, M., et al. 2008, AJ, 673, 864

Karttunen, H., et al. 2007, Fundamental Astronomy, Fifth Edition (Springer)

Keenan, P. C. & McNeil, R. C. 1976, An Atlas of Spectra of the Cooler Stars: Types G, K, M, S, and C. Part 1: Introduction and Tables (Columbus: Ohio State University Press)

Kharchenko, N. V. & Roser, S. 2009, All-Sky Compiled Catalog of 2.5 million stars, VizierR On-line Data Catalog
Kirkpatrick, J. D., Henry, T. J., & McCarthy, D. W. 1991, ApJS, 77, 417
Kirkpatrick, J. D., et al. 1999, AJ, 519, 802
Köppen, J. & Arimoto, N. 1990, A&A, 240, 22
Kordopatis, G., et al. 2013, AJ, 146, 134
Krawchuk, C. A. P., et al. 2000, AJ, 119, 1956
Kuiper, G. P. 1942, ApJ, 95, 201
Larson, R. B. 1974, MNRAS, 166, 585
Larson, R. B. 1974, MNRAS, 176, 31
Larson, K. A. & Whittet, D. C. B. 2005, AJ, 623, 897
Laughlin, G. 1997, AJ, 482, 420
Laughlin, G. 2000, AJ, 545, 1064
Lee, Y. S., et al. 2008, AJ, 136, 2022
Leggett, S. K. 1992, ApJS, 82, 351
Leggett, S. K., et al. 2002, MNRAS, 332, 78
Lépine, S., et al. 2003, ApJ, 585, L69
Lépine, S., et al. 2007, ApJ, 669, 1235
Lépine, S. & Scholz, R. 2008, ApJ, 681, L33
Lépine, S. & Gaidos, E. 2011, AJ, 142, 138
Lépine, S., et al. 2013, AJ, 145,102
Luck, R. E., & Heiter, U. 2006, AJ, 131, 3069
Lynden-Bell, D. 1975, Vistas in Astr., 19, 299
McQuillan, A., et al. 2014, ApJS, 211, 24
Mann, A. W., et al. 2013a, AJ, 145, 52
Mann, A. W., et al. 2013b, AJ, 770, 43
Mann, A. W., et al. 2014, AJ, 147, 160
Messina, S., et al. 2010, RACE-OC project: YSOs within 100pc, VizierR On-line Data Catalog
Mo, H., et al. 2010, Galaxy Formation and Evolution (Cambridge University Press)
Moorhead, A.V. 2008, The Orbital Evolution of Planet-Disk Solar System [Ph.D dissertation]
Morgan, W. W. 1938, ApJ, 87, 589

Morgan, W. W. & Keenan, P. C. 1943, An Atlas of Stellar Spectra (The University of Chicago press)

Mould, J. R. & McElroy, D. B. 1978, ApJ, 220, 935

Navarro, J. 2010, http://www.cfa.harvard.edu/events/2010/dyn/

Neves, V., et al. 2012, A&A, 538, id.A25

Neves, V., et al. 2013, A&A, 551, id.A36

Newton, E. R., et al. 2014, AJ, 147, 20

Nordström, B., et al. 2004, A&A, 418, 989

Nordström, B. 2008, The Ages of Stars, Proceedings IAU Symposium, 258

Noyes, R. W., et al. 1984, ApJ, 279, 763

Nykytyuk, T. V. & Mishenina, T. V. 2006, AA, 456, 969

Önehag, A., et al. 2011, A&A, 528, id.A85

Ostriker, J. B. & Thuan, T. X. 1975, Ap. J. Lett., 201, L51

Padmanabhan, N., et al. 2008, AJ, 674, 1217

Pagel, B. E. J. & Patchett, B. E. 1975, MNRAS, 172, 13

Pagel, B. E. J. 2009, Nucleosynthesis and Chemical Evolution of Galaxies (Cambridge University Press)

Parker, E. N. 1993, ApJ, 408, 707

Pickles, A. & Depagne, E. 2010, PASP, 122, 1437

Pinsonneault, M. H., et al. 2012, ApJS, 199, 30

Pizzolato, N., et al. 2003, A&A, 397, 147

Plez, B. 1998, A&A, 337, 495

Prantzos, N. 2007, eprint arXiv:0709.0833v1

Prantzos, N. 2007, eprint arXiv: 1101.2108v1

Quillen, A. C. & Garnett, D. R. 2000, eprint arXiv:astro-ph/0004210

Robinson, S. E., et al. 2007, ApJS, 169, 430

Rajpurohit, A. S., et al. 2010, SF2A-2010: Proceedings of the Annual meeting of the French Society of Astronomy and Astrophysics

Rajpurohit, A. S., et al. 2013, A&A, 556, id.A15

Rajpurohit, A. S., et al. 2014, A&A, 564, id.A90

Ramírez, I., et al. 2007, A&A, 465, 271

Reid, I. N. & Gizis, J. E. 1997, AJ, 114, 1992

Reid, I. N., et al. 1995, AJ, 110, 1838

Reid, I. N., & Hawley, S. L. 2000, New Light on Dark Stars Red Dwarfs, Low-Mass Stars, Brown Stars (Springer-Praxis Books in Astrophysics and Astronomy)

Robinson, S. E., et al. 2007, ApJS, 169, 430

Rojas-Ayala, B., et al. 2010, ApJL, 720, L113

Rojas-Ayala, B., et al. 2012, ApJ, 748, 93

Rojas-Ayala, B., et al. 2013, Astron. Nachr., 334, 155

Schlaufman, K. C. & Laughlin, G. 2010, A&A, 519, A105

Schlesinger, K. J., et al. 2012, AJ, 761, 160

Schmidt, M. 1963, ApJ, 137, 758

Seabroke, G. M. & Gilmore, G. 2007, MNRAS, 380, 1348

Seager, S & Mallén-Ornelas, G. 2003, AJ, 585, 1038

Sharp, C. M & Burrows, A. 2007, ApJS, 168, 140

Skrutskie, M. F., et al. 2006, AJ, 131, 1163

Sneden, C. A. 1973, http://www.as.utexas.edu/~chris/moog.html

Sommer-Larsen, J. 1991, MNRAS, 243, 468

Stelzer, B., et al. 2013, MNRAS, 431, 2063

Tashkun, S. A., et al. 2004, High-Resolution Molecular Spectroscopy: Proceedings of IAU Symposium, No.14, p.102

Taylor, B. J., & Croxall, K. 2005, MNRAS, 357, 967

Terrien, R. C., et al. 2012, ApJL, 747, L38

Thompson, M. J. & Christensen-Dalsgaard, J. 2003, Stellar Astrophysical Fluid Dynamics (Cambridge University Press)

Tucker, D. L., et al. 2006, Astron. Nachr., 327, 821

Valenti, J. A., & Piskunov, N. 1996, A&AS, 118, 595

Valenti, J. A., et al. 1998, APJ, 498, 851

Valenti, J. A. & Fischer, D. A. 2005, ApJS, 159, 141

Valentini, M., et al. 2013, 40th Liège International Astrophysical Colloquium, vol.43, id.03006

van den Bergh, S. 1962, AJ, 67, 486

Viti, S., et al. 1997, MNRAS, 291, 780

West, A. A., et al. 2004, AJ, 128, 426
West, A. A., et al. 2005, PASP, 117, 706
West, A. A., et al. 2006, AJ, 132, 2507
West, A. A., et al. 2008, AJ, 135, 785
West, A. A., et al. 2011, AJ, 141, 97
Wielen, R. 1977, A&A, 60, 263
Wing, R. F. 1973, IAU Symposium, No. 50, p. 209
Woolf, V. M. & Wallerstein, G. 2004, MNRAS, 350, 575
Woolf, V. M. & Wallerstein, G. 2005, MNRAS, 356, 963
Woolf V. M. & Wallerstein G., 2006, PASP, 118, 218
Woolf V. M., et al. 2009, PASP, 121, 117
Woolf, V. M. & West, A. A. 2012, MNRAS, 422, 1489
Wyse, R. F. G., Gilmore, G. 1995, AJ, 110, 2771
Yi, Z., et al. 2014, AJ, 147, 33
York, D. G., et al. 2000, AJ, 120, 1579
Zagury, F. 2006, MNRAS, 370, 1763
Zhao, J. K., et al. 2013, AJ, 145, 140